

9-2015

Eastern Tropical Pacific Climate And El Niño Variability During The Past Millennium

Gerald Thomas Rustic

Graduate Center, City University of New York

How does access to this work benefit you? Let us know!

Follow this and additional works at: https://academicworks.cuny.edu/gc_etds



Part of the [Geology Commons](#), and the [Paleontology Commons](#)

Recommended Citation

Rustic, Gerald Thomas, "Eastern Tropical Pacific Climate And El Niño Variability During The Past Millennium" (2015). CUNY Academic Works.

https://academicworks.cuny.edu/gc_etds/1116

This Dissertation is brought to you by CUNY Academic Works. It has been accepted for inclusion in All Dissertations, Theses, and Capstone Projects by an authorized administrator of CUNY Academic Works. For more information, please contact deposit@gc.cuny.edu.

**EASTERN TROPICAL PACIFIC CLIMATE AND EL NIÑO
VARIABILITY DURING THE PAST MILLENNIUM**

By

Gerald T. Rustic

A dissertation submitted to the Graduate Faculty in Earth and Environmental Sciences in partial fulfillment
of the requirements for the degree of Doctor of Philosophy, The City University of New York

2015

©2015

Gerald Thomas Rustic

All Rights Reserved

This manuscript has been read and accepted for the Graduate Faculty in Earth and Environmental Science in satisfaction of the dissertation requirement for the degree of Doctor of Philosophy

Prof. Athanasios Koutavas

Date

Chair of Examining Committee

Prof. Cindi Katz

Date

Executive Officer

Prof. Stephen Pekar

Prof. Marco Tedesco

Dr. Braddock Linsley

Supervisory Committee

THE CITY UNIVERSITY OF NEW YORK

Abstract

Eastern Tropical Pacific Climate And El Niño Variability During The Past Millennium

By

Gerald T. Rustic

Advisor: Professor Athanasios Koutavas

The El Niño Southern Oscillation (ENSO) has been implicated in large-scale climate shifts of the past millennia, but paleoclimate records from the dynamically vital eastern equatorial Pacific Ocean (EEP) spanning the past millennium are sparse. This has limited our understanding of tropical Pacific dynamics, leaving questions regarding the source of ENSO variability unanswered. Here I seek to address some of these questions regarding relationship between ENSO and tropical Pacific mean state, and the relationship between the tropical Pacific and large-scale climate. Mean EEP sea surface temperature (SST) for the past millennium was reconstructed using Mg/Ca ratios in *Globigerinoides ruber* from a sub-centennial resolved sediment core collected near the Galápagos Islands. ENSO activity for the past ~1000 years was reconstructed using oxygen isotope ratios ($\delta^{18}\text{O}_\text{c}$) from individual *G. ruber* foraminifera from the same sediments. For the first time, a “Mid-Millennial Shift” is identified at ~1500 CE when the tropical Pacific switched from a “La Niña-like” mean state with a strong zonal SST gradient and damped ENSO to an “El Niño-like” mean state with weak zonal gradient and amplified ENSO. The ~350-year

periods preceding and following ~1500 CE represent fundamentally different ocean-atmosphere circulation states in terms of both tropical Pacific mean state and variability. The Mid-Millennial Shift coincided with the deepest Little Ice Age cooling and a southward shift of the Intertropical Convergence Zone. This research provides context to the ENSO modulations of the past millennium by extending the SST record back to ~2700 years before present. This record reveals a long-term cooling trend of -0.22 °C/ky, similar to Northern Hemisphere temperature trends suggesting a common origin, likely insolation forcing. Warm SST, within error of modern, is observed during the peak Medieval Climate Anomaly (~900-1150 CE), contradicting the prevailing La Niña-like paradigm. Much of the past millennium is characterized by an out-of-phase EEP, which is attributed to dynamical adjustments consistent with the “dynamical ocean thermostat” mechanism. Reconstruction of the zonal SST gradient from existing western Pacific SST records supports this hypothesis. I propose that the long-term pattern of EEP SST is a response to high-latitude forcing, and propose a mechanism for the communication of this signal via the shallow overturning circulation. A combination of dynamical and thermodynamic mechanisms is invoked to explain the region’s complex SST history. The overall record suggests ENSO modulations are coupled to tropical Pacific mean state, and this paired system participates in extra-tropical climate processes.

Additional exploration of the foraminiferal record reveals a decrease of 0.3‰ in the stable carbon isotope ratios ($\delta^{13}\text{C}$) of modern individual *G. ruber* compared to pre-industrial specimens. I attribute this to the $\delta^{13}\text{C}$ -Suess effect, a result of the emission of isotopically depleted carbon into the atmosphere from fossil fuels. Based on changes in

the $\delta^{13}\text{C}$ – $\delta^{18}\text{O}_\text{c}$ relationship and differences between *G. ruber* morphotypes, I propose that upwelling in the EEP limits the penetration of the atmospheric $\delta^{13}\text{C}$ signal in this region. Investigation of Mg/Ca and $\delta^{18}\text{O}_\text{c}$ from individual specimens of the thermocline-dwelling foraminifer *Neogloboquadrina dutertrei* suggest the depth habitat of this species is consistent with the deep thermocline, but its utility as a thermocline proxy may be limited by the inability to record strong El Niño events.

Keywords:

Paleoclimate, ENSO, El Niño Southern Oscillation, paleoceanography, ocean dynamics, foraminifera, stable isotopes

Acknowledgements

I gratefully acknowledge the support of my advisor and mentor Professor Athanasios Koutavas, without whose time, effort and patience none of this would be possible. I also thank my committee and article co-authors for their insightful comments. I thank Thomas Marchitto at INSTAAR for Mg/Ca analysis and Aleksey Sadekov at Cambridge for LAICP-MS. I owe a debt of gratitude to Emilie Dassié and Wei Huang at LDEO for laboratory assistance. Thanks to the crew of the R/V Knorr, leg 195-5 under chief scientists Tim Herbert and funded by the NSF for providing the sediment samples for this research, and Mark Altabet at the University of Massachusetts, Dartmouth for funding ^{14}C analysis. I would like to acknowledge the financial support of the College of Staten Island Engineering Science and Physics Department, and the financial support of the CUNY Graduate Center. Funding from the LDEO Climate Center is gratefully acknowledged for supporting the many analyses necessary for this project.

I would like to thank my Father and my Sister for their unwavering support and confidence. I have relied on you more than you know. Thanks to Ian for the laughs, and to my nieces for asking questions. Thank you to Lisa for being tough, and to Sandrina for support through difficult days. To my friends, thank you for your patience and understanding. Thanks to Bitter and Orlando for sitting on my keyboard, and to Luna, for being a nut. And finally, thank you to Leo, whose faith in me was unwavering, whose courage has been my inspiration and who hung on until the end. Good boy.

This thesis is dedicated to my Mother, who taught me to ask questions and to look for answers.

Table of Contents

Abstract	iv
Acknowledgements	vii
List of Tables.....	x
List of Figures	xi
Introduction.....	1
Materials and Methods	5
Summary of Research Questions.....	8
Chapter 1. Dynamical Excitation of the Tropical Pacific Ocean and ENSO Variability by Little Ice Age Cooling	13
Main Text:	15
Figures	24
Chapter 2. Sea surface cooling of the eastern equatorial Pacific during the past 2700 years	30
Abstract.....	30
Introduction.....	31
Materials and Methods	33
Results and discussion	35
Conclusion	41
Tables.....	43
Figures	44
Chapter 3. $\delta^{13}\text{C}$ Suess effect observed in individual foraminifera from the eastern equatorial Pacific	49
Abstract.....	49
Introduction.....	50
Materials and Methods	53
Results.....	54

Discussion.....	64
Conclusion	69
Figures	71
Tables.....	81
Chapter 4. Paired $\delta^{18}\text{O}_c$ and Mg/Ca single-shell analysis of <i>Neogloboquadrina dutertrei</i> from the eastern equatorial Pacific: assessment of depth habitat and utility as an ENSO proxy.....	83
Abstract.....	83
Introduction.....	84
Materials and Methods	85
Results.....	87
Discussion.....	91
Conclusions.....	94
Figures	96
Conclusions.....	105
Summary.....	109
Appendix A. Supplementary Materials for Dynamical excitation of the tropical Pacific Ocean and ENSO variability by Little Ice Age cooling	111
S1. Materials and Methods	111
Tables.....	124
Figures	127
Bibliography and References.....	137

List of Tables

Table 2.1. Radiocarbon data from KNR195-5 MC42C/MC42E.....	43
Table 3.1. $\delta^{13}\text{C}$ mean and variance for each sample interval.	82
Table 3.2. <i>G. ruber</i> masses and mean $\delta^{13}\text{C}$	82
Table 4.1. <i>N. dutertrei</i> data from KNR195-5 MC38G.	104
Table SA.1. ^{14}C analyses and age control points for KNR195-5 MC42C.	124
Table SA.3. List of analyzed MC42C sample intervals and their climate data.....	126

List of Figures

Figure 1.1. Average tropical Pacific SST and 1000 mb winds (1981-2008) for March (top) and September (bottom).....	25
Figure 1.2. Climatic proxies measured on Galápagos multicore KNR195-5 MC42C.	27
Figure 1.3. Climatic evolution of the tropical Pacific in broader context.	29
Figure 2.1. Map of the tropical Pacific showing average sea surface temperatures.....	44
Figure 2.2 Sea surface temperature records of the past several millennia.....	45
Figure 2.3. Comparison of climate reconstructions and SST records.	48
Figure 3.1. Map of the study location. Top panels show March temperature (left) and phosphate concentrations (right).....	71
Figure 3.2. $\delta^{13}\text{C}$ records from the past millennium.	73
Figure 3.3. <i>G. ruber</i> $\delta^{13}\text{C} - \delta^{18}\text{O}_\text{c}$ relationship.	74
Figure 3.4. $\delta^{13}\text{C} - \delta^{18}\text{O}_\text{c}$ R – values for each sampled interval.....	76
Figure 3.5. <i>G. ruber</i> morphotype differences in $\delta^{13}\text{C}$ mean and variance.....	77
Figure 3.6. <i>G. ruber</i> morphotype $\delta^{13}\text{C} - \delta^{18}\text{O}_\text{c}$ relationships.	79
Figure 3.7. <i>G. ruber</i> $\delta^{13}\text{C}$ mass effect in the analyzed MC42C samples.....	80
Figure 4.1. Frequency histogram of individual <i>N. dutertrei</i> $\delta^{18}\text{O}_\text{c}$ from two size fractions.	96
Figure 4.2. Depth habitat for <i>G. ruber</i> and <i>N. dutertrei</i>	97
Figure 4.3. $\delta^{13}\text{C}-\delta^{18}\text{O}_\text{c}$ for <i>N. dutertrei</i> for 355 μm and 425 μm size fractions. No statistically significant relationship is observed between $\delta^{13}\text{C}$ and $\delta^{18}\text{O}_\text{c}$ in <i>N. dutertrei</i> from MC38G.	98
Figure 4.4. Relationship of $\delta^{13}\text{C}$ and $\delta^{18}\text{O}_\text{c}$ to mass in <i>N. dutertrei</i> of two size fractions.	99
Figure 4.5. Mg/Ca and $\delta^{18}\text{O}_\text{c}$ from same-shell analysis.....	100
Figure SA.1. MC42C age model with 1-sigma age uncertainty.....	127
Figure SA.2. Time series of monthly sea surface temperature (SST), salinity (SSS), and computed $\delta^{18}\text{O}_\text{c}$ from SODA reanalysis data, for the $0.5^\circ\times0.5^\circ$ grid box surrounding the study site (Carton and Giese 2008).	128
Figure SA.3. $\delta^{18}\text{O}_\text{c}$ data of individual <i>G. ruber</i> from KNR195-5 MC42C.....	131

Figure SA.4. Comparison of $\delta^{18}\text{O}_c$ values measured on <i>G. ruber</i> single shells from surface sediments (1951-2009, purple), and computed from SODA 2.1.6 reanalysis data (1958-2009, gray).....	132
Figure SA.5. Reconstructed versus instrumental $\delta^{18}\text{O}_c$ variance for 1860-2009.	133
Figure SA.6. Records of ENSO variance during the past millennium.	134
Figure SA.7. <i>G. ruber</i> mean $\delta^{13}\text{C}_c$ from MC42C.	135
Figure SA.8. Comparison of mean $\delta^{18}\text{O}_c$ from MC42C and an Urvina Bay coral (Dunbar et al. 1994).	136

Introduction

In recent decades the tropics have emerged as a major focus of paleoclimate research (Cane 1998, Chiang 2009). The highly dynamic nature of the tropical oceans and the close coupling of the atmosphere and tropical surface ocean allows tropical climate variability to be projected into the mid-and high-latitudes (Chiang 2009). The tropics' ability to influence climate on a global scale is exemplified by the El Niño Southern Oscillation (ENSO), which affects temperature and precipitation regimes across a wide swath of the world (Rasmusson and Carpenter 1982). Our understanding of ENSO dynamics has greatly improved in the past decades, but much remains unknown. Our ability to accurately predict the strength of individual ENSO events remains limited (Barnston et al. 2012), and the situation is made more difficult by the non-stationarity of the climate and the uncertainty of the climate system's response to anthropogenic change (Collins et al. 2010, Stevenson et al. 2012, Cai et al. 2014, Cai et al. 2015).

ENSO is the expression of strong coupled atmosphere-ocean interactions in the tropical Pacific Ocean, and dominates interannual climate variability around the globe. The mean state of the eastern equatorial Pacific features strong, seasonally variable wind-driven upwelling, a shallow thermocline and cool sea surface temperatures (SST) (Deser and Wallace 1990). Mean western tropical Pacific conditions feature warmer SSTs and deep atmospheric convection. This east-west zonal SST gradient sets up a zonal pressure gradient that drives the tropical trade winds from east to west, forming the surface flow of the Walker circulation (Bjerknes 1969). Bjerknes (1969) described a feedback process in

Introduction

which eastern Pacific upwelling is driven by these tropical trade winds, resulting in cool EEP SST and strengthening of the SST gradient, intensifying the Walker circulation and enhancing upwelling and cooling of the EEP (Bjerknes 1969, Wang and Fiedler 2006). Perturbations to this feedback cycle through positive EEP SST anomalies in the eastern Pacific (Wang et al. 2012) cause a cascade of feedbacks through the ocean-atmosphere system and a weakening of the Walker circulation. Reduced trade winds diminish the strength of EEP upwelling and result in SST warming in the EEP, a reduction of the zonal SST and pressure gradients and further diminishing of the trade winds. El Niño conditions are the end result of this process and feature warm SST anomalies in the EEP, cool SST anomalies in the western Pacific, a reduced zonal SST gradient, and a deeper EEP thermocline (McPhaden et al. 2006). In the EEP, SST anomalies can exceed 3 °C in the eastern Pacific cold tongue during strong events (Carton and Giese 2008). ENSO events reach their peak intensities at the end of calendar year, and are currently phase-locked with the seasonal cycle (Rasmusson and Carpenter, 1982). The location of deep tropical convection shifts from the western Pacific toward the warmer SSTs in central Pacific, altering precipitation patterns throughout the tropics and extra-tropics (Rasmusson and Carpenter, 1982). Anomalous westerly wind bursts in the western Pacific that slow the equatorial trade winds have been linked to the initiation of El Niño events (Fedorov et al. 2014). It has been proposed that the termination of these events is the result of negative feedbacks in the tropical ocean-atmosphere system, including the shoaling of the thermocline and cooling of surface of the western Pacific (Wang et al. 2012) and the reflection of thermocline-propagating Rossby and Kelvin waves off the

Introduction

eastern and western boundaries of the Pacific basin inducing upwelling and cooling in the EEP that terminates the El Niño event (McPhaden et al. 2006, Wang and Fiedler 2006). La Niña conditions occur when the Bjerknes feedback continues to strengthen the Walker circulation and intensifies the cooling of the EEP beyond normal conditions, resulting in cool SST anomalies in the EEP and warm SST anomalies and enhanced deep convection in the western Pacific. The overall spatial pattern of ENSO varies with each event (Fedorov et al. 2014), and differences in the degree and location of greatest SST anomalies have given rise to the proposal of different “flavors” of ENSO, including eastern Pacific El Niño (described above) and central Pacific “El Niño Modoki” that feature maximal SST anomalies in the central rather than Eastern Pacific (Ashok et al. 2007).

The impact of ENSO on interannual climate is wide-ranging and spans far beyond the tropical Pacific (Rasmusson and Carpenter 1982, McPhaden et al. 2006, Chiang 2009). ENSO reconstruction from tree rings (D’Arrigo et al. 2006) and using multi-proxy techniques (Mann et al. 2009) suggest that ENSO has varied on longer, centennial-to-millennial timescales, and model studies have suggested that these centennial variations may be related to tropical mean state (Karnauskas et al. 2012). The high level of natural variability in the climate system and relatively short duration of the instrumental record necessitates long-term paleoclimate archives to provide adequate perspective. ENSO reconstructions spanning the past millennium have been plagued by a lack of direct and continuous records of conditions in the dynamically important eastern equatorial Pacific,

Introduction

and instead have relied on discontinuous coral records (Cobb et al. 2003, Cobb et al. 2013) from the central Pacific, distantly teleconnected tree ring records (Cook et al. 2004, Fowler et al. 2008), and lake sediment records (Conroy et al. 2008, Moy et al. 2002) that rely on indirect and poorly calibrated hydrological relationships. Such indirect and remote records provide an incomplete picture of the conditions of the tropical Pacific, limiting our ability to reconstruct past tropical conditions and infer relationships between the tropics and extra-tropical influences. Last Glacial Maximum reconstructions support a connection between tropical mean state, ENSO, and high-latitude insolation forcing (Koutavas and Joanides 2012; Sadekov et al. 2013), but it has been suggested that ENSO modulation during the past millennium has been driven by internal variability and not linked to larger-scale climate or insolation forcing (Cobb et al. 2013).

At this juncture, ENSO science appears to be confronted by an overarching fundamental question: Are the modes of ENSO variability ultimately driven by natural climate processes, or are they forced by external factors? The answer to this question requires robust insights from paleoclimate data that can resolve the mean state and variability of the tropical Pacific Ocean. A key region for investigation is the eastern equatorial Pacific (EEP), which is the central stage for the dynamical unfolding of ENSO events, and also a major determinant of the mean basin-wide state. Model studies of the tropical Pacific have posited that the EEP acts as a “Dynamical Ocean Thermostat” (Clement et al. 1996), cooling in response to positive forcing of the tropics and warming under negative forcing conditions. The EEP’s role as this “Dynamical Ocean Thermostat” (Clement et al. 1996),

Introduction

and its possible role in climate shifts of the past millennium, including the warm Medieval Climate Anomaly (MCA, ~900-1250 CE) and cooler Little Ice Age (1450-1850 CE) make this region an important target for identifying connections between extra-tropical climate processes and tropical dynamics (Mann et al. 2009, PAGES2K 2013). Hypotheses implicating EEP dynamics in these climatic changes (Mann et al. 2005, Mann et al. 2009) raise additional research questions including: What is the nature of the connections between extra-tropical forcing and tropical dynamics? What is the mechanism for the communication of climate signals from high latitudes to the tropics? And is it possible to detect and attribute changes in ENSO variability (Cobb et al. 2013)?

Materials and Methods

The brevity of the instrumental record and long-term nature of these questions necessitates the use of paleoclimate archives in the search for answers. Here, I make use of the geochemical properties of planktonic, mixed-layer dwelling foraminifer *Globigerinoides ruber* to reconstruct sea surface temperature (SST) and SST variability related to ENSO. Sediments containing *G. ruber* were obtained from multi-core KNR195-5 MC42C, collected by the R/V Knorr on 4/4/2009 from 615 m near the Galápagos Islands in the EEP cold tongue region. The sediment core was sampled contiguously at sub-centimeter intervals corresponding to a temporal resolution from ~20 to 90 years.

The temperature relationship of oxygen-18 to oxygen-16 ratios ($\delta^{18}\text{O}_c$) in biogenic calcite has long been recognized (Urey 1947, Epstein 1953). Emiliani (1955) created a

Introduction

reconstruction of Pleistocene temperatures from foraminiferal $\delta^{18}\text{O}_c$ in 1955, demonstrating the utility of this powerful tool. Calibrations relating $\delta^{18}\text{O}_c$ to temperature and the $\delta^{18}\text{O}$ ratio of seawater ($\delta^{18}\text{O}_{\text{sw}}$) for various foraminifera species and for low-light and high-light conditions have since been formulated (Bemis et al. 1998), and the effect of salinity on $\delta^{18}\text{O}_c$ has been quantified through salinity- $\delta^{18}\text{O}_{\text{sw}}$ relationships (e.g. Fairbanks et al. 1982).

In the calcium carbonate tests of foraminifera, it has been empirically observed that magnesium replaces calcium as a function of temperature (Nürnberg et al 1996, Rosenthal et al. 1997), resulting in calibrations relating Mg/Ca ratios and temperature (Rosenthal et al. 1997, Dekens et al. 2002, Anand et al. 2003) and accounting for salinity (Hönisch et al. 2013). Paleothermometry using Mg/Ca has been extensively used to reconstruct SST in the western Pacific (Newton et al. 2006, 2011, Oppo et al. 2009, Linsley et al. 2010) and through the early and mid-Holocene in the EEP (Lea et al. 2004, Koutavas et al. 2006).

The ratio of stable carbon isotopes ($\delta^{13}\text{C}$) in biogenic calcite also contains environmental information, although it is a more enigmatic proxy related to nutrients (King and Howard 2004), upwelling (Beveridge and Shackleton, 1994), remineralized carbon (Gruber et al. 1999), the global carbon cycle (Böhm et al. 2002), and anthropogenic input to the atmosphere (Keeling 1979). The atmospheric decline in $\delta^{13}\text{C}$ compared to pre-industrial times (Francey et al. 1999) attributed to $\delta^{13}\text{C}$ -depleted fossil fuel emissions (Andres et al.

Introduction

2012) is known as the $\delta^{13}\text{C}$ -Suess effect (Suess 1955, Keeling 1979). This $\delta^{13}\text{C}$ -Suess effect has been observed in corals and sponges (see Swart, 2010, for an overview) and in foraminiferal $\delta^{13}\text{C}$ (Beveridge and Shackleton, 1994, Al-Rousan et al. 2004, Black et al. 2011) across ocean basins.

In this thesis, the foraminifer *Globigerinoides ruber* (white) is the primary species used to reconstruct past ocean conditions. *G. ruber* is a mixed layer dwelling species used extensively in SST reconstructions (e.g. Newton et al. 2006, Oppo et al. 2009, Linsley et al. 2010, Koutavas et al. 2003, Koutavas et al. 2006, Koutavas and Joanides 2012) and in stable carbon isotope analysis (Beveridge and Shackleton 1994, Al-Rousan et al. 2004, Black et al. 2011). *G. ruber* has two morphotypes, *sensu stricto* and *sensu latu* (Wang 2000, Löwemark et al. 2005) thought to occupy slightly different temperature and depth habitats. The thermocline-dwelling species *Neogloboquadrina dutertrei* is also analyzed (Chapter 4). *N. dutertrei* from the Western Pacific has been used to infer subsurface conditions (Rosenthal et al. 2013) and individuals of this species have been used to reconstruct thermocline variability in the EEP (Leduc et al. 2009). Paired analysis of $\delta^{18}\text{O}_\text{c}$ and Mg/Ca ratios in *N. dutertrei* individuals has also been used to infer its depth habitat (Steinhardt et al. 2015).

Single-shell analysis

Analysis of $\delta^{18}\text{O}$, $\delta^{13}\text{C}$ and Mg/Ca ratios in foraminifera commonly uses aggregate samples consisting of sufficient shells to obtain a representative mean value. A relatively novel approach to analysis for $\delta^{18}\text{O}_\text{c}$, $\delta^{13}\text{C}$ and Mg/Ca is the analysis of single

Introduction

foraminiferal shells. The oceanic conditions experienced during the brief 2-4 week life span of the foraminifera (Spero 1998) is reflected in the shell chemistry, and thus analysis of multiple individuals from a sediment horizon is analogous to obtaining brief “snapshots” of oceanic conditions. While the method does not allow for the ordering of this data, it generates a population distribution from which population-level statistics can be calculated and compared across sediment intervals to identify changes in underlying oceanic conditions (Koutavas et al. 2006).

Tests of this method have relied on comparison of core-top sediments with modern oceanographic data (Koutavas et al. 2006, Khider et. al 2011). Here, I have the significant added advantage of core-top samples that are modern and therefore directly comparable with instrumental data to test the basic assumptions of this method. Critiques of this technique suggest that changes in the seasonal cycle and changes in ENSO variability are quantitatively indistinguishable in the EEP (Thirumali et al. 2013, Ford et al. 2015). In this thesis new methods of data analysis are used to extract information about high-probability ENSO events and the frequency of those events, supporting the use of this technique as an ENSO proxy.

Summary of Research Questions

Using these materials and techniques, specific research questions can be addressed about the nature of ENSO variability. These research questions include:

- 1) Is the detection and attribution of ENSO signals with single specimen analysis possible?

Introduction

$\delta^{18}\text{O}_c$ from single shells of *G. ruber* foraminifera in modern-era sediments is compared with instrumental and reanalysis data of the past ~150 years (SODA 2.1.6) to demonstrate the ability of single shell $\delta^{18}\text{O}_c$ to capture the modern SST variance due to ENSO. Using this technique to reconstruct ENSO and Mg/Ca to reconstruct mean SST, I identify distinct modes of ENSO variability during the past millennium and attribute changes in ENSO to dynamical shifts in the tropical Pacific, modulated by movement of the Intertropical Convergence Zone (ITCZ) prompting a reorganization of tropical Pacific dynamics.

- 2) What is the relationship between the mean state of the tropical Pacific and ENSO variability?

Our reconstruction of ENSO variability and SST over the past millennium, combined with existing records of SST from the Western Pacific (Oppo et al. 2009) allows the reconstruction of the zonal temperature gradient of the tropical Pacific in order to test for a relationship between the mean state and ENSO. I find that ENSO activity over the past millennium is related to the mean state of the tropical Pacific, with La Niña-like mean state conditions inhibiting ENSO activity, while El Niño-like mean state conditions are associated with more active ENSO.

- 3) What is the nature of the connections between extra-tropical climate and tropical Pacific dynamics, and what is the mechanism for the communication of climate signals from high latitudes to the tropics?

Introduction

The dynamical states identified in the EEP over the past millennium are seen to alternate in concert with Northern Hemisphere climate shifts from the MCA to the LIA, when Northern Hemisphere temperatures were generally warmer and cooler (respectively). Migration of the ITCZ in response to these changes in the Northern Hemisphere (Schneider et al. 2014) provides a plausible mechanism linking large-scale climate with modes of tropical dynamics.

To determine the connection between the tropics and high-latitudes over longer time scales, I use Mg/Ca paleothermometry to reconstruct EEP SST for the past 2700 years. The similarity of the long-term cooling trends found in the EEP and in Northern Hemisphere multi-proxy reconstructions (Moberg et al. 2005, Mann et al. 2009, Ljundqvist et al. 2010), tree ring records (Esper et al. 2012), ice records (Alley 2000), and SST and subsurface temperatures from the Western Pacific (Oppo et al. 2009, Newton et al. 2006, 2011, Rosenthal et al. 2013) suggests common forcing, likely high-latitude insolation changes. Evidence from the western Pacific (Rosenthal et al. 2013) is used to generate a hypothesis describing the mechanism for the transmission of high-latitude climate signals via intermediate waters formed in the South Pacific, which enter the EEP via the shallow overturning circulation of the Pacific Ocean (Gu and Philander 1997), allowing the high-latitude cooling signal to be communicated (Rosenthal et al. 2013).

- 4) Do the records from the EEP show signs of anthropogenic carbon entry into the ocean?

Introduction

Stable carbon-13 isotope ratios ($\delta^{13}\text{C}$) from the individual *G. ruber* shells analyzed reveal a decline in mean $\delta^{13}\text{C}$ from the pre-industrial era to the modern, consistent with a $\delta^{13}\text{C}$ Suess effect resulting from the burning of fossil fuels (Suess 1955, Keeling 1979). Factors in the mean $\delta^{13}\text{C}$ decrease are explored in the context of the foraminiferal proxy and the oceanographic setting in the EEP. It is proposed that upwelling limits the penetration of the atmospheric $\delta^{13}\text{C}$ signal in the EEP (Beveridge and Shackleton, 1994).

- 5) Are thermocline-dwelling *N. dutertrei* foraminifera from the EEP capable of capturing ENSO variability in thermocline temperatures?

Paired analysis of Mg/Ca and $\delta^{18}\text{O}_\text{c}$ in individual *N. dutertrei* shells from core-top sediments provide insights into this species' depth habitat and ability to capture the full range of thermocline conditions experienced in the modern era. A notable lack of correlation between $\delta^{18}\text{O}_\text{c}$ and Mg/Ca data is observed, and the possibility that this reflects varying habitats during ontogeny (Steinhardt et al. 2015) is explored.

These questions are addressed in detail in the research presented in the following chapters. The purpose of this research is two-fold – first, to provide the first long-term, continuous reconstructions of SST and ENSO variance in the EEP, a dynamically important region yet one whose history over recent millennia is largely unknown. Second, this research aims to address an over-arching question about ENSO variability, namely, are large-scale modulations in ENSO the product of internal variability, or are

Introduction

they related to external climate processes? By reconstructing ENSO and the tropical Pacific mean state, and relating these to large-scale climate records, it may be possible to identify and characterize linkages between the tropical Pacific and global climate. These findings can make significant contributions to our understanding of climate during the past several millennia. It is with these goals in mind that this research is presented here.

Chapter 1. Dynamical Excitation of the Tropical Pacific Ocean and ENSO Variability by Little Ice Age Cooling

Submitted for publication 11 July, 2015

Gerald T. Rustic,^{1,2,*}, Athanasios Koutavas,^{1,2,3}, Thomas M. Marchitto,⁴, and Braddock K. Linsley³

¹ Department of Engineering Science and Physics, College of Staten Island, City University of New York, Staten Island, NY, 10314, USA

² Doctoral Program in Earth and Environmental Sciences, Graduate Center of the City University of New York, New York, NY, 10016, USA

³ Lamont–Doherty Earth Observatory of Columbia University, 61 Route 9W, Palisades, NY 10964, USA

⁴ Department of Geological Sciences and Institute of Arctic and Alpine Research, University of Colorado, Boulder, CO 80309, USA.

* Corresponding author: grustic@gradcenter.cuny.edu

Abstract:

Tropical Pacific Ocean dynamics have been implicated in the origin and evolution of the Medieval Climate Anomaly (MCA, ~900-1450 CE) and Little Ice Age (LIA, ~1450-1850 CE). However, evidence from the dynamically crucial eastern equatorial Pacific has remained elusive. We reconstructed sea surface temperature, El Niño-Southern Oscillation (ENSO) activity, and the tropical Pacific zonal gradient from Galápagos

ocean sediments. We find that the ~350-year periods preceding and following ~1500 CE represent fundamentally different ocean-atmosphere circulation states in terms of both mean state and variability. During a newly identified ~1500 CE “Mid-Millennium Shift” (MMS), the tropical Pacific switched from a state with strong zonal gradient and dampened ENSO to one with weak zonal gradient and amplified ENSO. The MMS coincided with deepest LIA cooling and was likely caused by southward shift of the Intertropical Convergence Zone. Peak MCA (900-1150 CE) was a warm period in the eastern Pacific (comparable to modern), contradicting the paradigm of an extended La-Niña pattern.

Main Text:

The tropical Pacific Ocean exerts a major influence on global climate through the inter-annual El Niño–Southern Oscillation (ENSO) (McPhaden et al. 2006), and Pacific Decadal Oscillation (PDO) (Mantua and Hare, 2002). However, its role on centennial to millennial timescales remains an open question. Recent evidence that a cool eastern equatorial Pacific (EEP) played a key role in the global warming slowdown or “hiatus” of the past ~15 years (Kosaka and Xie, 2013, England et al. 2014) places new urgency on this question and emphasizes the need to understand tropical Pacific climate in the recent past. During the last millennium, Northern Hemisphere (NH) climate evolved from a warm Medieval Climate Anomaly (MCA, ~900-1450 CE) into a substantially colder Little Ice Age (LIA, ~1450-1850 CE), followed by modern warming (Moberg et al. 2005, Mann et al. 2009, Ljundqvist 2010). In the tropics, the MCA to LIA transition was manifested as a weakening of the East Asian Summer Monsoon (Zhang et al. 2008, Tierney et al. 2010), a southward shift of the Atlantic and Pacific Intertropical Convergence Zones (ITCZ) (Haug et al. 2001, Sachs et al. 2009), and sea surface cooling in the Western Pacific Warm Pool (WPWP) (Newton et al. 2006, Oppo et al. 2009). Notably absent, however, are records of sea surface temperature (SST) spanning the MCA-LIA transition from the ENSO sensitive and dynamically important cold tongue of the EEP. Without such records any dynamical connections between basin-scale tropical Pacific processes and NH climate cannot be properly diagnosed.

Despite limited evidence, it has been hypothesized that a “dynamical ocean thermostat” (Clement et al. 1996) response of the EEP to solar and volcanic forcing induced a cool “La Niña-like” mean state during the MCA, and a warmer “El Niño-like” state during the LIA (Mann et al. 2009). This hypothesis has found some support in central Pacific corals (Cobb et al. 2003), North American tree rings documenting medieval mega-droughts (Cook et al. 2004) and in multi-proxy climate field reconstructions (Mann et al. 2009). In each of these cases however, direct confirmation from the EEP has been lacking. Insights into past ENSO variability have also remained elusive, and are mostly based on discontinuous corals (Cobb et al. 2013) and remote tree ring records (Li et al. 2011, Emile-Geay et al. 2013). Here we address these data limitations with new climate reconstructions from the heart of the EEP cold tongue. We present continuous, multi-decadally resolved estimates of local SST, basin-wide zonal SST gradient, and ENSO activity from ~1000 to 2009 CE from Galápagos marine sediments.

Our primary datasets were developed from an ocean multicore (KNR195-5 MC42C) retrieved in 2009 near Española Island in the Galápagos ($01^{\circ} 15.58'S$, $89^{\circ} 41.13'W$ 615m). Undisturbed recovery of the sediment-water interface and detection of bomb radiocarbon confirm that the core-top is modern (See Appendix A). Sedimentation rates average 13.0 cm/ky but vary from 7.9 to 27.3 cm/ky with the largest changes coinciding with climatic signals. Unambiguous detection of a modern 0.3‰ carbon isotope ($\delta^{13}\text{C}$) depletion, or Suess effect, further corroborates the presence of a modern core top, core integrity and argues against significant signal attenuation by bioturbation (See Appendix

A). The core was slabbed continuously in sub-centimeter slices representing ~20-80 year time periods. We analyzed Mg/Ca of the mixed-layer foraminifera *Globigerinoides ruber* (white) as a proxy for mean SST, and $\delta^{18}\text{O}_c$ (calcite) of individual *G. ruber* shells (~60 individual *G. ruber* analyses per sample horizon) to quantify population-level $\delta^{18}\text{O}_c$ variance related to ENSO activity (Koutavas et al. 2006, Koutavas and Joanides 2012). Benchmark tests comparing modern samples with instrumental data support the use of single-shell $\delta^{18}\text{O}_c$ variance ($\delta^{18}\text{O}_c V$) as a proxy of the monthly SST variance (SSTV) of the real ocean, and further show that large ENSO events are consistently captured by isotopic outliers (See Appendix A).

Our Mg/Ca record reveals systematic changes in eastern Pacific SST of ~1°C (Figure 1.2C and Figure 1.3D) superimposed on a preindustrial (900-1850 CE) cooling trend of -0.37°C/ky, which, although not statistically significant ($p=0.23$), parallels trends in the NH (Figure 1.3C) and the WPWP (Figure 1.3E). Our data reveal warm SST during the peak of the MCA (900-1150 CE) coeval with NH warmth. The timing of this warm period is firmly constrained by a calibrated ^{14}C age at 1137 CE (± 72 years 1-sigma) (Figure 1.3C). This finding contrasts with a previously hypothesized dynamical La Niña state for the MCA (Mann et al. 2009). To further test this hypothesis, we computed the zonal SST gradient using reconstructed WPWP SST (Figure 1.3E) and our Galápagos record. During 900-1150 CE the zonal gradient was similar to the 20th century, not supporting a La Niña-like mean state. Instead, during this period the tropical Pacific was uniformly warm in the east and west, in phase with NH warmth.

Following peak MCA warmth Galápagos SST cooled by ~ 1 °C between ~ 1150 and ~ 1500 CE. This cooling occurred in parallel with NH cooling but had a larger amplitude and was more rapid in the EEP. An anomalous strong zonal SST gradient became established during this period (Figure 1.3F), largely due to more rapid cooling in the east than the west. This enhanced zonal gradient is evidence of dynamical changes in Pacific circulation and supports the notion of a cool La Niña-like mean state. However the timing of this change in tropical Pacific mean state (1150-1500 CE) post-dated peak NH MCA warmth and was instead associated with transitional NH cooling into the LIA. The origin of this dynamical anomaly remains unclear. Volcanic and solar forcing (Figure 1.3A and B) indicate an increase in volcanism in the 12th century followed by a decrease in solar activity in the 13th century, but overall correlations between these forcings and SST are poor. The observed EEP cooling and enhanced zonal gradient in light of decreasing external forcing are not consistent with a dynamical ocean thermostat mechanism (Mann et al. 2009, Clement et al. 1996).

At ~ 1500 CE, the EEP cooling trend ended and local SSTs began to increase and become more volatile signaling a shift in the dynamical character of the EEP (Figure 1.3D). Beginning in the 16th century, an anomalous weak zonal gradient was established as the WPWP continued to cool but the EEP trend reversed from cooling to warming (Figure 1.3D-F). This reversal occurred as the NH descended into the coldest portion of the LIA in the 16th and 17th centuries (Figure 1.3C), and lasted into the mid-19th century.

Throughout most of the LIA the zonal gradient remained reduced, evoking an extended El Niño-like mean state (Mann et al. 2009). This state appears to have ended with renewed WPWP warming in the early 20th century.

The record of $\delta^{18}\text{O}_c$ from single-shell *G. ruber* allows us to test for ENSO modulation in association with the above mean state shifts. Figure 2A shows $\delta^{18}\text{O}_c$ measurements of individual shells ($N=1325$) from 24 samples spanning the entire past millennium. By virtue of the short foraminiferal life cycle (month or less) single-shell $\delta^{18}\text{O}_c$ responds to seasonal and interannual signals, the latter of which dominates the tails of the $\delta^{18}\text{O}_c$ distribution through the presence or absence of outliers. Explicit identification of ENSO events in these data is only possible for very strong negative (El Niño) and positive (La Niña) outliers. For example, our data recovered strong negative outliers suggestive of the historic El Niños of 1997-98, 1982-83 and 1876-77 (Figure 1.2A), although one-to-one correspondence of any of our data with specific events is beyond the method's capability (See Appendix A). For more modest anomalies, however, we can only assign probabilities that they represent ENSO events. To illustrate, using historical ENSO events and monthly reanalysis data we calculate that $\delta^{18}\text{O}_c$ values exceeding a $\pm 1\%$ departure from the mean have an >87% probability of occurring during El Niño and 100% probability of occurring during La Niña (Figure 1.2A) (See Appendix A). The frequency of these “high-probability ENSO outliers” shows clear modulation through time. For example the period 1500-1850 CE had threefold more frequent warm and cold outliers than the period 1150-1500 CE (adjusted for sample size). Such high-probability ENSO

outliers are the largest driver of the integrated $\delta^{18}\text{O}_c\text{V}$ signal (Figure 1.2B), justifying its interpretation as an ENSO index.

The pattern of $\delta^{18}\text{O}_c\text{V}$ during the millennium (Figure 1.2B) shows striking similarity with Mg/Ca SST ($R=-0.43$, $p<0.05$, Figure 1.2C) considering these data sets are entirely independent and based on different geochemical proxies and separate foraminifera samples. A conspicuous feature of both is a mid-millennium (~1500 CE) change in the proxy character. When $\delta^{18}\text{O}_c\text{V}$ is compared with the reconstructed SST gradient (Figure 1.3F and 1.3G) a significant inverse correlation is evident ($R=-0.48$, $p<0.05$). This result implies a fundamental association between a weaker zonal gradient and strong ENSO variability, and vice-versa. The LIA (1500-1850 CE) stands out as a period with high $\delta^{18}\text{O}_c\text{V}$ and by inference greater ENSO activity with a distinct peak in the 18th century. The LIA also shows unusual general volatility with large century-scale swings in mean EEP SST (Figure 1.3D) and $\delta^{18}\text{O}_c\text{V}$ (Figure 1.3G). In contrast, the preceding period 1150-1500 CE had the lowest ENSO activity of the millennium and was less volatile. Compared to the LIA, this state had 20% less $\delta^{18}\text{O}_c$ variance (F-test $p<0.05$, Brown-Forsythe test $p<0.05$) and 1.0-1.5°C stronger zonal gradient. Because the ENSO variance in our data is superimposed on a large annual cycle, this 20% change in $\delta^{18}\text{O}_c\text{V}$ potentially indicates a much greater change in ENSO. To further quantify this, we modeled the effect of ENSO on $\delta^{18}\text{O}_c\text{V}$. By holding the seasonal cycle constant to its modern value and varying the amplitude of ENSO anomalies in the instrumental era, we calculated that a 20% decrease in total variance required a ~55% decrease in ENSO

amplitude. We conclude from these comparisons that the ~350-year periods preceding and following ~1500 CE represent fundamentally different dynamical states. The basin-wide tropical Pacific appears to have toggled between these states during a “Mid-Millennium Shift” (MMS) that unfolded over the 16th century.

The MMS occurred as the NH descended into the coldest portions of the LIA leading us to consider a NH trigger. The rapidity of the MMS suggests an atmospheric transmission mechanism. The tropical atmosphere is dominated by the seasonally migrating ITCZ. Evidence linking the ITCZ to hemispheric warming and cooling cycles is widespread throughout the last glacial period (Schneider et al. 2014) and implicates southward ITCZ displacements during NH cold periods, consistent with theory and models (Schneider et al. 2014, Chiang and Bitz, 2005). We propose that the same mechanism operated during the MMS as LIA cooling intensified. A southward shift of the ITCZ during the MCA-LIA transition has been proposed for the Atlantic (Haug et al. 2001), Western Pacific (Newton et al. 2006), Central Pacific (Sachs et al. 2009), and the Peruvian Andes (Thompson et al. 2013). Evidence for increasing precipitation offshore Panama after 1700 CE likely signals the northward return of the ITCZ (Linsley et al. 1994) from its more southerly LIA position. A southward ITCZ shift about ~1500 CE naturally integrates these observations with our findings of EEP warming and reduced zonal gradient across the Pacific. This is fundamentally the same type of ocean-atmosphere adjustment that accompanies individual El Niño events as the ITCZ shifts south over anomalous equatorial surface ocean warming. Under a more southerly ITCZ, cross-

equatorial southeast trade wind stress in the EEP diminishes leading to weaker cold-tongue development (Figure 1.1A) and reduced zonal gradient. Our results suggest the onset of similar conditions during the MMS was accompanied by dynamical excitation of ENSO activity, a finding that is corroborated by coral ENSO evidence from the 17th century (Cobb et al. 2003). The relationship between the zonal SST gradient and ENSO variability is central to the understanding and modeling of basin-scale tropical Pacific dynamics. Some models support an intrinsic relationship between a weak zonal gradient and high ENSO variance (Karnauskas et al. 2012) in accordance with our results.

However, a general divergence of ENSO and tropical Pacific climate responses in 21st century model simulations (Collins et al. 2010) highlights the need for insight and constraints from past reconstructions.

Our reconstruction extends into the 21st century and offers a unique millennial perspective on modern conditions. Modern SSTs are the highest of the millennium yet within error of peak MCA values, and therefore not unprecedented. Modern $\delta^{18}\text{O}_{\text{cV}}$ values are intermediate between the millennium maxima and minima, and therefore do not support unusual ENSO activity. What is unusual however is a hint of greater El Niño amplitudes in the late 20th century. In particular, the event tentatively matched to the 1997-98 El Niño has no precedent in the earlier part of the millennium (Figure 1.2A). A warming trend in the EEP appears to have followed the end of the LIA (~1850 CE) although it is coarsely resolved in our sediment record and must be viewed cautiously. Such warming is not evident in gridded instrumental data for our site, which however are

subject to considerable ambiguity (Vecchi et al. 2008, Deser et al. 2010). The warming trend now places the EEP on a parallel trajectory with NH climate since 1850 CE, contrasting with its out-of-phase relationship during the LIA. In so doing it re-establishes an in-phase relationship that existed during peak MCA warmth. The factors that induced dynamical changes in the Pacific's zonal gradient between 1150 and 1850 CE were seemingly not at play during peak MCA and may have again become disengaged in modern times. The in-phase relationship between the EEP and NH during the warmest times of the millennium (peak MCA and present) requires an explanation, and may simply mean that the ITCZ is too far removed from the equator to exert dynamical influence, allowing broader scale thermodynamics to become dominant.

Figures

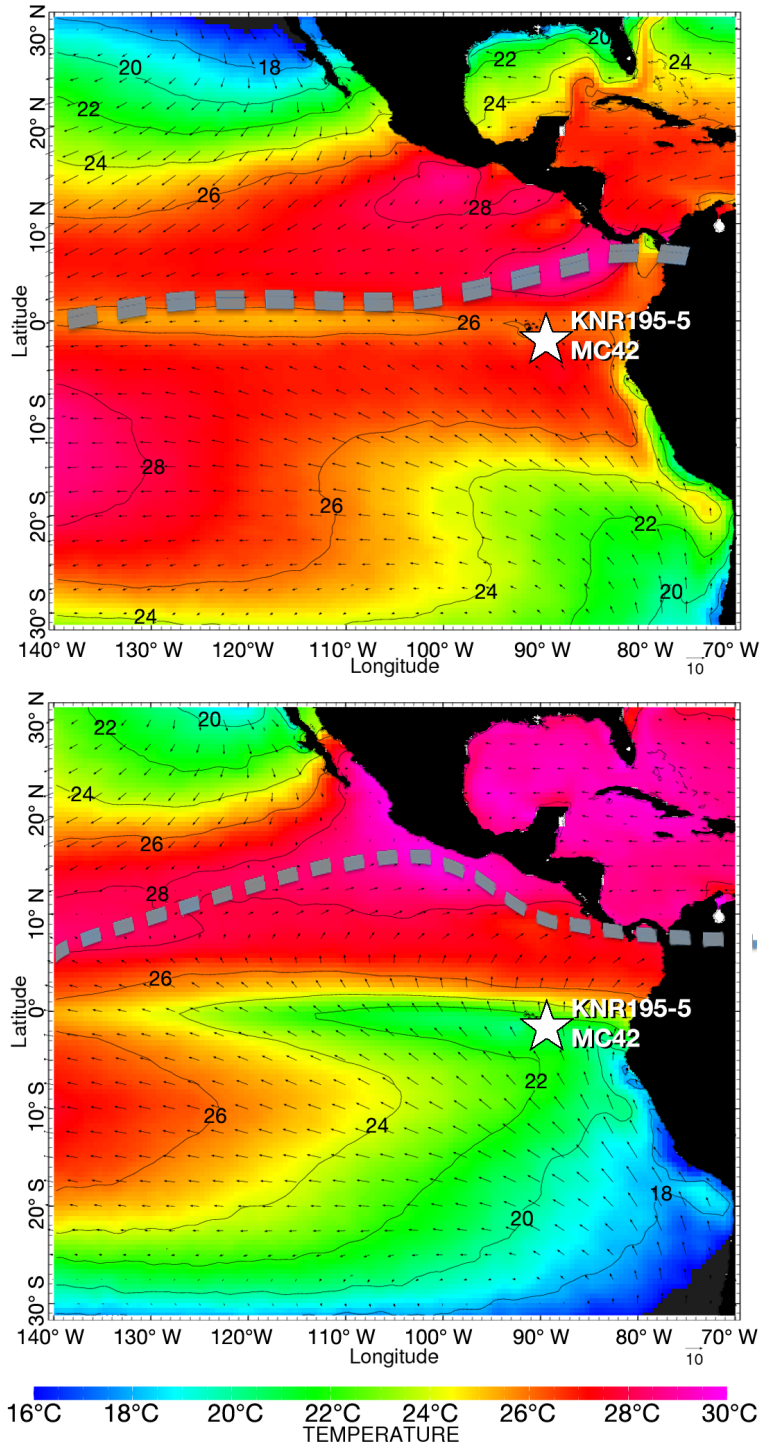


Figure 1.1. Average tropical Pacific SST and 1000 mb winds (1981-2008) for March (top) and September (bottom). KNR195-5 MC42 core location is denoted by white star. Mean SST is from SODA 2.1.6 1981-2008 (Carton and Geise 2008); 1000 mb wind are from NOAA NCEP-NCAR CDAS 1981-2009 (Kalnay et al. 1996). The position of the ITCZ is indicated by the gray dashed lines where wind vectors converge.

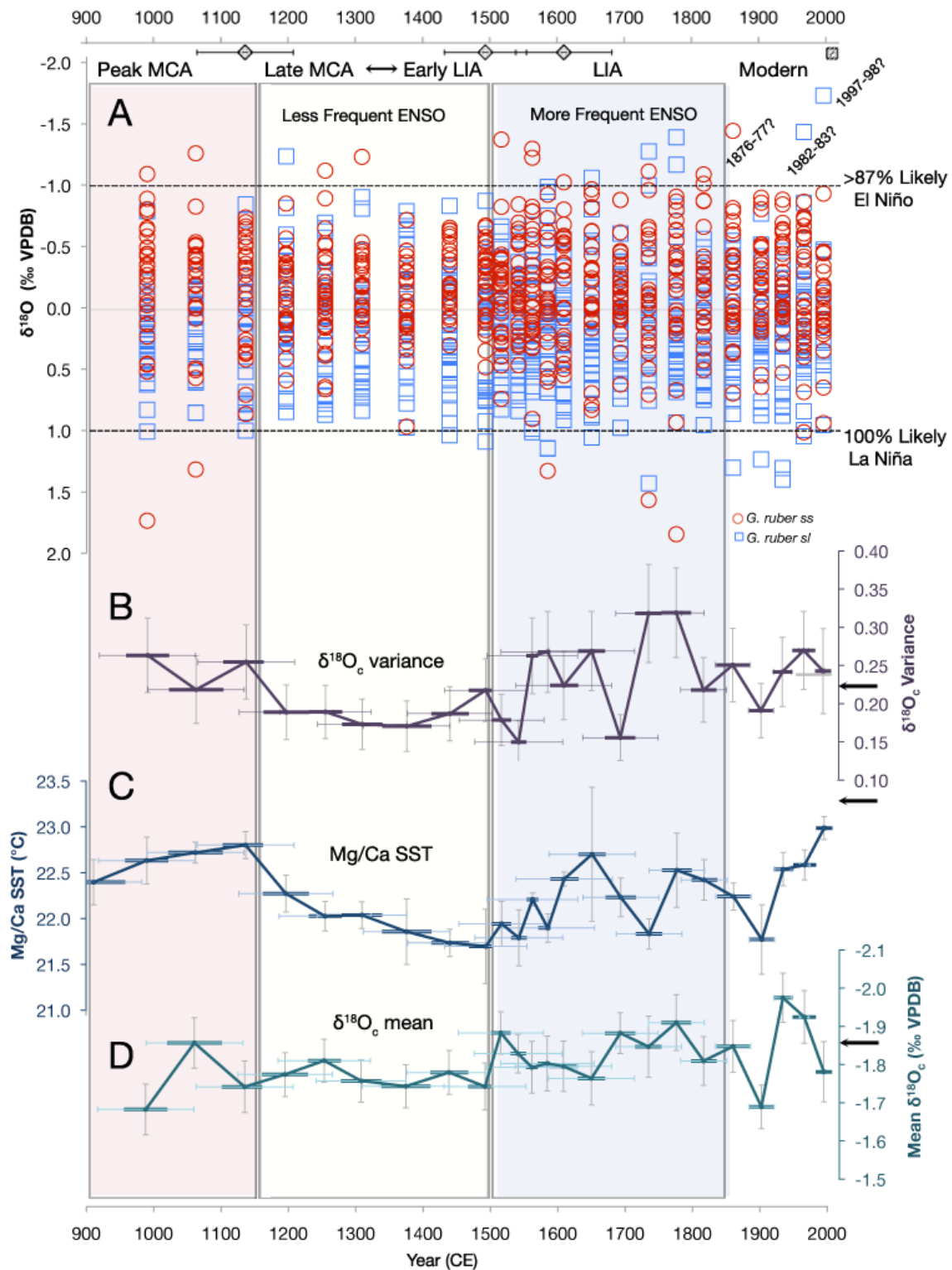


Figure 1.2. Climatic proxies measured on Galápagos multicore KNR195-5 MC42C. (A) Individual *G. ruber* $\delta^{18}\text{O}_c$ in 24 contiguous samples after removing the sample means, shown in (D). Red circles denote *sensu stricto* (*ss*) and blue squares *sensu lato* (*sl*) morphotypes, which together capture the correct mean, variance, and skewness of historical SST data (See Appendix A) . Radiocarbon age control points are shown by black diamonds (top). Whiskers are 1-sigma age uncertainty. The multi-core-top is assumed to be modern (2009). Horizontal dashed lines denote $\delta^{18}\text{O}_c$ values $\pm 1.0\text{\textperthousand}$ from the mean, denoting high-probability El Niño and La Niña events outside this range. $\delta^{18}\text{O}_c$ values consistent with historical extreme El Niño events in 1876-77, 1982-83, and 1997-98 are indicated. (B) *G. ruber* $\delta^{18}\text{O}_c$ variance ($\delta^{18}\text{O}_c\text{V}$) for each of the 24 sample intervals. Vertical error bars show the standard error of the variance; (C) *G. ruber* Mg/Ca SST. Each datum is the average of triplicate analyses. Standard deviation of the replicates is shown as vertical error bars. (D) Mean *G. ruber* $\delta^{18}\text{O}_c$. Vertical bars show the standard error of the mean. For (B), (C) and D the horizontal bars denote the duration of each sample interval and horizontal whiskers show the 1-sigma age error for each interval. Modern values computed from SODA 2.1.6 denoted by arrows on the right hand side.

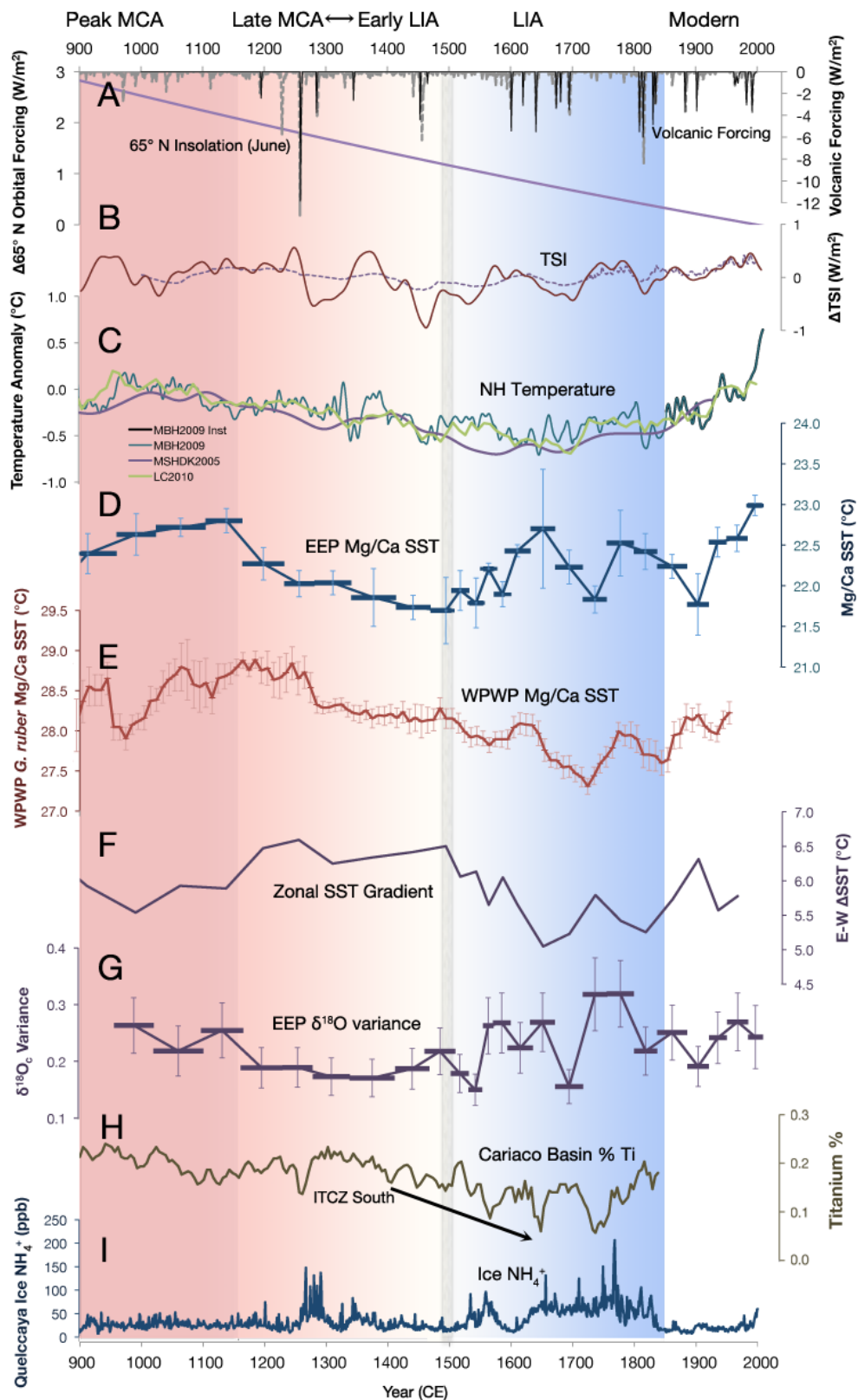


Figure 1.3. Climatic evolution of the tropical Pacific in broader context. (A) Volcanic forcing (dotted gray lines from Crowley et al. (2013); black solid line from Mann et al. (2009)), and 65°N June orbital forcing (Laskar et al. 2004) as anomaly from present. (B) Total Solar Irradiance (TSI) anomaly; (Steinhilber et al. 2009) solid red line and (Mann et al. 2009) dotted purple line. (C) NH temperature reconstructions (MSHDK2005 (Moberg et al. 2005), purple; LC2010 (Ljundqvist 2010), green; MBH2009 (Mann et al. 2009), blue); Instrumental record (MBH2009 Inst (Mann et al. 2009)) in black. (D) EEP Mg/Ca SST from KNR195-5 MC42C. Bar widths represent interval duration. Vertical whiskers show analytical uncertainty. (E) WPWP *G. ruber* Mg/Ca SST from four Makassar Straight cores (Oppo et al. 2009). Vertical whiskers show analytical error. (F) Zonal SST gradient (difference between (E) and (D)) after interpolation of the EEP data to the higher resolution of the WPWP data. (G) EEP $\delta^{18}\text{O}_\text{c}$ variance from individual *G. ruber* as in Fig 2B. Bar width shows interval duration. Vertical whiskers show the standard error of the variance. (H) Titanium % in the Cariaco Basin showing the southerly migration of the ITCZ around 1500 CE (Haug et al. 2001). (I) NH_4^+ (ppb) from the Quelccaya ice core (Thompson et al. 2013) interpreted as southward movement of the ITCZ.

Chapter 2. Sea surface cooling of the eastern equatorial Pacific during the past 2700 years

Abstract

Sea surface temperatures (SST) of the eastern equatorial Pacific (EEP) exert a major influence on global climate variability, as exemplified by the interannual climate variations of the El Niño Southern Oscillation (ENSO). However, the SST history of this region over recent millennia is poorly constrained due to lack of *in situ* records with sufficient resolution. Here, we present the first continuous SST reconstruction with sub-centennial resolution spanning the past ~2700 years and extending to modern times (2009 CE), from Mg/Ca ratios of planktonic foraminifera from the Galápagos Islands. This record exhibits a statistically significant long-term cooling trend of -0.22 °C/ky, similar to Northern Hemisphere multi-proxy temperature reconstructions, suggesting a common origin. Superimposed on this trend are multi-century scale features which, within dating uncertainty, match recognized climate periods of the Northern Hemisphere such as the Roman Warm Period (RWP, ~0-400 CE), Dark Ages Cold Period (DACP, ~450-850 CE), and early (peak) Medieval Climate Anomaly (MCA, 900-1150 CE). This in-phase climate relationship between the EEP and Northern Hemisphere through peak MCA suggests these were extensive, possibly global, climatic events. Following peak MCA and through most of the past millennium including the Little Ice Age (~1500-1850 CE), the EEP and Northern Hemisphere exhibit an out of phase relationship which is attributed to

Chapter 2: Sea surface cooling of the EEP during the past 2700 years

dynamical adjustments of the tropical Pacific Ocean circulation, in response to atmospheric forcing (Chapter 1). The last millennium has been the most dynamic period of the past 2700 years in the EEP, with significant ($\sim 1^{\circ}\text{C}$) SST variability and evidence for modulation of the basin-wide tropical Pacific zonal gradient. Modern warming in our Galápagos reconstruction, although rapid, is within error of temperatures of the RWP and MCA. As a whole these observations suggest that the EEP climate has been evolving in complex and significant ways over the past 2700 years, while maintaining discernible associations with broader, hemispheric, and possibly global processes. We emphasize here the long-term cooling trend of the past 2700 years and draw attention to orbital forcing as the likely source of this signal.

Introduction

The tropical Pacific Ocean features a large ($\sim 5.5^{\circ}\text{C}$) SST gradient between the western Pacific warm pool (WPWP) and the EEP cold tongue. Instrumental observations demonstrate that perturbations of this zonal gradient in association with El Niño Southern Oscillation (ENSO) events precipitate globally extensive climate anomalies, and affect upper ocean heat storage and global mean surface temperatures (Tourre and White, 1995). Since the zonal SST gradient is in large part maintained by cool upwelling in the EEP (Deser and Wallace 1990), the coupled ocean-atmosphere dynamics and SST structure of this region are crucial for the basin-wide circulation. There is currently little understanding about how SST has evolved in the EEP over recent millennia or over the entire Holocene (Koutavas et al. 2002; 2006; Koutavas and Joanides, 2012).

Mg/Ca ratios in planktonic foraminifera have been used to characterize SST in the tropical Western Pacific Ocean during recent millennia (Newton et al. 2006, Oppo et al. 2009, Linsley et al. 2010, Newton et al. 2011, Rosenthal et al. 2013). Similar records from the EEP, however, have been unavailable. Climate reconstructions from this region have relied instead on indirect proxy evidence. Such evidence includes discontinuous coral $\delta^{18}\text{O}$ records from the central Pacific (Cobb et al. 2003), distantly teleconnected tree-ring evidence from North America (Cook et al. 2004) and Australasia (Fowler et al. 2008), and climate field reconstructions from large spatial networks of diverse proxy data (Mann et al. 2009). Freshwater diatoms found in Galápagos lake sediments have been used to infer SST during the last millennium (Conroy et al. 2009) but these are reliant on indirect hydrographic relationships. Further, $\delta^{18}\text{O}$ of Andean ice cores has been correlated to conditions in the NINO3.4 region adjacent to the EEP, although the source waters for this glacial ice is believed to be the Atlantic basin (Thompson et al. 2013). Our ability to accurately reconstruct EEP climate over the past two and a half millennia, and to assess changes in the strength of the tropical Pacific's zonal SST gradient, thus remains limited by the lack of direct EEP records.

Here we present a ~2700-year record of SST derived from Mg/Ca ratios in *Globigerinoides ruber* (white) foraminifera from the Galápagos Islands. This record provides us with the unique opportunity to (i) identify long-term EEP SST trends, (ii) determine the scale of centennial variability in the EEP and (iii) compute changes in the

Chapter 2: Sea surface cooling of the EEP during the past 2700 years

zonal SST gradient through comparison with western Pacific SST records. Our reconstruction spans recognized climate shifts of the past two and a half millennia, including the Roman Warm Period (RWP, ~0-400 CE), Dark Ages Cold Period (DACP, ~450-850 CE) (Lamb 1995), Medieval Climate Anomaly (MCA, 900-1350 CE), Little Ice Age (1450-1850 CE), and the modern era (1850-2009 CE).

Materials and Methods

Study Location

Deep-sea sediment multi-core (KNR195-5 MC42C) was collected near the Galápagos Islands ($01^{\circ} 15.58' S$, $89^{\circ} 41.13' W$, 615m depth) in the heart of the EEP cold tongue (**Figure 2.1**). Local monthly mean SST from the *Simple Ocean Data Assimilation* reanalysis product (SODA 2.1.6, Carton and Giese 2008) ranges from $21.3^{\circ} C$ in September to $26.3^{\circ} C$ in March. Vigorous upwelling, driven by strong cross-equatorial winds, produces the cool tropical SSTs characteristic of the cold tongue (Deser and Wallace, 1990). These winds vary seasonally, with the weaker winds driving less vigorous upwelling as the Intertropical Convergence Zone (ITCZ) approaches the equator and strong wind-driven upwelling when the ITCZ approaches $10^{\circ} N$ during boreal summer. Oceanic conditions in the EEP are strongly affected by ENSO with monthly SST anomalies exceeding $\pm 3^{\circ} C$ during the strongest El Niño or La Niña events (SODA 2.1.6).

Chapter 2: Sea surface cooling of the EEP during the past 2700 years

Materials and Age Model

Sediment multi-core KNR195-5 MC42C was sampled continuously at sub-centimeter intervals with an average sample thickness of 0.58 cm, representing ~20-95 years of deposition per interval. Eight radiocarbon ages (**Table 2.1**) on *Neogloboquadrina dutertrei* from MC42C and companion core MC42E were obtained from National Ocean Sciences Accelerator Mass Spectrometer (NOSAMS) in Woods Hole, MA. Results were calibrated using Calib 6.1 (Stuiver and Braziunas 1993) using a delta-R of 125 ± 66 years based on published Galápagos reservoir ages (Druffel, 1981; Druffel et al. 2004; Taylor et al. 1967). Based on (i) undisturbed recovery of the sediment water interface, (ii) an anomalously young age at 2-3cm depth in MC42E, indicative of bomb-era radiocarbon, and (iii) the presence of a discernible $\delta^{13}\text{C}$ -Suess effect at the core top of MC42C (see Chapter 3), we assigned to the core-top an age corresponding to the year of collection (2009). A radiocarbon age reversal occurs below 28 cm suggesting sediments below this depth may be disturbed. We therefore limited our investigations to the top 28 cm representing ~2700 years of deposition. The age model was constructed based on linear interpolation between six age control points, one corresponding to the modern (2009) core top and the rest corresponding to five calibrated radiocarbon ages in stratigraphic order (**Table 2.1**).

Mg/Ca Analysis

Sea surface temperatures (SST) were reconstructed from Mg/Ca ratios of *G. ruber*, a mixed layer dwelling foraminifer based on well-established and widely used calibrations (Dekens et al. 2002, Anand et al. 2003). ~100 specimens of *G. ruber* from the 250-300

Chapter 2: Sea surface cooling of the EEP during the past 2700 years

µm size fraction were selected in roughly equal proportions of *sensu stricto* and *sensu latu* morphotypes (Wang, 2000) for analysis. Samples were gently crushed to expose inner chamber walls, homogenized, and split into triplicate subsamples. They were then subjected to reductive and oxidative cleaning after removal of clay-size contaminants (Boyle & Keigwin, 1985, Boyle & Rosenthal, 1996). Mg/Ca ratios were analyzed on a Thermo Finnigan Element 2 ICP-MS at INSTAAR, University of Colorado (Marchitto, 2006). Long-term analytical precision, based on repeat measurements of liquid standards, is $\pm 0.5\%$, or ~ 0.015 mmol/mol for these samples. True sample reproducibility, expressed as the average standard deviation of 48 sets of triplicate analyses, is ± 0.61 mmol/mol, or ± 0.24 °C. Mg/Ca ratios (mmol/mol) were converted to temperature (T, °C) using the relationship

$$\text{Mg/Ca} = 0.38 \exp(0.09*T) \text{ (Eq. 1.) (Anand et al. 2003)}$$

Modern (1985-2008) annual mean SST for the core site from SODA 2.1.6 reanalysis data (Carton and Giese, 2008) is 23.44 °C. Mg/Ca SST from the core-top sediment interval is 22.99 ± 0.13 °C, within the ± 1.2 °C standard error of the calibration (Anand et al. 2003). Diagenetic effects on Mg/Ca due to dissolution are considered to be minimal based on the shallow depth of the core and good preservation quality of the analyzed foraminifera.

Results and discussion

Our Mg/Ca results are shown in **Figure 2.2 B**, and provide a longer perspective on the millennium-length SST record discussed in Chapter 1. The two most striking features of this longer record are a long-term cooling trend of -0.22 °C/ky ($p<0.05$) over the past 2700 years, and increased variability in reconstructed SST in the second half of the

Chapter 2: Sea surface cooling of the EEP during the past 2700 years

record compared to the first. This increase in SST variability is illustrated in **Figure 2.2 D**, showing the increase in the residuals from the long-term trend. The detection of the 2700-year cooling trend in EEP SST is a new finding, as no other direct EEP SST records span this time period. Superimposed on this trend are significant multi-century scale SST oscillations. More specifically, we observe warm SST between 700 BCE and ~300 CE (through the RWP), followed by cooler temperatures that prevailed from ~400-900 CE during the DACP. Renewed warming occurs from 900-1150 CE, a period recognized as the peak of the MCA, and is followed by cooling of over 1°C from 1150-1500 CE in the transition between the MCA and LIA. Beginning at 1500 CE, we observe the highly variable warming throughout the LIA that is discussed in Chapter 1. The record ends in the modern era with the warmest observed SST, although this is within error of SST at 600 BCE, the RWP, and peak MCA warmth.

The trend at our Galápagos site is similar to trends seen in the Western Pacific (**Figure 2.2 B**) suggesting the entire tropical Pacific participated in a cooling trend, whose origins remain unknown. For example, cooling over the last 2000 years is observed by both Newton et al. (2006, 2011) and Oppo et al. (2009), who also find relatively warm temperatures in modern sediments. Cooling is observed over the Holocene in Western Pacific Mg/Ca SST records from Linsley et al. (2010) and Stott et al. (2004). Cooling of the thermocline and deeper waters (500-900 m) of the Western Pacific since the early Holocene temperature maximum has been reported by Rosenthal et al. (2013) (**Figure 2.3 G**). In the eastern Pacific, Lea et al. (2006) observed cooling over much of the Holocene,

Chapter 2: Sea surface cooling of the EEP during the past 2700 years

but this record is coarsely resolved and does not include the last two millennia. These records and the cooling trend that we observe in our EEP data may be part of a larger tropical ocean cooling trend spanning the entire Holocene.

Following the approach taken in Chapter 1, our data from the EEP allow for the first time a quantitative estimation of the east-west SST gradient of the tropical Pacific, considered diagnostic of basin-wide dynamics. To do this, we compare our data with a Mg/Ca SST record of the Western Pacific (Oppo et al. 2009) spanning the last 2000 years (**Figure 2.2 A**). To compute the zonal gradient we averaged the more highly resolved western Pacific SST data to match the resolution of each interval in our EEP reconstruction. In the first millennium of this record, small scale fluctuations of the strength of the gradient are observed, though most are on the order of ± 0.5 °C with durations of about a century. Given that the uncertainty of the zonal gradient estimation is approximately twice the analytical uncertainty of the individual records, or about 0.4-0.5 °C, such small changes in the gradient may be considered noise and not meaningful to interpret. The most significant periods of centennial-scale modulation of the zonal gradient occur during the last millennium, with a prolonged strengthening of the gradient between 1150-1500 CE, followed by a sharp weakening ~1500 CE, and persistence of a weakened gradient between ~1600-1850 CE. These swings in the zonal gradient were discussed in Chapter 1, in the context of corresponding changes in ENSO dynamics reconstructed from single-shell $\delta^{18}\text{O}$. The longer perspective of the past 2,000 years shown here emphasizes that the

Chapter 2: Sea surface cooling of the EEP during the past 2700 years

last millennium appears unusual in displaying a considerably larger range of variability in EEP SST and zonal gradient relative to the previous millennium.

We explore our dataset in the larger context by comparing it with temperature reconstructions of the Northern Hemisphere (NH) and global mean. Figure 2.3 shows temperature reconstructed from the GISP2 ice core (Alley et al. 2000) (**Figure 2.3 B**), multi-proxy NH and global temperature reconstructions (Moberg et al. 2005, Mann et al. 2009, Llundqvist 2010, Marcott et al. 2013) (**Figure 2.3 C**) and tree-ring based (maximum latewood density, MXD) Fennoscandia summer temperature reconstruction (Esper et al. 2012) (**Figure 2.3 D**). All of these records indicate cooling trends over recent millennia. In addition, these records show evidence of multi-century scale oscillations that are broadly recognized as the RWP, DACP, MCA and LIA, although their timing in the various records is not always contemporaneous but is generally within the 1-sigma age uncertainties. Our record arguably also shows evidence of similar climatic oscillations in phase with their NH counterparts up until 1150 CE, but evolving differently thereafter. Warm SST at our site from 200 BCE to ~200 CE corresponds to the RWP observed in Greenland ice and Fennoscandian tree ring reconstructions (Figure 3). This warming is followed by cooler SST between ~450-850 CE corresponding with the DACP, and is succeeded by early MCA warming between 900-1150 CE. These climatic features are in phase between our Galápagos SST reconstruction and the NH. However, this relationship appears to change after 1150 CE and to give way to pattern that can be described as out-of-phase with the NH mean. This pattern was discussed

Chapter 2: Sea surface cooling of the EEP during the past 2700 years

extensively in Chapter 1, and was linked to dynamical adjustment of the basin-wide ocean-atmosphere circulation in response to deep NH cooling in the transition from MCA to LIA. The out-of phase relationship is most clearly seen during the “Mid-Millennium Shift” of ~1500 CE, identified in Chapter 1, when Galápagos SST warmed in the face of pronounced NH cooling. A southward shift of the Intertropical Convergence Zone (ITCZ), was likely responsible for inducing the EEP warming during the LIA, and was further linked to excitation of ENSO activity.

Observation of similar cooling trends in Northern Hemisphere temperature records and in the Western Pacific suggests that this cooling is hemispheric or possibly global in scale. A new reconstruction of global mean surface ocean temperature over the past two millennia indeed supports the global extent of such cooling (McGregor et al. 2015). While this specific study attributed the cooling to volcanism, earlier studies have invoked Milankovitch orbital forcing as the cause of NH cooling (Ljundqvist 2010, Esper et al. 2012, Marcott et al. 2013). **Figure 2.3 (A)** shows the 65°N summer insolation curve indicating a 9 W/m² decrease over the past 2700 years, which is part of the longer Holocene decline from a maximum ~10,000 years ago. It is generally held that 65°N summer insolation has been the critical factor for the inception and termination of the Pleistocene ice ages, but the mechanism through which this forcing acts to cool the globe remains poorly understood. If the cooling observed in the eastern and western tropical Pacific over the past 2-3 millennia is a response to NH high-latitude insolation forcing, the question as to how this signal is communicated to the tropics must be addressed.

Chapter 2: Sea surface cooling of the EEP during the past 2700 years

Cooling similar to the EEP has been observed in the deep thermocline (600-900 m) of the western Pacific (Rosenthal et al. 2013). These waters are sourced from North Pacific Intermediate Water (NPIW) and Antarctic Intermediate Water (AAIW) that form at mid- and high-latitudes of the North and South Pacific, respectively. Rosenthal et al. (2013) suggest the surface cooling of the western Pacific is a result of the upward mixing of these cooler intermediate waters sourced from extra-tropical and subantarctic latitudes. The mechanism for the observed cooling of the EEP may be analogous with the western Pacific. The source waters of EEP upwelling are the AAIW and Subantarctic Mode Waters (SAMW), which form part of the shallow overturning circulation of the Pacific (Gu and Philander 1997, Johnson and McPhaden 1999, Rogers et al. 2003). These waters are entrained in the Equatorial Undercurrent (EUC) that upwells in the EEP (Johnson and McPhaden 1999, Kessler et al. 2006), and influences the properties of the surface waters (Gu and Philander, 1997). Our hypothesis is that the long-term cooling trend of the EEP is a reflection of the cooling of intermediate water masses forming at subtropical and sub-Antarctic latitudes in the Southern Hemisphere, similar to the proposed mechanism driving cooling in the western Pacific (Rosenthal et al., 2013). It remains unclear whether (and if so how) these southern-sourced water masses experience cooling in response to 65°N insolation. One possibility is that NH summer insolation cools North Atlantic Deep Water (NADW) that upwells in the Southern Ocean and forms the precursor to these intermediate water masses. Another possibility is that the southern water masses cool not

Chapter 2: Sea surface cooling of the EEP during the past 2700 years

in response to 65°N forcing, but in response to Southern Hemisphere insolation forcing at a season (austral spring) which shares the same phase with 65°N.

SST reconstructions from the Southern Ocean and South Pacific support long-term cooling over the Holocene. Shevenell et al. (2011) report Holocene-length cooling from TEX-86 records from the West Antarctic Peninsula at 65°S. Holocene cooling is also seen in $\delta^{18}\text{O}_\text{c}$ benthic foraminifera records from the Chatham Rise in the western Pacific (at 45°S) (Pahnke et al. 2003). And an alkenone SST reconstruction from the Peru Margin (41°S) shows cooling over the entire Holocene, including the past 3000 years (Kaiser et al. 2005). These records provide evidence for cooling of the extra-tropical Pacific source regions for intermediate waters feeding the tropical thermocline and upwelling in the EEP (Johnson and McPhaden 1999, Kessler et al. 2006). This cooling of the high-latitude source waters would allow for the communication of high-latitude climate signals to the tropics via the shallow meridional overturning circulation of the South Pacific (Gu and Philander, 1997). We propose this as the main mechanism behind the EEP cooling trend revealed in our data over the past 2700 years.

Conclusion

We have produced the first available reconstruction of EEP SST from Galápagos marine sediments with sub-century resolution spanning the past 2700 years. The record documents a $-0.22^\circ\text{C}/\text{ky}$ cooling trend similar to trends seen in western Pacific SST and thermocline temperature, and in NH mean temperature reconstructions. Superimposed on the EEP cooling trend are multi-centennial scale signals broadly associated with the

Chapter 2: Sea surface cooling of the EEP during the past 2700 years

RWP, DACP, MCA, and LIA. Of these, the RWP, DACP and peak MCA are in phase between the EEP and NH, while the LIA is distinctly out of phase, signaling a shift in the equatorial ocean-atmosphere dynamics, arguably related to extratropical LIA cooling. The presence of such signals suggests these events were hemisphere-wide, if not global. In line with previous attributions (Ljundqvist 2010, Esper et al. 2012, Marcott et al. 2013) we propose that the origin of the long-term cooling trend lies in high-latitude insolation forcing and is consistent with a 65°N Milankovitch mechanism, although further investigation into the role of Southern Hemisphere insolation forcing is also warranted. We have described a possible mechanism for the transmission of high-latitude cooling from southern high-latitudes to the tropical Pacific via intermediate water masses that are the source of upwelling in the EEP (Gu and Philander 1997). This signal should be detectable in temperature reconstructions from benthic and thermocline foraminifera in the EEP, similar to the detection of the signal in the western Pacific sub-surface (Rosenthal et al. 2013), but this remains to be seen. While a possible mechanism for transmitting this signal has been presented here, the precise origin of the Southern Hemisphere cooling remains elusive.

Tables

NOSAMS Accession ID	Depth	Radiocarbon Age (YBP)	Calibrated Date	1 sigma range	2 sigma range
OS-86755	MC42E 2-3cm	200 ± 25	>1950	N/A	N/A
OS-93340	4.94-5.48cm	805 ± 25	1611 CE	1539 - 1682 CE	1479 - 1774 CE
OS-113967	8.13-8.65cm	950 ± 20	1494 CE	1433 - 1555 CE	1401 - 1651 CE
OS-113968	11.79-12.32cm	1390 ± 15	1137 CE	1065 - 1209 CE	1018 - 1278 CE
OS-93341	14.78-15.49cm	1770 ± 25	745 CE	674 - 816 CE	616 - 908 CE
OS-93342	27.53-28.22cm	3000 ± 30	683 BCE	585-781 BCE	440 - 831 BCE
OS-93343	33.53-34.27cm	2950 ± 25	636 BCE	533-739 BCE	410-775 BCE
OS-93344	37.75-38.0cm	3150 ± 30	848 BCE	775-921 BCE	718-1046 BCE

Table 2.1. Radiocarbon data from KNR195-5 MC42C/MC42E. The first row is from core MC42E. All others are from MC42C. Radiocarbon dates were obtained from NOSAMS using specimens of *Neogloboquadrina dutertrei*. Reported radiocarbon ages were calibrated using Calib 6.1 with a Delta-R = 125±66 using the marine09.14c dataset (Stuiver and Reimer 1993/2011, Reimer et al. 2009). Because of the radiocarbon reversal below 28 cm, we chose not to consider that section of the core. Extrapolating to the ages in the reversal section, ages in the section of the core below 15.5 cm may be younger by up to 490 years.

Figures

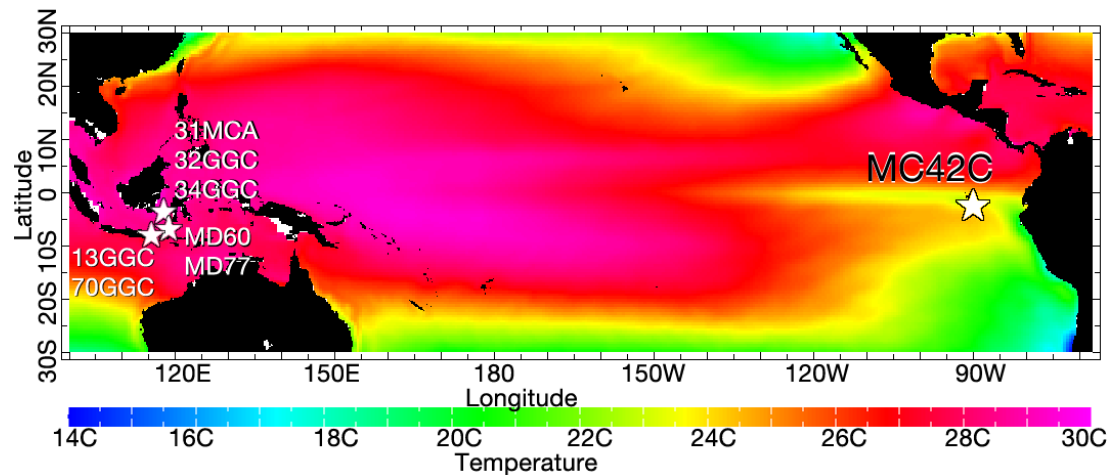


Figure 2.1. Map of the tropical Pacific showing average sea surface temperatures.

SST data from SODA 2.2.4 1871-2009 (Carton and Giese, 2010). Study location in the eastern equatorial Pacific (MC42C, this study) and core locations from the western Pacific (MD98-2160, Newton et al. 2006; MD98-2177, Newton et al. 2011; BJ8-03-34GGC, BJ8-03-32GGC, BJ8-03-31MCA, Oppo et al. 2009) indicated by stars.

Chapter 2: Sea surface cooling of the EEP during the past 2700 years

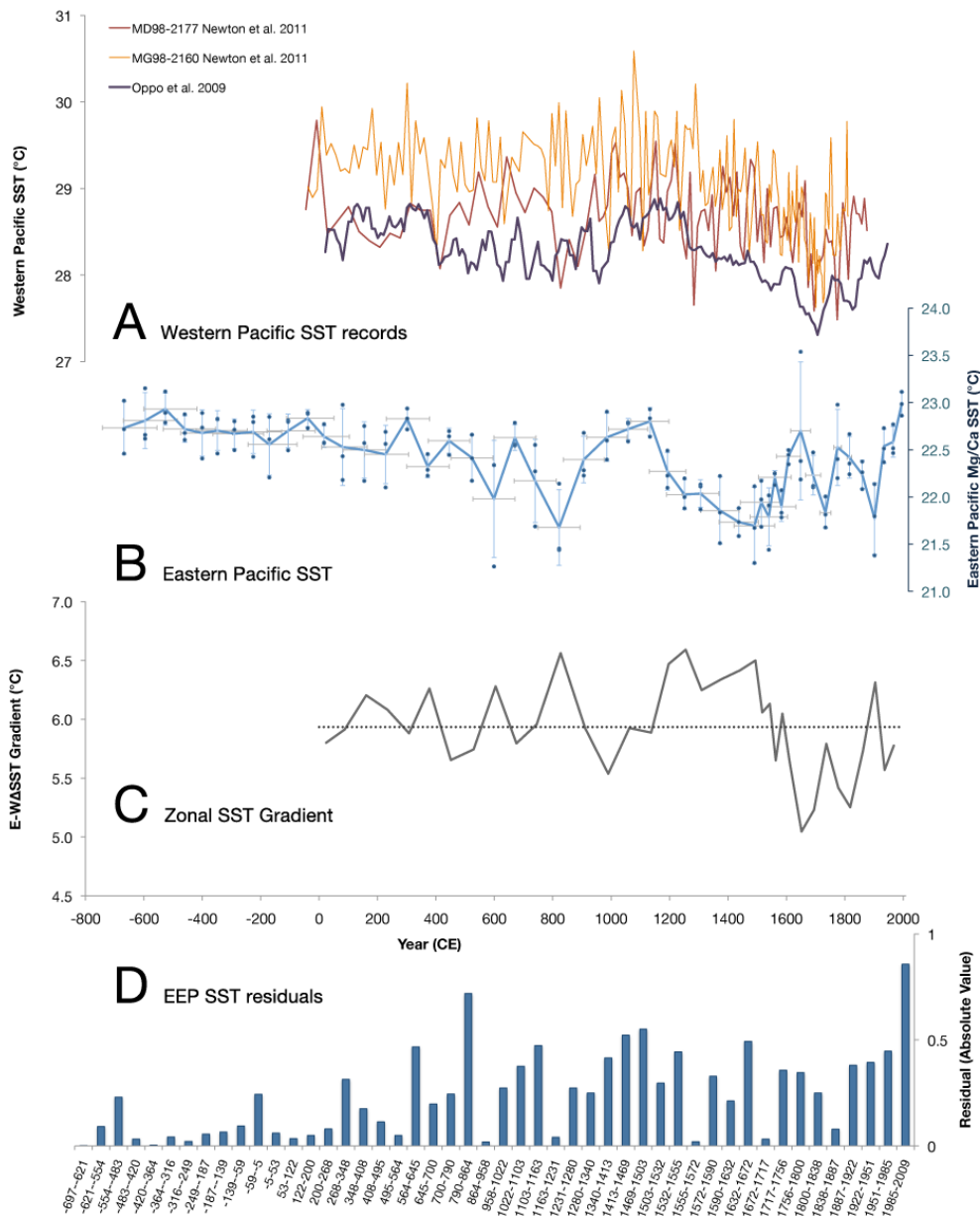


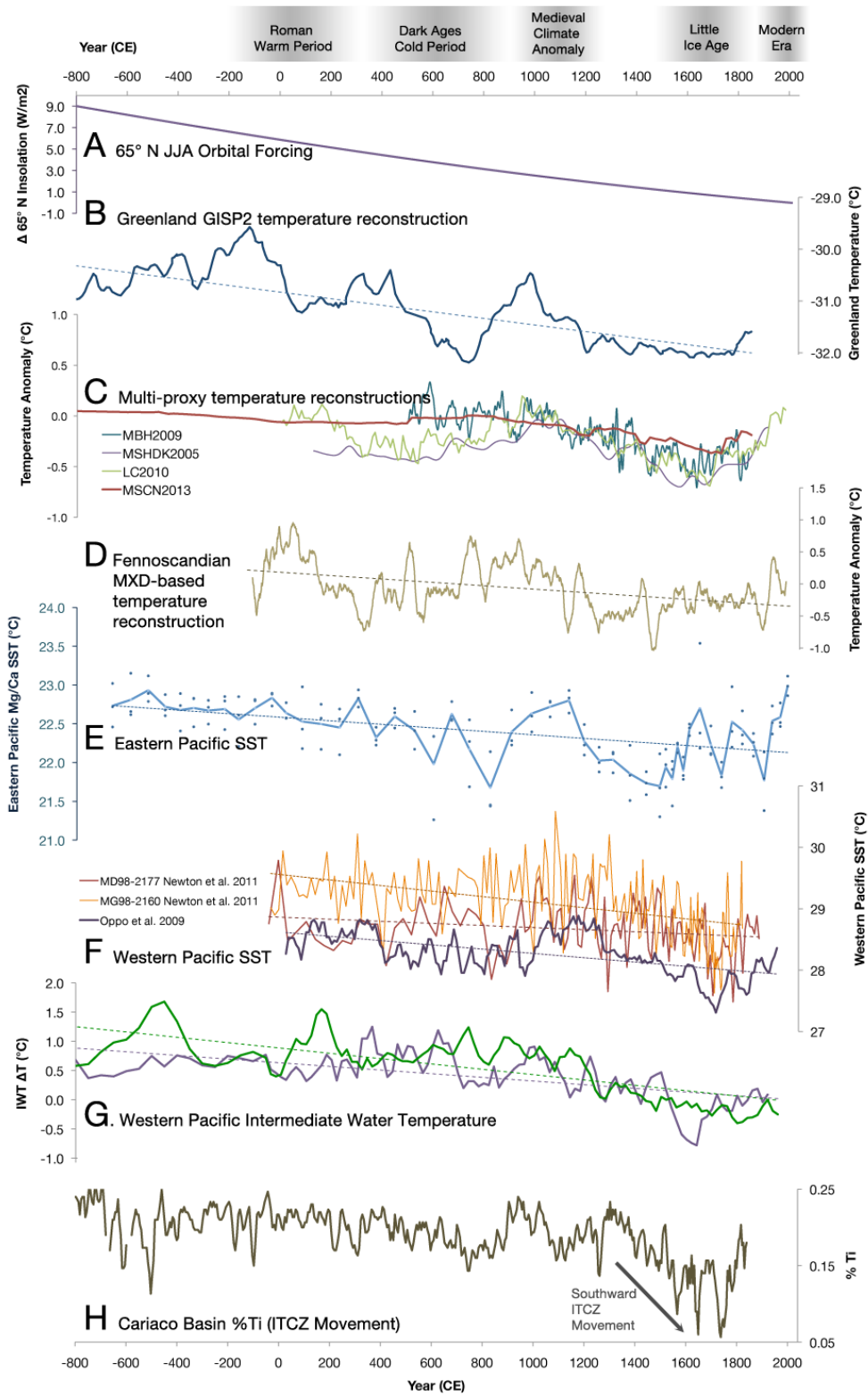
Figure 2.2 Sea surface temperature records of the past several millennia. (A)

Western Pacific Mg/Ca SST records (Composite from Oppo et al. 2009, MD89-2160 and MD98-2177 from Newton et al. 2011). **(B)** Eastern equatorial Pacific Mg/Ca SST

Chapter 2: Sea surface cooling of the EEP during the past 2700 years

(MC42C, this study). Blue line shows the SST record, with blue dots showing individual Mg/Ca SST analyses. Horizontal whiskers show 1-sigma age uncertainty, vertical whiskers indicate analytical error. **(C)** Zonal temperature gradient calculated from Oppo et al. 2009 SST composite record and MC42C EEP SST. **(D)** EEP SST residuals, calculated as the absolute value of the difference between the long-term EEP cooling trend (-0.22 °C/ky) and interval SST.

Chapter 2: Sea surface cooling of the EEP during the past 2700 years



Chapter 2: Sea surface cooling of the EEP during the past 2700 years

Figure 2.3. Comparison of climate reconstructions and SST records. **(A)** Change in 65° N June orbital forcing (purple) (Laskar 2009). **(B)** Greenland GISP2 temperature showing trend (dotted line) (Alley, 2000). **(C)** Northern Hemisphere/global multi-proxy temperature reconstructions (MSCN2013 = Marcott et al. 2013 global stack, LC2010 = Llundqvist 2010, MBH2009 = Mann et al. 2009 omitting instrumental data from 1850+, MSHDK2005 = Moberg et al. 2005). **(D)** Fennoscandia MXD based temperature reconstruction (Esper et al. 2012). **(E)** Eastern Pacific SST (MC42C, this study). **(F)** Western Pacific SST as in Figure 1 **(G)** Western Pacific Intermediate Water Temperature (IWT). Green line is temperature at 500 m, purple line is temperature at 600-900 m (Rosenthal et al. 2013) **(H)** % Titanium from Cariaco Basin sediments interpreted as tracking location of the ITCZ (Haug et al. 2001). Trends in all records are shown as dotted lines.

Chapter 3. $\delta^{13}\text{C}$ Suess effect observed in individual foraminifera from the eastern equatorial Pacific

Abstract

The carbon-13/carbon-12 isotope ratio ($\delta^{13}\text{C}$) of atmospheric CO₂ has been decreasing over the past decades due to isotopically depleted carbon from fossil fuel emissions. This decrease in $\delta^{13}\text{C}$ is known as the $\delta^{13}\text{C}$ –Suess effect, and it has been observed in atmospheric CO₂ records, oceanic records of dissolved inorganic carbon, and in biogenic marine carbonates. Here we present a record of $\delta^{13}\text{C}$ from individual *Globigerinoides ruber* foraminifera from eastern equatorial Pacific deep-sea sediments spanning the past millennium. We find that mean $\delta^{13}\text{C}$ has decreased by 0.3‰ in recent modern sediments compared to the pre-industrial era, while the $\delta^{13}\text{C}$ variance of individual shells increased steadily from a pre ~1500 CE minimum to the present day. A significant negative correlation between single-shell $\delta^{18}\text{O}$ and $\delta^{13}\text{C}$ was present in the first half of the last millennium, but was gradually eliminated toward the present day in parallel with the $\delta^{13}\text{C}$ depletion. Changes in the $\delta^{13}\text{C}$ mean, $\delta^{13}\text{C}$ variance, and $\delta^{18}\text{O}$ – $\delta^{13}\text{C}$ relationships are found to be large driven by the *ss* (*sensu stricto*), and less so by the *sl* (*sensu latu*) *G. ruber* morphotype. *G. ruber ss* is generally associated with a warmer calcification temperature and shallower depth than *sl*, implying that the $\delta^{13}\text{C}$ Suess effect signal at this site is transmitted directly from the atmosphere rather than through upwelling waters sourced from higher latitudes.

Introduction

Atmospheric CO₂ has been increasing since the beginning of the industrial revolution from a pre-industrial concentration of ~280 ppmv (parts per million by volume) (Indermühle et al. 1997) to over 400 ppmv at present day (Keeling et al. 2011), driven largely by the accumulation of CO₂ from the combustion of fossil fuels (Andres et al. 2012). In concert with this rise in CO₂, the stable isotope ratio of carbon-13 ($\delta^{13}\text{C}$) has been decreasing due to the influx of isotopically depleted fossil fuel carbon ($\delta^{13}\text{C}$ of -27‰, Keeling et al. 2011).

The creation of modern atmospheric sampling networks in the latter part of the 20th century have allowed for accurate measurements of CO₂ and carbon isotopes (Keeling, 1979). Research on the impact of anthropogenic emissions predating these networks relied on carbon isotopes to track the fate of CO₂ emitted since the beginning of the Industrial Revolution (Slocum 1955), and the residence time of that CO₂ in the atmosphere (Craig 1957; Revelle and Suess 1957). Suess (1955) recognized a decreased radiocarbon (¹⁴C) ratio in atmospheric CO₂, a phenomenon referred to as “the Suess effect” as early as 1956 (Anderson and Hayes, 1956). Slocum (1955) reported on the discovery of a secular trend toward decreasing $\delta^{13}\text{C}$ ratios in tree-rings in a report by H.S. Brown in 1952, but ¹⁴C remained the focus of carbon isotope research for the following decades. $\delta^{13}\text{C}$ was not widely used, possibly due to the mistaken belief that fossil fuel $\delta^{13}\text{C}$ and atmospheric $\delta^{13}\text{C}$ were in equilibrium (Bolin and Eriksson, 1959).

The term “Suess effect” was re-applied to the study of changing $\delta^{13}\text{C}$ in any carbon reservoir due to anthropogenic activities by Keeling in 1979. In the period since, atmospheric $\delta^{13}\text{C}$ has decreased by 0.85‰ (Keeling et al. 2011), and gas trapped in Antarctic Ice records a 1.4‰ $\delta^{13}\text{C}$ decrease since the beginning of the industrial revolution (Francey et al. 1999). The exchange of gases at the ocean surface has allowed for the transmission of this atmospheric $\delta^{13}\text{C}$ signal to the ocean via dissolved CO₂ and the dissolved inorganic carbon pool (Druffel and Benavides, 1986), which has, in turn, altered the isotopic signature of biogenic calcite. A synthesis of coral and sponge records found evidence for a $\delta^{13}\text{C}$ reduction of 0.74‰ in the Atlantic and 0.27‰ in the Pacific over the 20th century, and 1.2‰ and 0.5‰, respectively, since 1800 (Swart et al. 2010). Recent studies of corals from the Western Pacific found that $\delta^{13}\text{C}$ may be influenced by differences in depth as shallow at 10 m (Dassié et al. 2013), and evidence from Caribbean coralline sponges indicate upwelling and large scale changes in climate can also affect $\delta^{13}\text{C}$ trends (Böhm et al. 2002).

The calcitic tests of foraminifera are also sensitive to changes in $\delta^{13}\text{C}$ (Spero et al. 1988). A $\delta^{13}\text{C}$ reduction of 0.4‰ to 0.9‰ based on comparison of modern sediment-trap data and pre-industrial core-tops has been observed in foraminifera from the eastern Atlantic (Beveridge and Shackleton, 1994), Arctic (Bauch et al. 2000) and Southern Oceans (King and Howard, 2004). Foraminifera from the Gulf of Aqaba have recorded a $\delta^{13}\text{C}$ decrease of 0.42‰ since 1750 (Al-Rousan et al., 2004), and foraminifera from both sediment traps

Chapter 3: $\delta^{13}\text{C}$ Suess effect observed in individual foraminifera from the EEP

and laminated Cariaco Basin sediments record a $\delta^{13}\text{C}$ reduction of upwards of 0.75‰ since the pre-industrial era (Black et al. 2011).

These proxy records add to our understanding of the fate of emitted CO₂ and its re-uptake into the surface oceans. However, these records, as well as oceanographic surveys have shown that the rate of $\delta^{13}\text{C}$ decrease is highly variable across ocean basins and oceanographic setting (Quay et al. 1992), highlighting the need for $\delta^{13}\text{C}$ records from differing oceanographic regimes. Here we present a ~1000 year continuous record of $\delta^{13}\text{C}$ from foraminifera from a sediment multi-core retrieved near the Galápagos Islands in the eastern equatorial Pacific (EEP) cold tongue region. We analyzed individual shells of the mixed-layer dwelling foraminifera *Globigerinoides ruber* (white) to determine mean $\delta^{13}\text{C}$ and the $\delta^{13}\text{C}$ variance over the past millennium. The objectives of this study are: i) to characterize changes in $\delta^{13}\text{C}$ mean and variance in surface-dwelling foraminifera from the EEP cold tongue and determine whether they are consistent with a Suess effect; ii) to analyze $\delta^{13}\text{C} - \delta^{18}\text{O}_\text{c}$ relationships over time for insights into the causes of $\delta^{13}\text{C}$ changes; and iii) to investigate how the oceanographic setting of the EEP influences any observed Suess effect.

Oceanographic Setting

The EEP features strong, seasonably variable wind-driven upwelling (Deser and Wallace, 1992) and is a center-of-action for the El Niño Southern Oscillation (ENSO). Upwelling here is strongest during the cold season (September) and is further strengthened during

La Niña events. Warm SSTs and weaker upwelling occur in March, and upwelling slows during strong El Niño events as the thermocline deepens (Cane 1983). The upwelling water has a source in the Subantarctic Mode Waters (SAMW) which forms at ~50 °S (Rogers et al. 2003) and upwells into the tropics with a lag of several decades (Gu and Philander, 1997, McPhaden and Zhang, 2002). The strong upwelling of the EEP brings in waters with high levels of nutrients, including PO₄ (Figure 3.1), as well as high levels of dissolved inorganic carbon (DIC), remineralized carbon, and pCO₂ (Pennington et al., 2006). This region is an oceanic source of CO₂ to the atmosphere except during warm periods (e.g., El Niño events) (Feeley et al. 2006).

Materials and Methods

Sediments for this study come from multi-core KNR195-5 MC42C, which was raised near the Galápagos Islands (01° 15.58'S, 89° 41.13'W 615m, 4/4/2009, R/V Knorr) (Figure 3.1). The age model for the core is based on radiocarbon analyses presented in Chapters 1 and 2. Average sedimentation rate for the last 1000 years is 13.0 cm/ky. The core was sampled at sub-centimeter intervals representing sub-century resolution. Single shells of *G. ruber* (300-355 µm) were picked from each interval (~60 per sample) and analyzed for $\delta^{18}\text{O}$ and $\delta^{13}\text{C}$ at Lamont-Doherty Earth Observatory using a Thermo Delta V with Kiel device, and a VG Isoprime, both with dual inlets. Single-shell $\delta^{18}\text{O}$ results were presented and discussed in Chapter 1. This chapter presents an analysis of the $\delta^{13}\text{C}$ data generated simultaneously with $\delta^{18}\text{O}$. Long-term analytical precision was ±0.09‰ for

Chapter 3: $\delta^{13}\text{C}$ Suess effect observed in individual foraminifera from the EEP

$\delta^{18}\text{O}$ and 0.05‰ for $\delta^{13}\text{C}$, based on repeat analysis of the NBS-19 carbonate standard.

Approximately one standard was analyzed for every two *G. ruber* analyses.

Results

Mean $\delta^{13}\text{C}$ and isotopic equilibrium

Unlike $\delta^{18}\text{O}$ (Spero 1998), $\delta^{13}\text{C}$ in foraminiferal calcite may deviate strongly from isotopic equilibrium with the environment (Kroopnick et al. 1985), partly due to vital effects, for example from the action of photosynthetic symbionts (Spero et al. 1991). The vital effect in *G. ruber* has been estimated at -1.3-2.1‰ from sediment trap data from the eastern Atlantic (Beveridge and Shackleton, 1994) and core-top sediments in the Red Sea (Al-Rousan et al. 2004). To estimate this vital effect, we calculated the expected $\delta^{13}\text{C}$ equilibrium from Romanek et al. (1992):

$$\delta^{13}\text{C}_{\text{equilibrium}} = \delta^{13}\text{C}_{\text{seawater}} + 1.0\text{\textperthousand}$$

Data for surface $\delta^{13}\text{C}$ in the Galapagos was not readily available, but surface $\delta^{13}\text{C}$ for equatorial regions at 95 °W range from 0.81-1.11‰, and a wider survey of eastern equatorial Pacific $\delta^{13}\text{C}$ values has a range of 0.81- 1.19‰ (Laube-Lenfant and Pierre, 1994). (Note that Quay et al. (1992) report surface $\delta^{13}\text{C}$ values in excess of 1.6‰ for a region several degrees southwest of the Galapagos, and more precise location-specific $\delta^{13}\text{C}_{\text{seawater}}$ data could alter these results.) Using the geographically closest values, $\delta^{13}\text{C}_{\text{equilibrium}}$ is calculated to be 1.8-2.2‰. In our individual *G. ruber* data (Figure 2), mean $\delta^{13}\text{C}$ is 1.42‰ over the entire 20th century and 1.35‰ in the latest 20th century

Chapter 3: $\delta^{13}\text{C}$ Suess effect observed in individual foraminifera from the EEP

sediments. The calculated vital effect of -0.4‰ to -0.8‰ is less than half of that previously reported. We also note that the 20th century mean $\delta^{13}\text{C}$ from the EEP is isotopically enriched compared to *G. ruber* from the eastern Atlantic (~0.5‰, Beveridge and Shackleton, 1994), the Gulf of Aqaba (0.4‰, Al-Rousand et al. 2004), and from the Cariaco basin (0.9-1.25‰, Black et al. 2011) by 0.1-0.95‰. This is in-line with the mean difference between Atlantic and Pacific corals and sponges surveyed by Swart et al. (2010). Some of the difference in $\delta^{13}\text{C}$ from foraminifera across basins may be a function of comparing sediment trap data (Beveridge and Shackleton, 1994, Black et al. 2011) containing only contemporary foraminifera with sedimentary data that integrates climate signals over time.

Mean $\delta^{13}\text{C}$

Mean $\delta^{13}\text{C}$ values from the pre-1500 CE period range from 1.60-1.68‰ (mean 1.65‰), identical to late-Holocene $\delta^{13}\text{C}$ means of 1.61-1.68‰ from individual *G. ruber* (Koutavas et al. 2006). This stability of $\delta^{13}\text{C}$ mean values ends in the 16th century and mean $\delta^{13}\text{C}$ decreases significantly from ~1500 CE to present, with the minimum $\delta^{13}\text{C}$ of 1.35‰ occurring in the most recent sediment horizon (dated to ~1985-2009 CE) (Figure 3.2B). The mean $\delta^{13}\text{C}$ of the modern era (1850-present) is 1.42‰, significantly lower than the mean value during the Little Ice Age (LIA, 1500-1850, 1.53‰) and the pre-1500 CE period (1.65‰). These differences in mean $\delta^{13}\text{C}$ are statistically significant (student's t-test, p<0.05 for all).

Chapter 3: $\delta^{13}\text{C}$ Suess effect observed in individual foraminifera from the EEP

Using the $\delta^{13}\text{C}$ difference between our most recent sediment sample (~1985-2009, $\delta^{13}\text{C}=1.35\text{\textperthousand}$) and the pre-1500 CE average ($\delta^{13}\text{C}=1.65\text{\textperthousand}$) we quantify the magnitude of the $\delta^{13}\text{C}$ Suess effect at our site to be $0.3\text{\textperthousand}$. This magnitude is less than a $0.5\text{\textperthousand}$ magnitude observed in *G. ruber* from the eastern Atlantic (Beveridge and Shackleton, 1994) and a $0.75\text{\textperthousand}$ magnitude in *G. ruber* (pink) from the Cariaco Basin (Black et al. 2011). It is also less than a $0.43\text{\textperthousand}$ Suess effect calculated in *G. ruber* (white) from the Gulf of Aqaba (Al-Rousan et al., 2004). The predicted whole-ocean $\delta^{13}\text{C}$ decrease from an atmospheric decrease of $1.4\text{\textperthousand}$ is $0.56\text{\textperthousand}$ (Oeschger et al. 1975), largely due to isotopic disequilibrium between the ocean and atmospheric CO_2 (Lynch-Stieglitz et al. 1995). The equatorial Pacific Ocean however, has shown smaller decreases in $\delta^{13}\text{C}$ than the mid-latitudes in multi-decadal ocean surveys (Quay et al. 1992) suggesting its Suess effect signal is relatively muted. Further, strong upwelling such as that which characterizes the EEP, influences $\delta^{13}\text{C}$ through the influx of remineralized carbon in upwelled waters (Böhm et al. 1996), and opposes the penetration of the atmospheric $\delta^{13}\text{C}$ signal through supply of older subsurface waters that have not had recent contact with the atmosphere (Beveridge and Shackleton, 1994). Here, we hypothesize that the total $0.3\text{\textperthousand}$ $\delta^{13}\text{C}$ decrease observed in our record post-1500 CE is in fact the result of an atmospheric Suess effect, and not of changes in climate or local ocean dynamics. We further hypothesize that the relatively small (but robust) amplitude of the Suess effect at our site is a consequence of limited penetration of the atmospheric signal into the surface ocean due to upwelling. These hypotheses are discussed below.

Single shell $\delta^{13}\text{C}$ variance

Individual *G. ruber* $\delta^{18}\text{O}$ has been used to infer ENSO variability by virtue of the primary influence of SST on $\delta^{18}\text{O}$ of shell calcite (Chapter 1, Koutavas et al. 2006; Koutavas and Joanides, 2012). Planktonic $\delta^{13}\text{C}$, which is measured concurrently with $\delta^{18}\text{O}$, is understood to record $\delta^{13}\text{C}$ of DIC which is inversely related to nutrient concentrations and is affected by upwelling and productivity (Beveridge and Shackleton, 1994, Broecker and Maier-Reimer, 1992, King and Howard, 2004) as well as by changes in atmospheric CO₂ (Black et al., 2011, Al-Rousan et al. 2004, Beveridge and Shackleton, 1994), all of which vary both seasonally and inter-annually (due to ENSO) in the EEP (Pennington et al. 2006). During periods of strong upwelling (e.g., during La Niña events) the colder surface waters are enriched in nutrients and depleted in $\delta^{13}\text{C}$ due to the supply of remineralized DIC by the upwelled waters (Ravelo and Hillaire-Marcel, 2007).

Conversely, during periods of weak upwelling, drawdown of nutrients by biological productivity enriches the surface water $\delta^{13}\text{C}$ by preferentially utilizing the lighter ¹²C isotope for biological carbon fixation (Ortiz et al. 2000). Thus, in a similar way that single-shell $\delta^{18}\text{O}$ may be used to reconstruct the variance of SST within a population of foraminifera recovered from the sediments, single shell $\delta^{13}\text{C}$ may be a useful indicator of variations in the supply and utilization of nutrients to the sea surface via upwelling.

Because cooling and the supply of nutrients to the surface are intimately related, we expected that single-shell *G. ruber* $\delta^{18}\text{O}$ and $\delta^{13}\text{C}$ should be negatively correlated reflecting the association of cold SST (high $\delta^{18}\text{O}$) with high nutrients (low $\delta^{13}\text{C}$).

Similarly, if a change in ENSO variability occurs which enhances the $\delta^{18}\text{O}$ variance due

Chapter 3: $\delta^{13}\text{C}$ Suess effect observed in individual foraminifera from the EEP

to greater SST variance, we anticipated a concomitant increase in $\delta^{13}\text{C}$ variance reflecting the greater variability in nutrient states. On the other hand, an anthropogenic Suess effect has the potential to interfere and overprint these relationships. For example, invasion of $\delta^{13}\text{C}$ -depleted fossil fuel carbon to the surface ocean from the atmosphere is likely enhanced during non-upwelling conditions (e.g. El Niño) having the potential to overprint the high- $\delta^{13}\text{C}$, nutrient-depleted signature of surface waters during such events. In this case the negative correlation between $\delta^{18}\text{O}$ and $\delta^{13}\text{C}$ in individual shells, reflecting the coupled variability of nutrients and SST, would be expected to weaken or vanish as an artifact of the Suess effect.

The single-shell data from our site indicate a steady increase ($R=0.78$, $p<<0.05$) in $\delta^{13}\text{C}$ variance beginning in the 16th century that continues in the 20th century (Figure 3.2C). $\delta^{13}\text{C}$ variance in the modern era (1850-2009 CE) is significantly higher than the LIA (1500-1850 CE) and the pre-1500 CE era (F-test $p<<0.05$ for both). The increase in variance appears to be driven primarily by depleted $\delta^{13}\text{C}$ values, especially values less than 0.8‰, which are uncommon before 1500 CE but are found in every interval thereafter (Figure 3.2 A). The pattern of increasing $\delta^{13}\text{C}$ variance through the millennium is similar to our previous finding of increasing $\delta^{18}\text{O}$ variance (Chapter 1), which was interpreted to reflect ENSO activity. In the period before 1850 CE, $\delta^{18}\text{O}$ variance and $\delta^{13}\text{C}$ variance of individual *G. ruber* shells are significantly correlated ($r=0.53$, $p<0.05$), although this correlation is reduced and not statistically significant at the 95% confidence level ($r=0.40$, $p=0.054$) if the results from 1850-2009 CE are included. The parallel

Chapter 3: $\delta^{13}\text{C}$ Suess effect observed in individual foraminifera from the EEP

increase in both $\delta^{18}\text{O}$ and $\delta^{13}\text{C}$ variance post 1500 CE, at first sight suggests that they may be driven by a common cause, related to an increase in ENSO activity. However, the most active ENSO period, in the 18th century, does not display the greatest $\delta^{13}\text{C}$ variance, while the modern era does not have particularly high ENSO activity but does have the highest $\delta^{13}\text{C}$ variance. Furthermore, a more careful examination of the paired $\delta^{18}\text{O}$ - $\delta^{13}\text{C}$ relationship in individual shells, discussed below, suggests that ENSO modulation cannot be the only factor affecting the $\delta^{13}\text{C}$ changes, and that an atmospheric Suess effect has likely overprinted the $\delta^{13}\text{C}$ data.

$\delta^{13}\text{C} - \delta^{18}\text{O}_c$ relationship

Modulations of the $\delta^{13}\text{C}$ - $\delta^{18}\text{O}$ relationship in single *G. ruber* shells provide further insight into the causes of the reduction in mean $\delta^{13}\text{C}$ (Figure 3.3). Before 1500 CE, a significant negative correlation ($r=-0.32$, $p<0.05$) exists between $\delta^{13}\text{C}$ and $\delta^{18}\text{O}$, consistent with an upwelling mechanism driving cooling (high $\delta^{18}\text{O}$) and nutrient enrichment (low $\delta^{13}\text{C}$) in surface waters (Figure 3.3A). A similar relationship was found earlier in *G. ruber* single-shell isotope data from the late Holocene (Koutavas et al. 2006; Figure 3.3E and 3F), and is consistent with the relationship observed in live culture experiments (Spero et al. 1988). The $\delta^{13}\text{C}$ - $\delta^{18}\text{O}$ relationship changes during the LIA (1500-1850 CE), resulting in the correlation (r -value) losing significance (Figure 3B and Figure 3.4). The loss of $\delta^{13}\text{C}$ - $\delta^{18}\text{O}$ correlation persists into the modern era (1850-2009 CE) (Figure 3C, Figure 4).

Chapter 3: $\delta^{13}\text{C}$ Suess effect observed in individual foraminifera from the EEP

The changed relationship of $\delta^{13}\text{C}$ – $\delta^{18}\text{O}$ provides a test for distinguishing between climate versus Suess effect as driver of the $\delta^{13}\text{C}$ signal. The decrease of mean $\delta^{13}\text{C}$ beginning in the LIA, if related to ocean dynamics, would require an increase in mean upwelling rates and regional SST cooling. Our Mg/Ca SST reconstructions however (Chapter 1) indicate the opposite. Regional warming was established at the onset of the LIA, accompanied by a reduced zonal SST gradient and an enhancement of ENSO activity inferred from single-shell $\delta^{18}\text{O}$ variance. The increase in ENSO variability itself during the LIA leads to expectation of greater shell $\delta^{13}\text{C}$ variance due to more variable supply of upwelled nutrients in relation to El Niño and La Niña events. Such an increase in $\delta^{13}\text{C}$ variance is in fact observed beginning ~1500 CE and continuing to present day. The same mechanism however (greater ENSO activity) would be expected to strengthen (or at least maintain) the $\delta^{13}\text{C}$ – $\delta^{18}\text{O}$ negative correlation in individual shells evident pre-1500 CE (Figure 3A). Strong upwelling (La Niña conditions) would induce more $\delta^{13}\text{C}$ -depleted, $\delta^{18}\text{O}$ -enriched values, while El Niño conditions would have the opposite effect. Overall, the existing pre-1500 CE relationship between $\delta^{13}\text{C}$ and $\delta^{18}\text{O}$ should thus be reinforced or preserved during the LIA. However, the opposite is observed: a breakdown of the $\delta^{13}\text{C}$ – $\delta^{18}\text{O}$ correlation steadily unfolded over the latter half of the millennium (Figures 3B, 3C, and 4). This suggests that some other factor has overprinted the $\delta^{13}\text{C}$ signal, altering its anticipated relationship with $\delta^{18}\text{O}$. We posit that this factor is the anthropogenic $\delta^{13}\text{C}$ Suess effect.

Chapter 3: $\delta^{13}\text{C}$ Suess effect observed in individual foraminifera from the EEP

The change in the $\delta^{13}\text{C}$ - $\delta^{18}\text{O}$ relationship also suggests the transmission path of the $\delta^{13}\text{C}$ signal to the EEP. Upwelling waters in the EEP have their source at $\sim 50^\circ\text{S}$ in the South Pacific Ocean (Rogers et al. 2003). Atmospheric tracers in these waters suggest a transit time on the order of several decades (McPhaden and Zhang 2002), and provide a possible pathway for the transmission of the $\delta^{13}\text{C}$ signal from the atmosphere. The reversal of the $\delta^{13}\text{C}$ - $\delta^{18}\text{O}$ relationship suggests increased frequency of cold, $\delta^{13}\text{C}$ enriched individuals, or higher frequency warm, $\delta^{13}\text{C}$ -depleted individuals (or both). A $\delta^{13}\text{C}$ Suess effect signal in upwelling waters would most strongly affect cooler dwelling foraminifera, reducing $\delta^{13}\text{C}$ in foraminifera enriched in $\delta^{18}\text{O}$, but this is not evident from the $\delta^{13}\text{C}$ - $\delta^{18}\text{O}$ relationship. However, foraminifera from warmer water show $\delta^{13}\text{C}$ depletion, thus indicating the $\delta^{13}\text{C}$ signal is being transmitted directly via ocean-atmosphere gas exchange during warm conditions rather than via upwelling. Studies of pCO_2 in the EEP provide support for this mechanism. The EEP is a source of CO_2 to the atmosphere except during low-upwelling intervals such as warm El Niño events (Feeley et al. 2006). High pCO_2 hinders assimilation of the atmospheric $\delta^{13}\text{C}$ signal during upwelling (cold) periods. During warm, non-upwelling periods, lower pCO_2 allows for more gas exchange with the atmosphere and facilitates the transmission of the $\delta^{13}\text{C}$ -Suess signal into the surface ocean. On this basis we hypothesize that the observed $\delta^{13}\text{C}$ -Suess effect's source is air-sea gas mixing in the EEP rather than via upwelling waters.

***G. ruber* morphotypes**

Chapter 3: $\delta^{13}\text{C}$ Suess effect observed in individual foraminifera from the EEP

Additional evidence to support this hypothesis comes from observed differences in *G. ruber* morphotypes – *ss* are considered warmer and shallower, while *sl* are thought to prefer somewhat cooler and deeper waters (Wang 2000, Lowemark et al. 2005). Mean *ss* $\delta^{18}\text{O}$ is on average -0.32‰ depleted compared to *sl* (Chapter 1, Appendix A) through all sample intervals (Figure 3.5 C), supporting a warmer and possibly shallower habitat. The mean $\delta^{13}\text{C}$ values of the two morphotypes are identical before ~1500 CE (Figure 5A), but diverge after ~1500 CE (Figure 3.5 A). This suggests that the observed differences in $\delta^{13}\text{C}$ between morphotypes are not due to biological factors (e.g. vital effects) but reflect exposure to DIC pools with differing $\delta^{13}\text{C}$ composition after ~1600 CE. The $\delta^{13}\text{C}$ trend of *sl* since 1500 CE is negative but not statistically significant (-0.02‰/century, $p>0.05$), while that of *ss* is larger and statistically significant (-0.06‰/century, $p<0.05$) (Figure 5A). The different evolution of $\delta^{13}\text{C}$ in the two morphotypes indicates that the decline in mean $\delta^{13}\text{C}$ in our data is primarily driven by the *ss* morphotype, which occupies a warmer, surface-most habitat.

The $\delta^{13}\text{C}$ variance signal is also largely driven by the *ss* morphotype (Figure 5B). Most of the increase in $\delta^{13}\text{C}$ variance of *ss* post-1500 CE is driven by the presence of extreme low- $\delta^{13}\text{C}$ outliers (Figure 2A) which we attribute to the Suess effect. The fact that similar outliers are much less prevalent in the *sl* morphotype, which is understood to inhabit a slightly deeper and colder habitat, argues that the Suess effect signal is transmitted directly from the atmosphere above, rather than by upwelled waters from below.

Chapter 3: $\delta^{13}\text{C}$ Suess effect observed in individual foraminifera from the EEP

The difference in morphotype response to $\delta^{13}\text{C}$ is also reflected in their $\delta^{13}\text{C}$ - $\delta^{18}\text{O}$ relationships (Figure 3.6). Before 1500 CE, both morphotypes had similar negative relationships (Figure 3.6A). During the LIA (1500-1850 CE) *sl* maintained this negative relationship, although somewhat weakened, while in *ss* it disappeared (Figure 6B). By the modern era (1850-2009 CE) the $\delta^{13}\text{C}$ - $\delta^{18}\text{O}$ relationship was further weakened in *sl*, while in *ss* it switched sign and became weakly positive (Figure 6C). That the change in $\delta^{13}\text{C}$ mean, $\delta^{13}\text{C}$ variance and $\delta^{13}\text{C}$ - $\delta^{18}\text{O}$ relationship are all most strongly expressed in the warmer, shallower *ss* morphotype provides compelling support to the hypothesis of an atmospheric, rather than upwelling, source for the $\delta^{13}\text{C}$ Suess effect.

Shell weight effect on $\delta^{13}\text{C}$

Foraminiferal $\delta^{13}\text{C}$ is size-sensitive due to growth-related fractionation (Berger et al. 1978, Oppo and Fairbanks, 1995, Elderfield et al. 2002), and common practice is to analyze the largest size-fraction that contains abundant adult, and thus slower-growing, specimens (Ravelo and Hillaire-Marcel, 2007). In this study we selected individuals from the 300-355 μm size-fraction, consistent with other studies (Beveridge and Shackleton, 1994; Al-Rousan et al., 2004). Shell weights were recorded for ~90% of the analyzed specimens and we use these data here to test for potential mass/size effects in single-shell $\delta^{13}\text{C}$ that might bias our results. We observe a weak but significant positive correlation between shell mass and $\delta^{13}\text{C}$ of 0.036‰/ μg , resulting in a difference of 0.51‰ across the total mass range ($p < 0.05$, Figure 3.7). To determine the effect this may have on mean $\delta^{13}\text{C}$, we calculated the average mass for the pre-1500 CE intervals, the

Chapter 3: $\delta^{13}\text{C}$ Suess effect observed in individual foraminifera from the EEP

LIA, and modern era (Table 3.2). Modern era *G. ruber* are, on average lighter than those from the pre-1500 CE and LIA periods by 0.85 μg . The difference in mass from pre-1500 CE to modern samples can thus account for just 0.03‰, or 10% of the observed overall decrease in $\delta^{13}\text{C}$. We therefore maintain that ~90% of the recorded $\delta^{13}\text{C}$ signal is due to the anthropogenic Suess effect.

Discussion

The changes that are observed in $\delta^{13}\text{C}$ mean and variance occur concurrently with a re-organization of EEP circulation and increased ENSO variance at ~1500 CE, in what was identified as a “Mid-Millennium Shift” (MMS) in ocean-atmosphere circulation (Chapter 1). During the MMS our reconstructions suggest that the EEP experienced regional warming, enhanced ENSO activity and a weakening of the mean zonal SST gradient across the Pacific. These changes persisted through most of the LIA (1500-1850 CE), which could be characterized as an “El Niño-like” mean state with amplified interannual ENSO. This raises the question, are the observed $\delta^{13}\text{C}$ signals, which also begin to be expressed just after ~1500 CE, a result of circulation changes rather than a Suess effect? This question was partly addressed in the results section above, but here we elaborate on it more fully. The decreasing trend in mean $\delta^{13}\text{C}$ is inconsistent with a transition to an “El Niño-like” mean circulation state which would instead predict a mean decrease in nutrient upwelling and increase in mean $\delta^{13}\text{C}$. Furthermore the decreasing $\delta^{13}\text{C}$ trend post-1500 CE continues and intensifies into the modern era (Figure 2B) with no obvious analogue in the oceanographic reconstructions of SST and zonal gradient (Chapter 1).

The increase in single-shell $\delta^{13}\text{C}$ variance becomes established at about the same time as the increase in $\delta^{18}\text{O}$ variance (Figure 2C) but follows a different evolution. The $\delta^{13}\text{C}$ variance increases almost monotonically through the present, while the $\delta^{18}\text{O}$ variance has a peak in the 18th century and is followed by more intermediate values. Adding to the different evolution of $\delta^{13}\text{C}$ and $\delta^{18}\text{O}$ across this interval, we observe a significant change in the skewness of individual $\delta^{13}\text{C}$ data, with negative skewness becoming established after ~1500 CE. This skewness indicates that negative $\delta^{13}\text{C}$ departures extending farther from the mean are becoming more frequent, an observation which is evident in the raw data (Figure 2A). On the other hand there is no significant signal indicating a corresponding change in skewness of $\delta^{18}\text{O}$ values. While the increasing variance in both isotopes post-1500 CE may well have been initiated by greater ENSO activity, a separate process appears to have independently influenced $\delta^{13}\text{C}$ but not $\delta^{18}\text{O}$. This process has resulted in a near-monotonic decrease in mean $\delta^{13}\text{C}$, increase in $\delta^{13}\text{C}$ variance, and in negative $\delta^{13}\text{C}$ skewness, features that do not have discernible analogues in $\delta^{18}\text{O}$. The decoupling of $\delta^{13}\text{C}$ and $\delta^{18}\text{O}$ post-1500 CE is also clearly evident in the evolving and diminishing (negative) correlation of paired $\delta^{13}\text{C}$ and $\delta^{18}\text{O}$ data (Figures 3.3 and 3.6). This pattern further bolsters the argument that a separate process, preferentially affecting $\delta^{13}\text{C}$, has overprinted the $\delta^{13}\text{C}$ - $\delta^{18}\text{O}$ relationship expected from ocean dynamics, which was in fact detectable pre-1500 CE. Together this evidence suggests climatic or ocean-dynamical factors are not the root cause of the $\delta^{13}\text{C}$ signals reconstructed here, and instead support the hypothesis that the decline in mean $\delta^{13}\text{C}$ is a result of a Suess effect.

Chapter 3: $\delta^{13}\text{C}$ Suess effect observed in individual foraminifera from the EEP

This does not rule out however that climatic or ocean-dynamical effects are also imprinted in these data. The net signal revealed here may well be a combination of a Suess effect superimposed on such processes. On the basis of our data alone it is not possible to further parse out the relative contribution of such factors in a more quantitative way.

The $\delta^{13}\text{C}$ -Suess effect observed in the EEP is smaller than that observed in other studies of *G. ruber* (Beveridge and Shackleton, 1994, Al-Rousan et al. 2004, Black et al. 2011) and from model predictions (Oeschger et al. 1975). Changes in global pCO₂ may have played a role, as changes in surface water pCO₂ affect [CO₃²⁻] (Bijma et al. 1999; Spero et al. 1997). While pCO₂ in the EEP is estimated to be increasing in the last decades (Feeley et al. 2006), pCO₂ in the EEP is highly volatile and subject to large seasonal and interannual variations based on upwelling strength, ENSO variability, and the Pacific Decadal Oscillation (Feeley et al. 2006, Takahashi et al. 2009). While the atmospheric increase in pCO₂ has likely had an effect on surface waters (Takahashi et al. 2009), the true long-term trend and relationship to atmospheric pCO₂ remains unclear.

The EEP is dominated by highly variable and strong upwelling (Deser and Wallace, 1992). Cooler and older upwelling waters tend to have more pCO₂, higher DIC, and lower $\delta^{13}\text{C}$ than non-upwelling waters (Gruber et al. 1999, Pennington et al. 2006), and the elevated pCO₂ levels make the EEP a source of CO₂ to the atmosphere except during

Chapter 3: $\delta^{13}\text{C}$ Suess effect observed in individual foraminifera from the EEP

the warmest El Niño events (Feeley et al. 2006). Elevated pCO₂ limits the ability of atmospheric CO₂ to mix in to the ocean surface and penetrate into the mixed layer (Feeley et al. 2006), and upwelling has been implicated in attenuating the $\delta^{13}\text{C}$ Suess effect in thermocline species (Beveridge and Shackleton, 1994). We propose that the strong upwelling in the EEP likewise reduces the magnitude of the $\delta^{13}\text{C}$ Suess effect by limiting the ability of atmospheric $\delta^{13}\text{C}$ to influence the mixed layer.

The influence of an atmospheric $\delta^{13}\text{C}$ signal, rather than an upwelling $\delta^{13}\text{C}$ signal is supported by observed differences in *G. ruber* morphotype mean, variance and $\delta^{13}\text{C} - \delta^{18}\text{O}_\text{c}$ relationships. $\delta^{18}\text{O}_\text{c}$ for *sl* morphotypes suggests a cooler habitat, which can indicate differences in depth, seasonality, or both, compared to the habitat of *ss* morphotypes. In chapter 4, the mean $\delta^{18}\text{O}$ of the *ss* morphotype is observed to be consistent with a slightly shallower depth habitat than that inferred from *sl*, consistent with previous researchers (Wang 2000, Löwemark et al. 2005). A small $\delta^{13}\text{C}$ -Suess effect and little change in variance are observed in *sl* compared to warmer *ss* morphotypes. During warmer periods, upwelling lags and the emission of CO₂ to the atmosphere in the EEP is reduced (Feeley et al. 2006), permitting better mixing of atmospheric CO₂ into the surface layer and possibly allowing for transmission of the atmospheric $\delta^{13}\text{C}$ signal into the surface ocean. Therefore, shallower and warmer *ss* morphotypes would be more immediately affected by the $\delta^{13}\text{C}$ signal. On the other hand, cooler- and deeper-dwelling *sl* morphotypes may be more influenced by the isotopic signature of upwelling water, with high pCO₂ that limits atmospheric influence. Thus the *ss* morphotype more directly

Chapter 3: $\delta^{13}\text{C}$ Suess effect observed in individual foraminifera from the EEP

reflects changes in atmospheric $\delta^{13}\text{C}$, while the *sl* morphotype is indicative of upwelling influence. Therefore changes in $\delta^{13}\text{C}$ mean and variance driven by the *ss* morphotype support the hypothesis of an atmospheric, rather than upwelling, origin of the $\delta^{13}\text{C}$ Suess signal. This is supported by observed shifts in the $\delta^{13}\text{C}$ – $\delta^{18}\text{O}_\text{c}$ relationship. As atmospheric CO₂ has become $\delta^{13}\text{C}$ depleted, the warmer-dwelling *ss* morphotypes have become more affected (Figure 3.3 C and Figure 3.6), but the cooler dwelling *sl* do not show the same response.

Bioturbation, or the mixing of sediments from younger layers into older layers (and vice versa), may play a role in the attenuation of the $\delta^{13}\text{C}$ signal and in its early onset. The decline in mean $\delta^{13}\text{C}$ begins before atmospheric records show significant changes in $\delta^{13}\text{C}$ (Figure 3.2 D). While we have found evidence for limited bioturbation in the agreement of $\delta^{18}\text{O}_\text{c}$ variance with modern SST variability (Chapter 1, Appendix A Figure S5), some mixing of sediments is expected to occur in non-laminated sediments (e.g., Black et al. 2011). Mean annual dissolved oxygen levels at this site are relatively low at 500 m depth (<1.0 ml/L) based on the World Ocean Atlas 09 oxygen surveys (Garcia et al. 2010), which may limit but not completely prevent bioturbation (Levin 2003). Downward mixing of some $\delta^{13}\text{C}$ -depleted individuals may make the onset of the Suess effect appear earlier, and its evolution to appear more gradual and drawn out, but may also indicate that some of the earliest observed change is related to climatic events. However, the predicted $\delta^{13}\text{C}$ response to the observed climatic changes in ocean circulation is not recorded in the foraminifera $\delta^{13}\text{C}$ after the climate shift, indicating any changes associated with climate

Chapter 3: $\delta^{13}\text{C}$ Suess effect observed in individual foraminifera from the EEP

have been overprinted by the atmospheric Suess effect. We also note that there appears to be little mixing between pre-1500 and post-1500 CE sediments, as the change in mean $\delta^{13}\text{C}$ is relatively sharp, and there is complete absence of strongly depleted $\delta^{13}\text{C}$ individuals in the intervals immediately preceding 1500 CE. The nature of the sedimentary record will also tend to attenuate rapidly changing signals. The depletion of $\delta^{13}\text{C}$ was accelerating through the 20th century based on atmospheric and high-resolution sedimentary records (Keeling et al. 2011, Black et al. 2011) and the change of $\delta^{13}\text{C}$ over the past 30 years (-0.85‰) is ~60% of the 1.4‰ $\delta^{13}\text{C}$ decrease observed over the last 300 years (1.4‰, Francey et al. 1999). As the resolution of sampling intervals in modern-era MC42C sediments averages 34 years, the rapid changes are integrated over that period, attenuating the signal.

Conclusion

The change in carbon isotope ratios in the atmosphere as a result of fossil fuel burning during the industrial revolution has greatly influenced the isotopic signature of carbon in the oceans as recorded by biogenic calcite. We find that climatic change, ENSO variability, the carbonate-ion effect, and mass effects cannot adequately explain the observed decrease in mean $\delta^{13}\text{C}$ at our Galápagos site. We can therefore conclude that the 0.3‰ reduction in mean $\delta^{13}\text{C}$ is largely due to the Suess effect. The highly dynamical nature of the EEP can potentially exert major influence on the magnitude of the Suess effect by limiting its downward penetration from the atmosphere through upwelling of older waters from below. On the other hand, upwelling itself may transmit a Suess effect signal from higher latitudes where the upwelled waters have their source. Our data are

Chapter 3: $\delta^{13}\text{C}$ Suess effect observed in individual foraminifera from the EEP

most consistent with atmospheric rather than oceanic (upwelling) transmission of the $\delta^{13}\text{C}$ Suess to the surface waters around the Galápagos. While we find possible evidence for the transmission of long-term temperature signals to the EEP from source waters via upwelling (Chapter 2), analysis of the $\delta^{13}\text{C}$ record does not support this pathway as the primary source of the $\delta^{13}\text{C}$ signal. It is possible that the $\delta^{13}\text{C}$ signature of upwelling waters is removed via remineralization and biological processes (Pennington et al. 2006) before reaching the surface waters of the EEP, explaining the muted expression of the $\delta^{13}\text{C}$ signal in deeper foraminifera. The relative attenuation of the subsurface (*sl*) $\delta^{13}\text{C}$ signal appears to be due to the influence of upwelling and out-gassing of CO₂ in the EEP, which limits the influence of the atmosphere on the $\delta^{13}\text{C}$ in foraminifera during cool upwelling conditions. These results demonstrate the need to obtain long-term detailed records of $\delta^{13}\text{C}$ from various oceanographic domains in order to fully characterize the atmosphere-ocean carbon exchange dynamics over the industrial period.

Figures

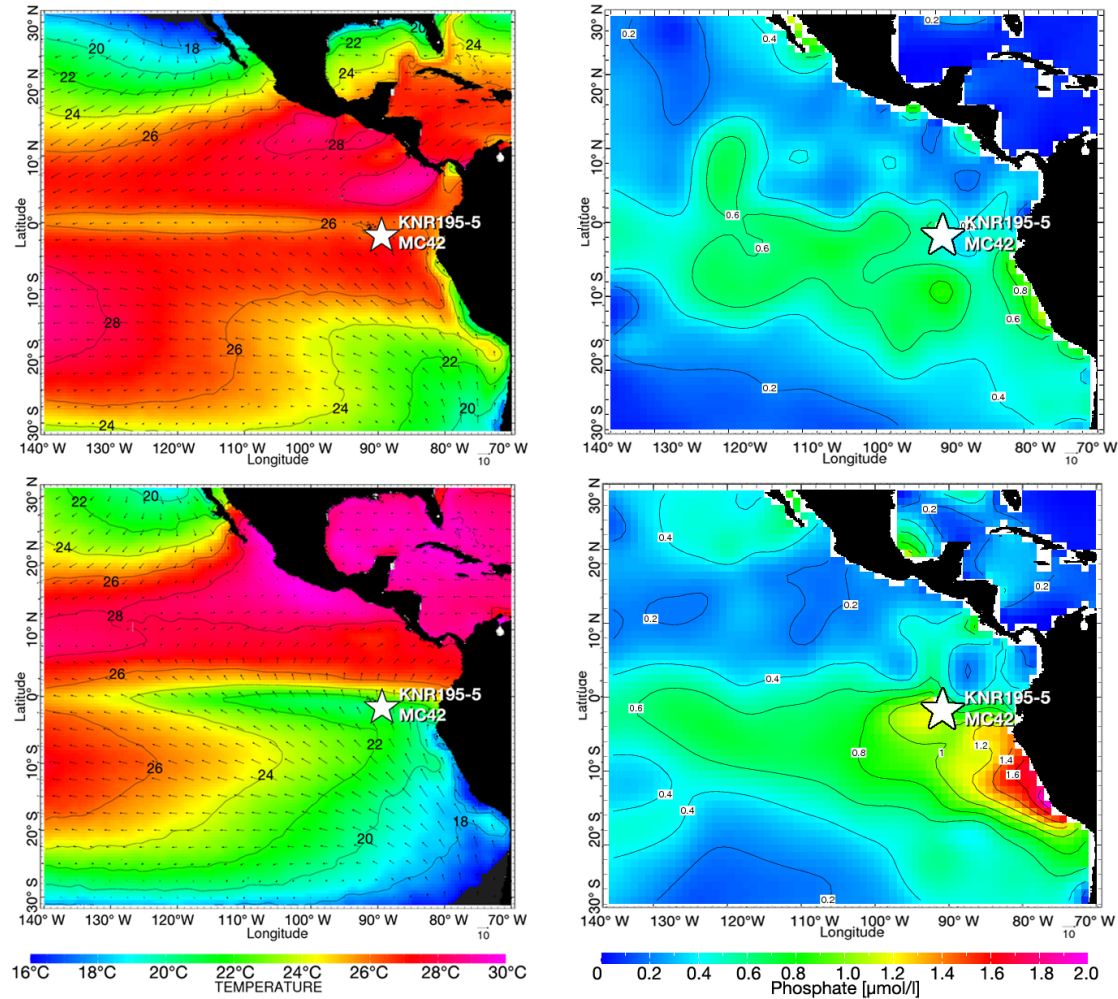


Figure 3.1. Map of the study location. Top panels show March temperature (left) and phosphate concentrations (right). Phosphate concentrations are higher during periods of upwelling. Bottom panels show September temperature (left) and phosphate (right). During periods of colder temperatures, more phosphate is present at the surface, indicating stronger upwelling. Mean SST is from SODA 2.1.6 1981-2008 (Carton and Geise 2008); 1000 mb wind are from NOAA NCEP-NCAR CDAS 1981-2009 (Kalnay et al. 1996); Phosphate data from WOA09 (Garcia et al. 2010).

Chapter 3: $\delta^{13}\text{C}$ Suess effect observed in individual foraminifera from the EEP

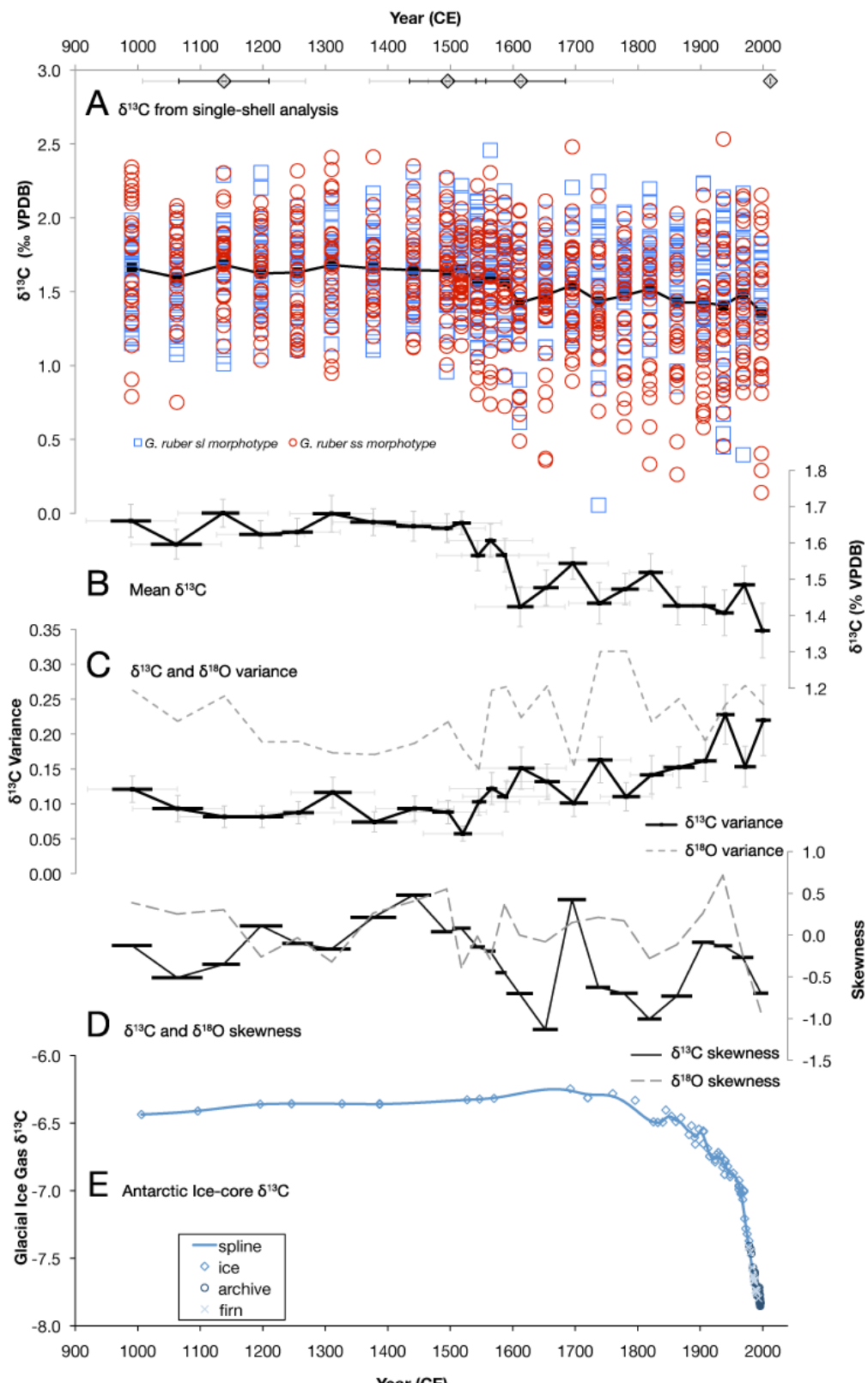


Figure 3.2. $\delta^{13}\text{C}$ records from the past millennium. (A) All individual foraminifera $\delta^{13}\text{C}$ values from MC42C. Red circles represent *G. ruber ss* morphotype. Blue squares show *sl* morphotypes. Black line shows the $\delta^{13}\text{C}$ mean. (B) Mean $\delta^{13}\text{C}$ for each sample interval. The width of the bar indicates the interval duration. Vertical whiskers are the standard error of the mean, horizontal whiskers represent the 1-sigma age error. (C) $\delta^{13}\text{C}$ and $\delta^{18}\text{O}$ variance for each sample interval. The width of the bar for $\delta^{13}\text{C}$ indicates interval duration, vertical whiskers are the standard error of the variance. Horizontal whiskers as above. (D) $\delta^{13}\text{C}$ and $\delta^{18}\text{O}$ skewness. The width of the bar for $\delta^{13}\text{C}$ shows the interval duration. (E) Atmospheric $\delta^{13}\text{C}$ from Antarctic Ice gases (Francey et al. 1999). Diamonds at the top of the figure show ^{14}C age control points. Black whiskers indicate 1-sigma range, gray whiskers indicate the 2-sigma range. The black square at 2009 represents the observed intact core-top.

Chapter 3: $\delta^{13}\text{C}$ Suess effect observed in individual foraminifera from the EEP

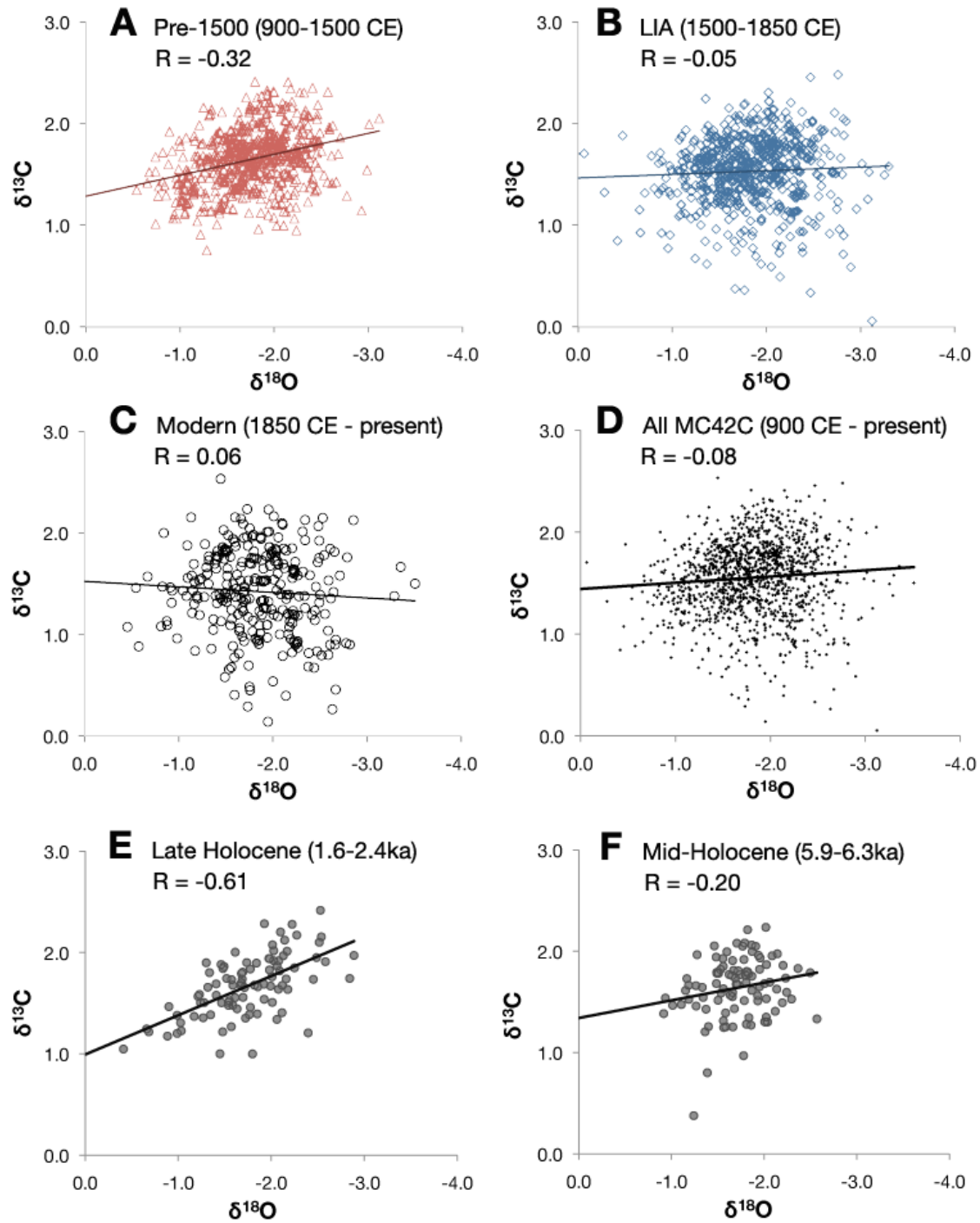


Figure 3.3. *G. ruber* $\delta^{13}\text{C} - \delta^{18}\text{O}_c$ relationship. (A) Pre-1500 CE. The trend is from lower-left (cooler, more $\delta^{13}\text{C}$ depleted) to upper right (warmer, more $\delta^{13}\text{C}$ enriched, $R = -0.32$, $p < 0.05$). (B) LIA (1500-1850). Trend line $p > 0.05$. The trend is no longer

Chapter 3: $\delta^{13}\text{C}$ Suess effect observed in individual foraminifera from the EEP

significant. **(C)** Modern (1850-present). The trend line is now reversed from pre-1500 (A) and mid-to-late Holocene (D, E), $p>0.05$ **(D)** All $\delta^{13}\text{C} - \delta^{18}\text{O}_\text{c}$ value pairs from MC42C, 900 CE – present. ($p<0.05$) **(E)** Late Holocene (1.6-2.4 ka) from Koutavas et al. 2006. **(F)** Mid-Holocene (5.9-6.3 ka) from Koutavas et al. 2006.

Chapter 3: $\delta^{13}\text{C}$ Suess effect observed in individual foraminifera from the EEP

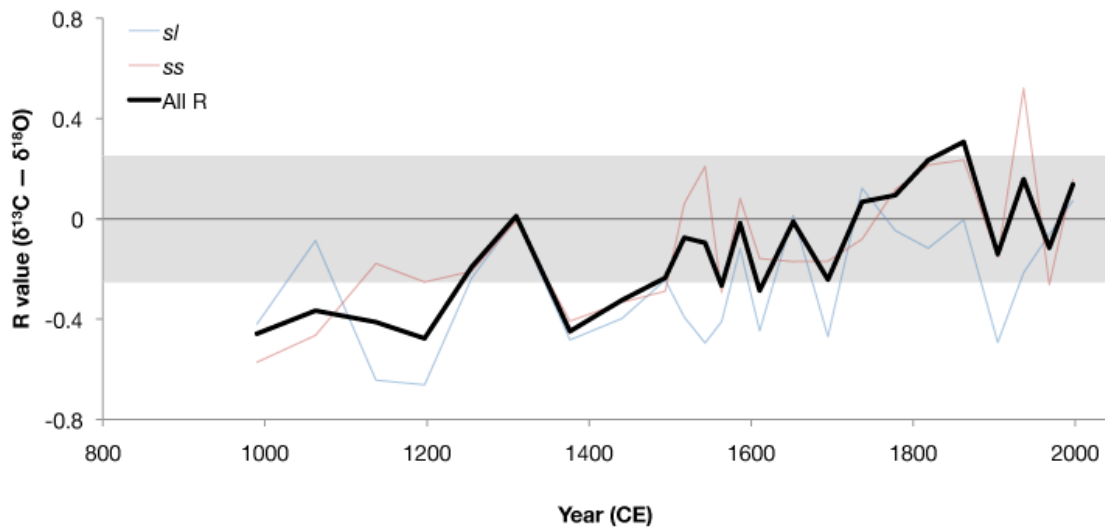


Figure 3.4. $\delta^{13}\text{C} - \delta^{18}\text{O}_c$ R – values for each sampled interval. Black line shows the increase in $\delta^{13}\text{C}-\delta^{18}\text{O}_c$ R-values over time. R values for ss and sl *G. ruber* morphotypes are shown as thin red and blue lines, respectively. The area shaded in gray represents R-values that are not statistically significant (52<N<61, Bartz 1999).

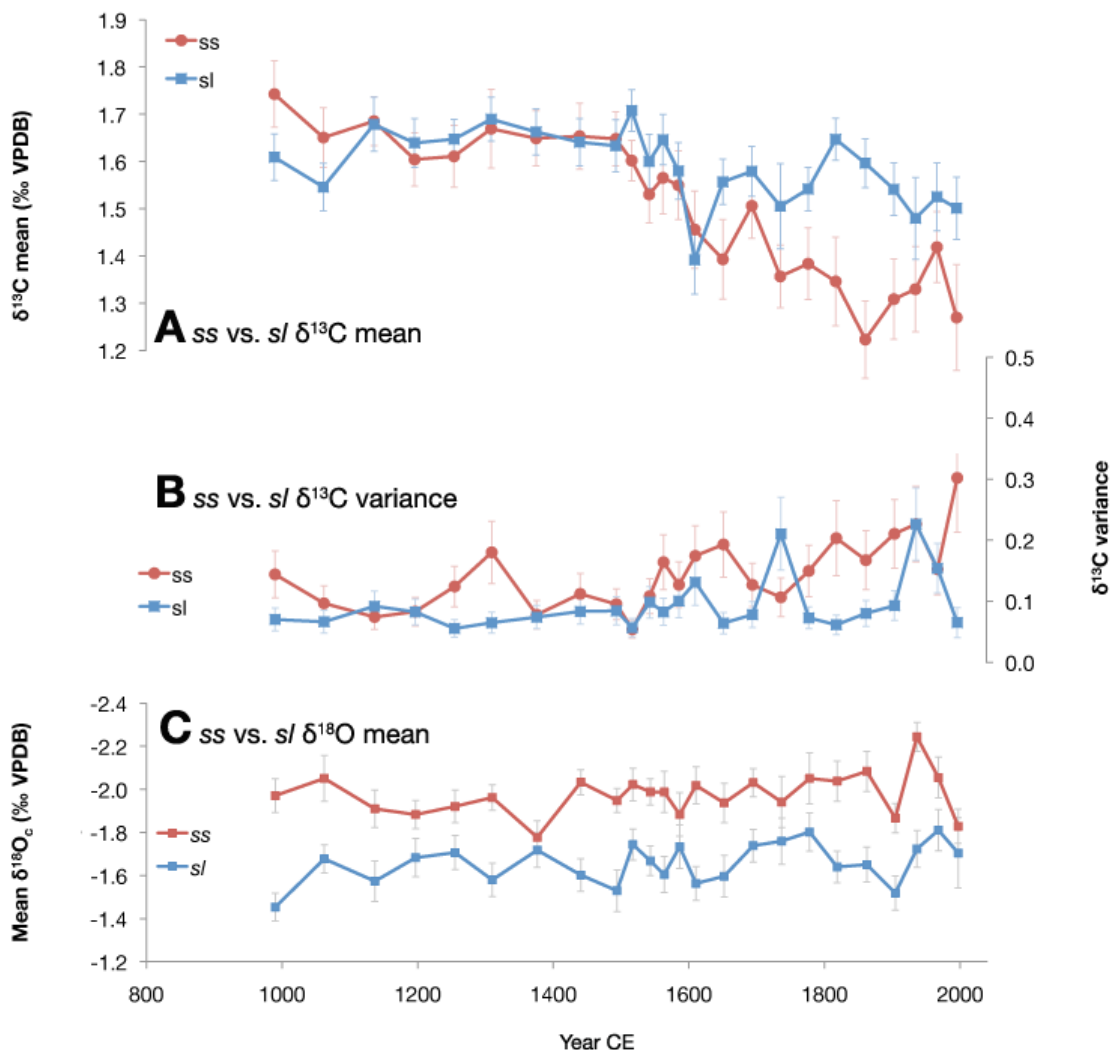


Figure 3.5. *G. ruber* morphotype differences in $\delta^{13}\text{C}$ mean and variance. (A) ss and sl $\delta^{13}\text{C}$ mean. The means for both morphotypes are within error for most pre-1500 CE intervals, but diverge after 1500 CE. sl morphotypes show a small trend (-0.02‰ / century, $p>0.05$) through the LIA and modern. Mean $\delta^{13}\text{C}$ in ss morphotypes decreases at 0.06‰ / century ($p<0.05$) from 1500 CE to present. **(B)** ss and sl morphotype $\delta^{13}\text{C}$ variance. Vertical whiskers show the standard error of the variance. **(C)** ss and sl morphotype mean $\delta^{18}\text{O}$ (Chapter 1). The 0.32‰ difference in mean $\delta^{18}\text{O}$ equates to ~1.5

Chapter 3: $\delta^{13}\text{C}$ Suess effect observed in individual foraminifera from the EEP

°C difference in calcification temperature, or ~10 m of depth (Chapter 4). Error bars represent standard error of the mean.

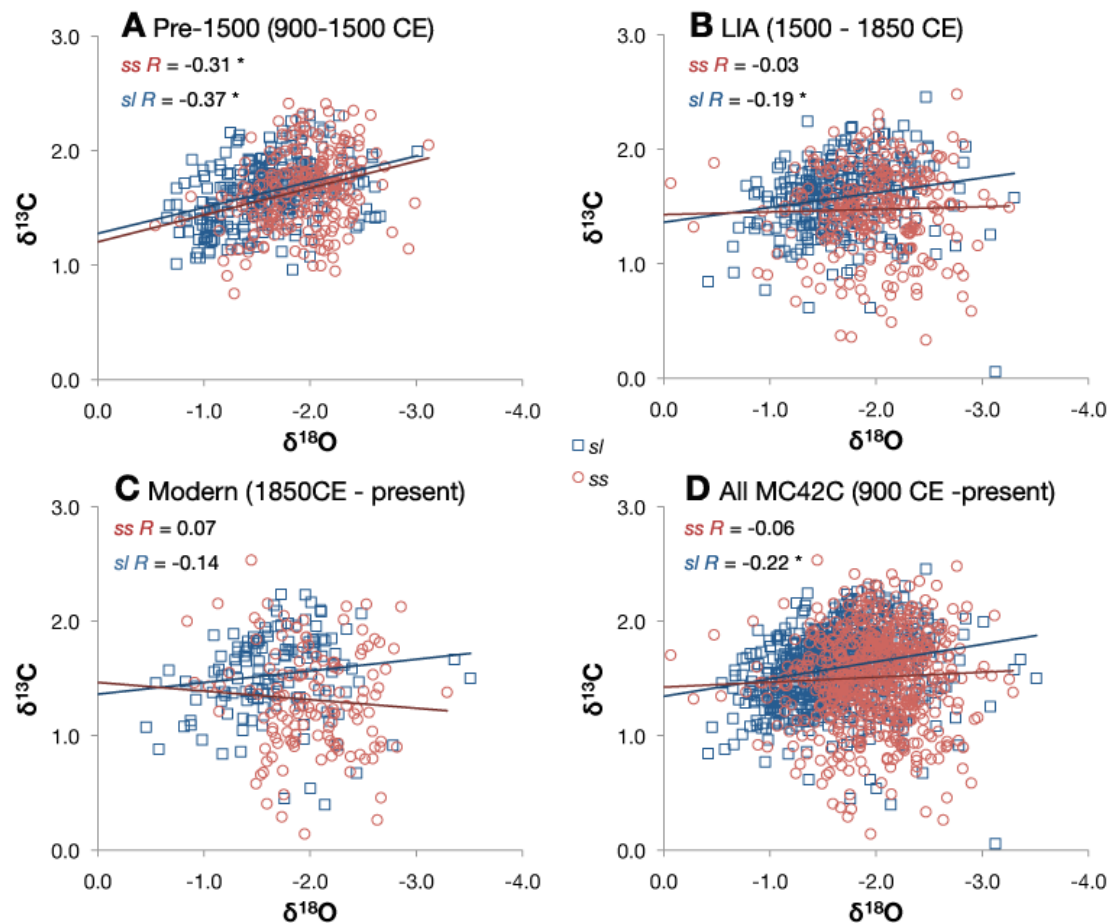


Figure 3.6. *G. ruber* morphotype $\delta^{13}\text{C} - \delta^{18}\text{O}_\text{c}$ relationships. **(A)** Pre-1500 CE, ss and sl morphotypes have a similar $\delta^{13}\text{C}-\delta^{18}\text{O}_\text{c}$ relationship. **(B)** In the LIA (1500-1850 CE), differences between the morphotypes begin to emerge as shown by offset trend lines. R -values for both morphotypes have increased toward zero, and the relationship for ss is no longer significant. **(C)** Modern era (1850 CE – present) $\delta^{13}\text{C}-\delta^{18}\text{O}_\text{c}$ relationship for sl is no longer significant, and ss now have a positive R -value. **(D)** $\delta^{13}\text{C}-\delta^{18}\text{O}$ scatter plot for the full MC42C data from 900 CE to present.

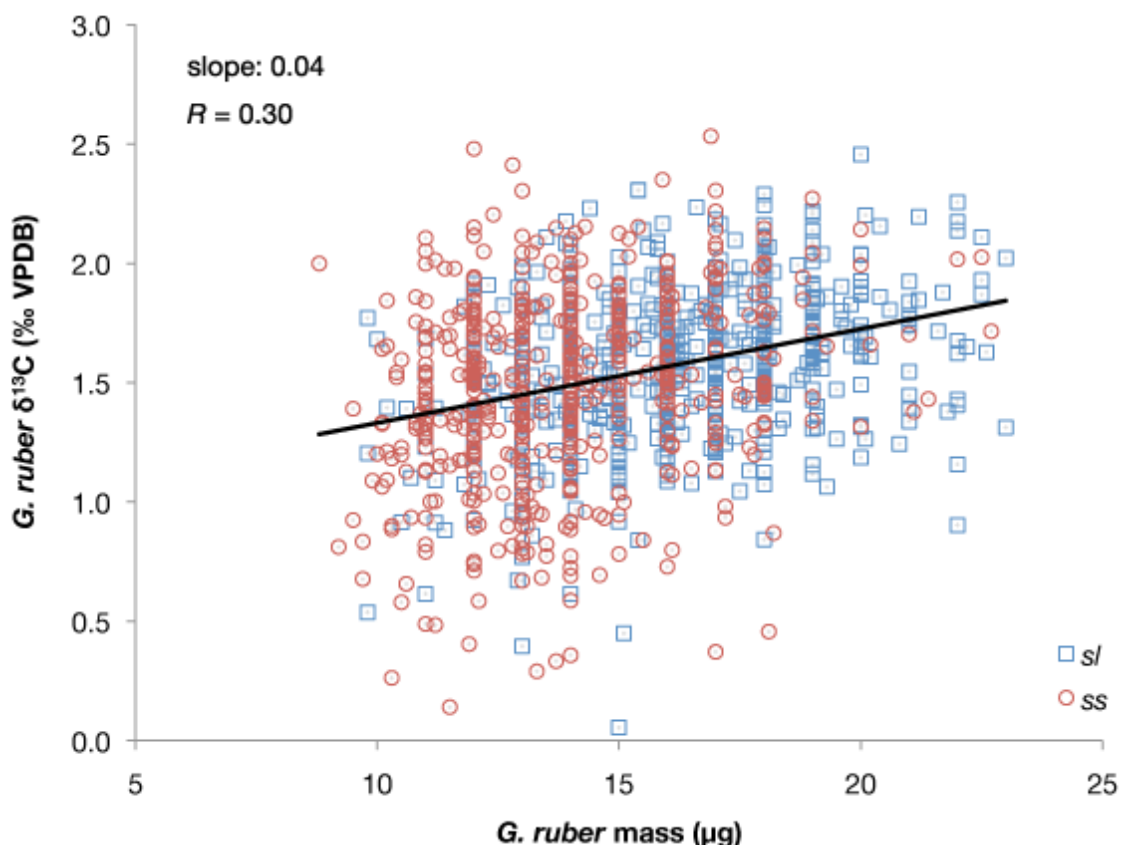


Figure 3.7. *G. ruber* $\delta^{13}\text{C}$ mass effect in the analyzed MC42C samples. *G. ruber* $\delta^{13}\text{C}$ is known to have a strong mass dependency (Berger et al. 1978, Oppo and Fairbanks, 1995, Elderfield et al. 2002) in both *ss* and *sl* morphotypes. All individuals used in this analysis were from the 300-355 μm size-fraction and weighed between 8.8 and 23.0 μg . The slope of the line is 0.04 and the correlation is $R=0.30$ ($p<0.05$).

Tables

Age (Years CE)	N	$\delta^{13}\text{C}$ Mean (‰)	$\delta^{13}\text{C}$ Variance
<i>Modern</i>			
1985-2009	39	1.36 ±0.08	0.22 ±0.05
1951-1985	57	1.48 ±0.05	0.15 ±0.03
1922-1951	58	1.41 ±0.06	0.23 ±0.04
1887-1922	59	1.43 ±0.05	0.16 ±0.03
1838-1887	55	1.43 ±0.05	0.15 ±0.03
<i>LIA</i>			
1800-1838	54	1.52 ±0.05	0.14 ±0.03
1756-1800	60	1.47 ±0.04	0.11 ±0.02
1717-1756	50	1.43 ±0.06	0.16 ±0.03
1672-1717	55	1.54 ±0.04	0.1 ±0.02
1632-1672	55	1.48 ±0.05	0.13 ±0.03
1590-1632	51	1.42 ±0.05	0.15 ±0.03
1572-1590	52	1.57 ±0.05	0.11 ±0.02
1555-1572	57	1.61 ±0.05	0.12 ±0.02
1532-1555	60	1.57 ±0.04	0.1 ±0.02
1503-1532	58	1.65 ±0.03	0.06 ±0.01
<i>Pre-1500</i>			
1469-1503	57	1.64 ±0.04	0.09 ±0.02
1413-1469	56	1.65 ±0.04	0.09 ±0.02
1340-1413	54	1.66 ±0.04	0.07 ±0.01
1280-1340	56	1.68 ±0.05	0.12 ±0.02
1231-1280	60	1.63 ±0.04	0.09 ±0.02
1163-1231	57	1.62 ±0.04	0.08 ±0.02
1103-1163	56	1.68 ±0.04	0.08 ±0.02
1022-1103	50	1.60 ±0.04	0.09 ±0.02
958-1022	59	1.66 ±0.05	0.12 ±0.02

Chapter 3: $\delta^{13}\text{C}$ Suess effect observed in individual foraminifera from the EEP

Table 3.1. $\delta^{13}\text{C}$ mean and variance for each sample interval. Mean shows the standard error for the mean. Variance shows the standard error of the variance.

Period	Mass (all, μg)	Mass (ss, μg)	Mass (sl, μg)	Mean $\delta^{13}\text{C}$	Mean $\delta^{13}\text{C}$ (ss, ‰)	Mean $\delta^{13}\text{C}$ (sl, ‰)
Pre-1500	15.38 ± 7.71	14.00	16.57	1.67 ± 0.30	1.68 ± 0.30	1.66 ± 0.28
LIA	15.37 ± 2.86	14.12	16.52	1.53 ± 0.35	1.47 ± 0.38	1.58 ± 0.31
Modern	14.53 ± 7.56	13.37	15.67	1.42 ± 0.42	1.32 ± 0.46	1.53 ± 0.36

Table 3.2. *G. ruber* masses and mean $\delta^{13}\text{C}$

Chapter 4. Paired $\delta^{18}\text{O}_c$ and Mg/Ca single-shell analysis of *Neogloboquadrina dutertrei* from the eastern equatorial Pacific: assessment of depth habitat and utility as an ENSO proxy

Abstract

Reconstructing past eastern equatorial Pacific (EEP) thermocline conditions can provide vital clues to understanding variability of the El Niño Southern Oscillation (ENSO). Here we analyze $\delta^{18}\text{O}_c$ from single shells of the abundant thermocline-dwelling foraminifer *Neogloboquadrina dutertrei* from EEP core-top sediments to assess this species' ability to capture the full range and variability of thermocline conditions. Depth habitat was inferred by matching *N. dutertrei* $\delta^{18}\text{O}_c$ mean, range and variance with expected $\delta^{18}\text{O}_c$ values calculated from modern temperature and salinity data. Larger *N. dutertrei* had $\delta^{18}\text{O}_c$ signatures consistent with a depth habitat of 58-73 m, while smaller specimens $\delta^{18}\text{O}_c$ suggest a depth habitat of 83-96 m. At these depths, *N. dutertrei* $\delta^{18}\text{O}_c$ appears to capture the full seasonal cycle and coldest La Niña events from the modern record, but the most extreme warm (El Niño) events are not represented in the $\delta^{18}\text{O}_c$ record. Paired analysis of Mg/Ca and $\delta^{18}\text{O}_c$ from the same shells shows no correlation. These differences suggest each analytical method may be sensitive to conditions experienced through ontogeny, and the sensitivity to temperature may differ in each method.

Introduction

Neogloboquadrina dutertrei is the most abundant foraminifera species in eastern equatorial Pacific (EEP) sediments. This species is commonly thought to live in the thermocline (Fairbanks et al. 1982) at the deep chlorophyll maximum (Fairbanks and Wiebe, 1980). In the EEP, the El Niño Southern Oscillation (ENSO) has profound effects on the thermocline, which can experience temperature changes greater in magnitude than those experienced at the surface (Wang and Fiedler 2006, Carton and Giese 2008). The large size of individuals and their abundance make this species a favorable candidate for single-shell analysis to reconstruct past ENSO conditions (Chapter 1). However, the use of this species as an ENSO indicator has met with mixed success (Leduc et al. 2009; Ford et al. 2015), highlighting the need for better understanding of thermocline species as ENSO proxies.

Here we present $\delta^{18}\text{O}_c$ and Mg/Ca from individual *N. dutertrei* from modern core-top sediments from the eastern equatorial Pacific cold tongue region. In this study we will characterize the mean and variance of two size fractions (355-425 μm and 425+ μm) to estimate calcification depth and to assess the ability of *N. dutertrei* individuals to capture the full range of modern oceanic conditions in the EEP. We also assess the correlation between Mg/Ca ratios and $\delta^{18}\text{O}_c$ temperature in the same shells (Anand et al. 2003, Steinhardt et al. 2015). The ability of *N. dutertrei* to accurately capture thermocline variability is important for multi-species approaches to observe water mass variability (Rosenthal et al. 2013), and an enhanced understanding of thermocline variability may

*Chapter 4: Paired $\delta^{18}\text{O}_c$ and Mg/Ca single-shell analysis of *N. dutertrei* from the EEP*
provide additional clues to characterizing surface variability in response to ENSO,
enhanced seasonality, or both (Ford et al. 2015).

Materials and Methods

Individual specimens of the kummerform foraminifera *N. dutertrei* were isolated from the 355-425 μm and $>425 \mu\text{m}$ size fractions of the core-top sediments (0-0.5cm) from multi-core KNR195-5 MC38G. This core was raised on 4/4/2009 from near the Galapagos Islands ($1^\circ 15.94\text{S } 89^\circ 41.96\text{W}$, 597m) within the eastern equatorial Pacific cold tongue. Selected *N. dutertrei* individuals from the 355-425 μm size fraction were subject to laser ablation ICP-MS Mg/Ca analysis by A. Sadekov at the University of Cambridge, UK, per procedures in Sadekov et al. (2005). Samples were then returned for further analysis. Mg/Ca values were converted to temperature using the multi-species calibration (Anand et al. 2003):

$$\text{Mg/Ca} = 0.38 \exp(0.090T) \quad (\text{Equation 1})$$

$\delta^{18}\text{O}_c$ and $\delta^{13}\text{C}$ were measured using a Thermo Delta V with a Kiel IV carbonate preparation device at the Lamont-Doherty Earth Observatory. Analytical precision of $\delta^{18}\text{O}_c$ was 0.07‰ for the 355-425 μm size fraction (hereafter 355 μm) and was 0.09‰ for the $>425 \mu\text{m}$ size fraction (hereafter 425 μm). $\delta^{13}\text{C}$ analytical precision was 0.03‰ for the 355 μm size fraction and 0.02‰ for the 425 μm size fraction. Precision was maintained by repeated measurements of NBS-19.

*Chapter 4: Paired $\delta^{18}\text{O}_c$ and Mg/Ca single-shell analysis of *N. dutertrei* from the EEP*

Monthly temperature and salinity data for the $0.5^\circ \times 0.5^\circ$ grid box surrounding the study site from 1958-2008 was obtained from *Simple Ocean Data Assimilation* data v2.1.6 (SODA 2.1.6, Carton and Giese 2008). Monthly $\delta^{18}\text{O}_c$ values were calculated from temperature and salinity values using the following equations relating $\delta^{18}\text{O}_c$ to temperature and the $\delta^{18}\text{O}$ of seawater (Bemis et al. 1998):

$$T(\text{°C}) = 16.5(\pm 0.2) - 4.80(\pm 0.16) * (\delta^{18}\text{O}_c - \delta^{18}\text{O}_{\text{sw}}) \quad [\text{low-light}] \quad (\text{Equation 2})$$

$$T(\text{°C}) = 14.9(\pm 0.1) - 4.80(\pm 0.08) * (\delta^{18}\text{O}_c - \delta^{18}\text{O}_{\text{sw}}) \quad [\text{high-light}] \quad (\text{Equation 3})$$

$\delta^{18}\text{O}_{\text{sw}}$ was calculated from the salinity relationship calculated from the Panama Basin (Fairbanks et al. 1982):

$$\delta^{18}\text{O}_{\text{sw}} = 0.260(S) - 8.773 \quad (\text{Equation 4})$$

The mean, seasonal maximum, and seasonal minimum, absolute maximum and minimum $\delta^{18}\text{O}_c$ were calculated from SODA 2.1.6 monthly temperature and salinity data for depths from 5 m to 500 m to create vertical $\delta^{18}\text{O}_c$ profiles for the mean annual temperature and salinity, seasonal cycle, and the entire range of $\delta^{18}\text{O}_c$ for the time period 1958-2008. The high-light equation (Equation 2) was used to calculate the expected $\delta^{18}\text{O}_c$ at depths above 50 m. The low-light equation (Equation 3) was used below 50 m. On Figure 4.2, the transition between high-light and low-light zones is shown with stippled lines. The low-light equation has been used in previous core-top studies of *N. dutertrei* (Cléroux et al. 2013), and calcification temperature calculated using this equation in this study are consistent with the depth habitat in the deep thermocline suggested by $\delta^{18}\text{O}_c$ (Cléroux et al. 2013), Mg/Ca and $\delta^{18}\text{O}_c$ (Steinhardt et al. 2015) and from plankton tows (Fairbanks et al. 1982). The calibration of Kim and O'Neil (1997) for the precipitation of non-biogenic

*Chapter 4: Paired $\delta^{18}\text{O}_c$ and Mg/Ca single-shell analysis of *N. dutertrei* from the EEP*
carbonate has been used for previous *N. dutertrei* studies (Cléroux et al. 2013, Steinhardt et al. 2015). Mean $\delta^{18}\text{O}_c$ values calculated from SODA 2.1.6 data using this calibration were within 0.1‰ of low-light $\delta^{18}\text{O}_c$ values for the upper 200 m of the water column.

Results

$\delta^{18}\text{O}_c$ and $\delta^{13}\text{C}$ data from the individual *N. dutertrei* from MC38G are shown in Table 4.1. Individuals from 425 µm population are on average more isotopically depleted than those from the 355 µm size-fraction. The range of each size-fraction is similar at 1.05‰ for 425 µm and 0.95‰ for 355 µm. The frequency distribution of the 425 µm size fraction is shifted toward more depleted $\delta^{18}\text{O}_c$ values, suggesting warmer calcification conditions, but is overall similar to the distribution for the 355 µm fraction (Figure 4.1). Mean $\delta^{18}\text{O}_c$ for 425 µm is -0.04 ± 0.06 , consistent with annual mean $\delta^{18}\text{O}_c$ at depths of 58-70 m per calculated SODA 2.1.6 $\delta^{18}\text{O}_c$ (Figure 4.2). $\delta^{18}\text{O}_c$ variance for this size fraction is 0.09 ± 0.03 , less than that calculated for either 58 m (0.18) or 70 m (0.14), similar to the calculated variance at 83 m (0.10). The smaller 355 µm size fraction have a mean $\delta^{18}\text{O}_c$ of 0.19‰, consistent with the annual mean $\delta^{18}\text{O}_c$ at 83-96 m depth, indicating a deeper habitat for this size fraction (Figure 4.2). $\delta^{18}\text{O}_c$ variance for this size-fraction is 0.04 ± 0.01 , in-line with the variance of calculated $\delta^{18}\text{O}_c$ at 112 m depth rather than the depth habitats suggested by mean $\delta^{18}\text{O}_c$. Both size fractions appear to capture the full range of the seasonal cycle at the depths suggested by their respective mean $\delta^{18}\text{O}_c$ values. Both size fraction capture the most isotopically enriched $\delta^{18}\text{O}_c$ values representing cooler conditions, but the warmest, most isotopically depleted $\delta^{18}\text{O}_c$ values are not represented by the *N. dutertrei* $\delta^{18}\text{O}_c$ for either size fraction.

An analysis of this $\delta^{18}\text{O}_c$ range limit for *N. dutertrei* shows that the calculated $\delta^{18}\text{O}_c$ values that are beyond the most depleted (most negative and warmest) *N. dutertrei* $\delta^{18}\text{O}_c$ values are predominantly from strong El Niño events, notably from the extremely strong El Niño events of 1997-98 and 1982-1983. This finding has implications for the use of this species as a stand-alone ENSO proxy, as paleo-proxy records may be under-representing the frequency of such extreme El Niño events. However, the small sample size and limited number of analyses prohibits a definitive evaluation of *N. dutertrei* as an ENSO proxy, but rather points to potential caveats for future investigators.

The approach of using the $\delta^{18}\text{O}_c$ mean, range and variance from individual foraminifera to characterize the species depth habitat was applied to individuals of the surface-dwelling foraminifer *Globigerinoides ruber* from nearby multi-core MC42C (Chapter 1, Chapter 3). Based on sub-population mean $\delta^{18}\text{O}_c$, *sensu stricto* morphotypes (*ss*) inhabit a shallower depth habitat than *sensu latu* (*sl*) morphotypes (Figure 4.2), consistent with previous studies (Wang, 2000, Löwenmark et al. 2005) and consistent with $\delta^{13}\text{C}$ data suggesting shallower/warmer conditions (Chapter 3). The range of the *ss* morphotype captures the seasonal cycle and cooler events well, but does not extend through the warmest temperatures, while the *sl* morphotypes capture the entire expected $\delta^{18}\text{O}_c$ range, including the warmest events. This finding indicates a subtle difference in depth or possibly seasonal habitat, and demonstrates that mixed-morphotype *G. ruber* populations closely reflect conditions of the upper-most ocean layer.

Carbon isotopes

The stable carbon isotopes ($\delta^{13}\text{C}$) of *N. dutertrei* were measured in concert with $\delta^{18}\text{O}_c$. We find that the average $\delta^{13}\text{C}$ are statistically equivalent between 355 μm ($1.15\text{\textperthousand} \pm 0.04$) and 425 μm ($1.17\text{\textperthousand} \pm 0.06$). The mean $\delta^{13}\text{C}$ is between 0.2-0.3‰ lower than late Holocene $\delta^{13}\text{C}$ from *N. dutertrei* from the Panama Basin (Pena et al. 2008), which may be evidence for a $\delta^{13}\text{C}$ -Suess effect (Keeling 1979). If this is the case it provides evidence that the $\delta^{13}\text{C}$ signal either penetrates into the EEP thermocline, or that upwelling waters are capable of transmitting the atmospheric $\delta^{13}\text{C}$ signal, contrary to what is observed in *G. ruber* (Chapter 3). No significant relationship between $\delta^{13}\text{C}$ and $\delta^{18}\text{O}_c$ is seen for either size fraction (Figure 4.3). Comparison of $\delta^{13}\text{C}$ and $\delta^{18}\text{O}_c$ in *N. dutertrei* from the Last Glacial Maximum (LGM) also show a lack of significant correlation (Clark 2015), but without individual $\delta^{13}\text{C}$ - $\delta^{18}\text{O}_c$ data from additional time periods, the reason for this lack of relationship remains elusive. Clearly more investigation into the source of $\delta^{13}\text{C}$ modulations is necessary.

Mass effects on $\delta^{13}\text{C}$ and $\delta^{18}\text{O}_c$ in *N. dutertrei*

$\delta^{13}\text{C}$ is known to be sensitive to mass in foraminifera (Oppo and Fairbanks, 1989), and $\delta^{18}\text{O}_c$ may also be influenced by sample mass in *N. dutertrei* (Leduc et al. 2009). The mass dependency of $\delta^{13}\text{C}$ is thought to be related to growth rate, and is thus reduced in the largest, slowest growing size fraction (Ravelo and Hillaire-Marcel, 2007). Here we find the opposite, as the 425 μm size-fraction shows a significant linear relationship

*Chapter 4: Paired $\delta^{18}\text{O}_c$ and Mg/Ca single-shell analysis of *N. dutertrei* from the EEP*
between mass and $\delta^{13}\text{C}$ ($p < 0.05$) and slight, but not significant relationship between $\delta^{18}\text{O}_c$
and individual foraminifera mass ($p < 0.09$) (Figure 4.4). We do not observe a significant
linear relationship between mass and $\delta^{13}\text{C}$ or $\delta^{18}\text{O}_c$ in the 355 μm *N. dutertrei*.

Mg/Ca

LAICMP-MS Mg/Ca data is known to be highly sensitive to growth bands, chamber selection, and ontogenetic calcite crusts on test walls (Eggins et al. 2003, Sadekov et al. 2005, A. Sadekov, *pers. comm 2014*). To reduce bias in the measurements multiple chambers were targeted for analysis. Foraminifera chambers are labeled f, f1, f2, f3, etc., in descending order of calcification, with the f chamber representing the last, most recently calcified chamber (Eggins et al. 2003). Here, the results from Mg/Ca analyses were averaged across three chambers (f2+f3+f4) and for all measured chambers (f, f1+f2+f3+f4) (Sadekov et al. 2005) for each measured specimen of *N. dutertrei* in the 355 μm size. The f2+f3+f4 Mg/Ca temperature values are consistently lower than the all-chamber values, and the f2+f3+f4 mean temperature (12.3 °C) implies a depth habitat in excess of 250 m, inconsistent with plankton tow depth habitat (Fairbanks et al. 1982) and previous studies (Cléroux et al. 2013, Steinhardt et al. 2015). The all-chambers mean temperature of 15.9 °C is consistent with a depth habitat of ~90 m, consistent with depth inferred from mean $\delta^{18}\text{O}_c$. The mean calcification temperature of all individuals analyzed for both Mg/Ca and $\delta^{18}\text{O}_c$ is 15.68 ± 0.39 (based on Mg/Ca) and 17.26 ± 0.16 (for $\delta^{18}\text{O}_c$). Mg/Ca mean temperature is in comparable to Mg/Ca temperature of 13.7 °C found in Panama Basin *N. dutertrei* (Pena et al. 2008), and higher Mg/Ca temperature of

*Chapter 4: Paired $\delta^{18}\text{O}_c$ and Mg/Ca single-shell analysis of *N. dutertrei* from the EEP*
17.7 °C from equatorial Atlantic Ocean core-top *N. dutertrei* (Cléroux et al. 2013). The Mg/Ca temperature variance from the individual *N. dutertrei* (7.30) is over four times the SODA 2.1.6 temperature variance at 97 m, and nearly three times the variance at 83 m. The Mg/Ca temperatures exceed the seasonal temperature range for both 83 m and 97 m. The minimum Mg/Ca temperature for all-chambers (10.2 °C) is lower than the minimum temperature in the upper 250 m of the SODA data. This broad range may be due to the effects of banding, calcitic crusts or other micro-scale inhomogeneity in the tests (Eggins et al. 2003, Sadekov et al. 2005) that are not factors in whole-shell analysis for $\delta^{18}\text{O}_c$.

Both Mg/Ca ratios and $\delta^{18}\text{O}_c$ are considered to be largely reflective of calcification temperature, so here we test the correlation of paired values measured on the same shells from the 355 µm size fraction. Single shell $\delta^{18}\text{O}_c$ is not correlated with paired (3-chamber or all-chamber) Mg/Ca values (Figure 4.5). Similar results are obtained with converting Mg/Ca to temperature, and by converting $\delta^{18}\text{O}_c$ values to temperature using depth-appropriate salinity values. We do note a difference between the three-chamber and all-chamber temperature relationship with $\delta^{18}\text{O}_c$, indicating measurable differences between shell chambers. If the calcite of these chambers is reflective of specific conditions at specific moments in the foraminifer's life history, this is evidence for changing conditions during ontogeny (Steinhardt et al. 2015).

Discussion

Plankton tows in the Panama Basin found *N. dutertrei* living from the surface to depths beyond 500 m, with population density maxima between 50 m and 100 m (Fairbanks et

*Chapter 4: Paired $\delta^{18}\text{O}_c$ and Mg/Ca single-shell analysis of *N. dutertrei* from the EEP*
al. 1982). The species has been characterized as a deep thermocline species (Leduc et al. 2009, Cléroux et al. 2013) inhabiting a deep chlorophyll maximum zone (Fairbanks and Wiebe, 1980). Assumed *N. dutertrei* depths, for the purposes of calibration and temperature calculation, range from 50 m (Leduc et al. 2009) to 100 m (Loubere 2001), based on earlier plankton tow data (Fairbanks et al. 1982). Cleroux et al. (2013) found that the calcification depth is in the range of 90–135 m based on multiple calibration parameters, and Steinhardt et al. (2015) used combined Mg/Ca– $\delta^{18}\text{O}_c$ to infer a mean calcification depth of 37 m or 81 m, depending on eddy conditions. Using a simple $\delta^{18}\text{O}_c$ mean-and-variance approach from the individual foraminifera, we find that the larger 425 μm specimens have a depth habitat consistent with 58–70 m, and the 355 μm size fraction is consistent with 83–97 m. The mean 355 μm Mg/Ca temperature of 15.9 °C is also in the 83–97 m range. These depths are slightly shallower than the depth habitat inferred by Cléroux et al. (2013) for Atlantic *N. dutertrei*, but is within the calcification range reported from *N. dutertrei* from the Mozambique Channel (Steinhardt et al. 2015) suggesting that the calcification depths calculated here are reasonable estimates.

Attempts to infer changes in ENSO through analysis of individual thermocline-dwelling - dwelling foraminifera species *Pulleniatina obliquiloculata* (Khider et al. 2011), and *Neogloboquadrina dutertrei* (Leduc et al. 2009) have had mixed success. The $\delta^{18}\text{O}_c$ variance measured in thermocline species can be small (Khider et al. 2011), and systematic changes difficult to discern (Leduc et al. 2009). In the EEP, *N. dutertrei* $\delta^{18}\text{O}_c$ did not show changes in the amplitude or frequency of ENSO events over the last glacial

*Chapter 4: Paired $\delta^{18}\text{O}_c$ and Mg/Ca single-shell analysis of *N. dutertrei* from the EEP*

period, despite evidence for changes in the total variance through time (Leduc et al. 2009). We find that individual *N. dutertrei* $\delta^{18}\text{O}_c$ do not capture the full range of warm conditions encountered at the presumed depth habitats, which provides insight into the lack of evidence for changes in ENSO amplitude and frequency. If extreme warm events are not recorded, inferences of ENSO activity will be biased toward lower variance. At 83 m (the shallow end of the 355 μm depth habitat), temperature anomalies of up to 7 °C are observed during the strongest El Niño events (SODA 2.1.6). It is possible that these anomalously warm temperatures reduce *N. dutertrei* productivity, resulting in fewer $\delta^{18}\text{O}$ -depleted specimens. However *N. dutertrei* from the Atlantic basin record mean $\delta^{18}\text{O}_c$ values near the minimum calculated thermocline $\delta^{18}\text{O}_c$ values, suggesting that it is biologically possible for the species to grow under warmer conditions (Cléroux et al. 2013). It is also possible that the lack of the warmest events may be due to undersampling in modern sediments, particularly in the 425 μm size fraction (N=25). It should be noted that wide range of individual Mg/Ca temperatures includes a value consistent with the warmest temperature at 83 m (23.38 °C vs. 23.95 °C), suggesting that it may be possible for calcification to occur at the most elevated EEP thermocline temperatures.

The difference in mean $\delta^{18}\text{O}_c$ from the 355 μm and 425 μm size fractions, difference in Mg/Ca between shell chambers, and the lack of correlation between Mg/Ca and $\delta^{18}\text{O}_c$ is consistent with previous findings of variable depths during *N. dutertrei* ontogeny (Steinhardt et al. 2015). $\delta^{18}\text{O}_c$ is constantly added during the life of the foraminifer (Bé and Lott, 1964), and whole-shell $\delta^{18}\text{O}_c$ integrates all conditions experienced, an assertion

*Chapter 4: Paired $\delta^{18}\text{O}_c$ and Mg/Ca single-shell analysis of *N. dutertrei* from the EEP* supported by a cumulative $\delta^{13}\text{C}$ – $\delta^{18}\text{O}_c$ mass balance model (Steinhardt et al. 2015). As the larger chambers are added later in development (Olsson 1973), integrated $\delta^{18}\text{O}_c$ is weighted towards the final conditions, but conditions from early in ontogeny exert influence on final $\delta^{18}\text{O}_c$ (Steinhardt et al. 2015). Differences between 3-chamber and all-chamber Mg/Ca measurements reinforces this notion of changing depth habitat and conditions over the foraminifera life-cycle (Eggins et al. 2003, Steinhardt et al. 2015). Measurements from individual chambers may represent short periods of calcification in specific environments, and thus measurements from more chambers integrate conditions from longer time intervals and more diverse environments (Sadekov et al. 2005). The three different measurements – three-chamber Mg/Ca, all-chamber Mg/Ca and full-specimen $\delta^{18}\text{O}$ – may be integrating progressively longer records of the conditions experienced by an individual foraminifer. This may explain some of the difference in estimated calcification temperatures from the same individual. The influence of salinity (e.g. Bemis et al. 1998), mass dependence (Leduc et al. 2009) and calibration (Anand et al. 2003) on estimated $\delta^{18}\text{O}_c$ and Mg/Ca derived temperatures may also be a factor in the differences.

Conclusions

We conducted paired Mg/Ca and $\delta^{18}\text{O}_c$ analysis on individuals of *N. dutertrei* from the 355–425 μm size fraction and $\delta^{18}\text{O}_c$ analysis on individuals from the >425 μm size fraction. We find that paired same-shell measurements show no correlation between Mg/Ca and $\delta^{18}\text{O}_c$, suggesting that either one of these proxies (or both) does not primarily

*Chapter 4: Paired $\delta^{18}\text{O}_c$ and Mg/Ca single-shell analysis of *N. dutertrei* from the EEP*

reflect calcification temperature. Further study of whole-shell vs. individual chamber Mg/Ca, and whole-shell Mg/Ca vs. whole-shell $\delta^{18}\text{O}_c$ is warranted to determine the relationship with calcification temperature. We have also constrained the depth habitat of *N. dutertrei* to the deep thermocline in the EEP, and observed that measured $\delta^{18}\text{O}_c$ captures the seasonal cycle and the coldest conditions, but not the most extreme warm conditions, questioning this species' usefulness for ENSO studies. These results indicate further calibrations experiments are needed to assess the utility of this species as a thermocline paleoceanographic proxy.

Figures

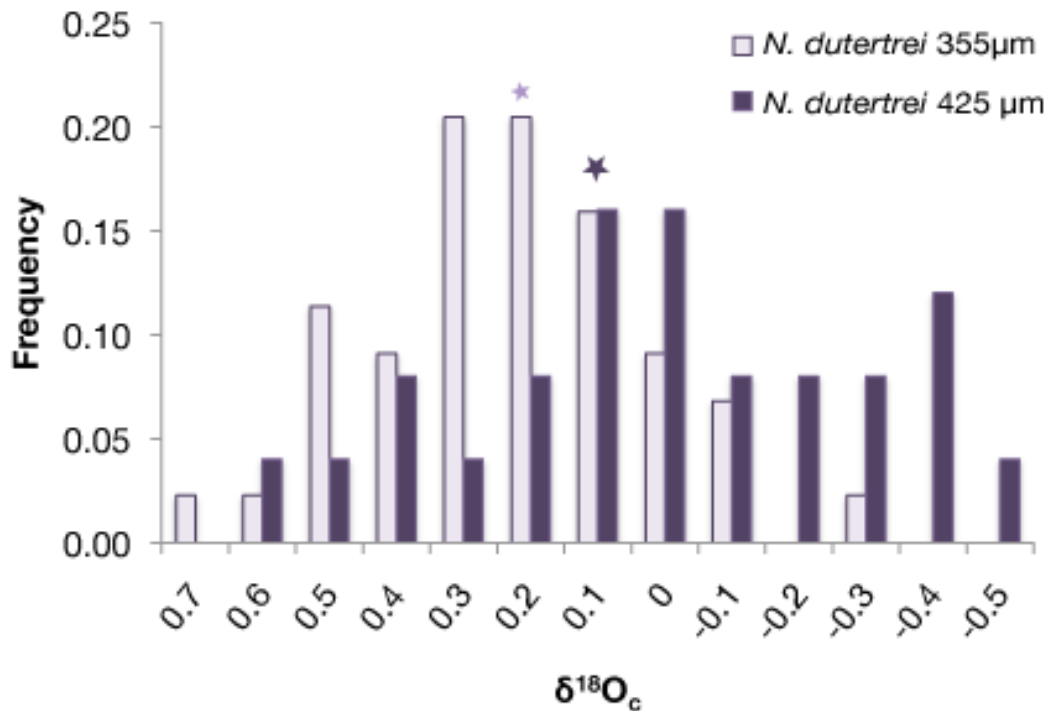


Figure 4.1. Frequency histogram of individual *N. dutertrei* $\delta^{18}\text{O}_c$ from two size fractions. Light purple is 355 μm . Population mean for this size fraction is $0.19\text{\textperthousand} \pm 0.3$, variance = 0.04 ± 0.01 , N=44. Dark purple is 425 μm size fraction. Population mean is - $0.04\text{\textperthousand} \pm 0.06$, variance is 0.09 ± 0.03 , N=25. Stars represent the population mean. The larger population (425 μm , dark purple) is shifted to the right, representing more depleted $\delta^{18}\text{O}_c$ and warmer temperatures.

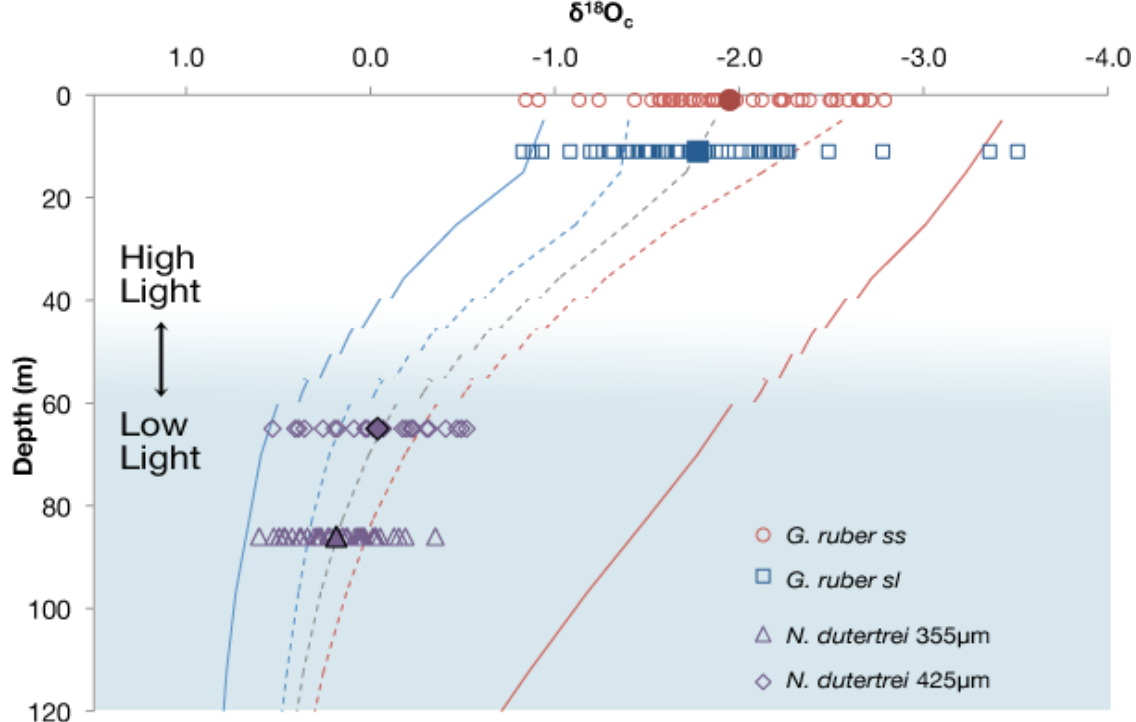


Figure 4.2. Depth habitat for *G. ruber* and *N. dutertrei*. SODA 2.1.6 temperature and salinity data was used to calculate equilibrium $\delta^{18}\text{O}_c$ for 5-120 m depths. Depths above 50 m use equation 2 for high-light conditions while below 50 m the low-light equation (Equation 3) from Bemis et al. (1998) is used (Cléroux et al. 2013). Dotted gray line is the mean $\delta^{18}\text{O}_c$ from 1958-2008. Dotted red and blue lines are the seasonal maximum and minimum. Solid red and blue lines are the absolute maximum and minimum from the record. Stippled lines from 40-60 m represent a switch from the high-light to low-light $\delta^{18}\text{O}_c$ equations. Depth habitat is estimated from a best fit with $\delta^{18}\text{O}_c$ mean and adjusted slightly to fit both the seasonal and extra-seasonal range.

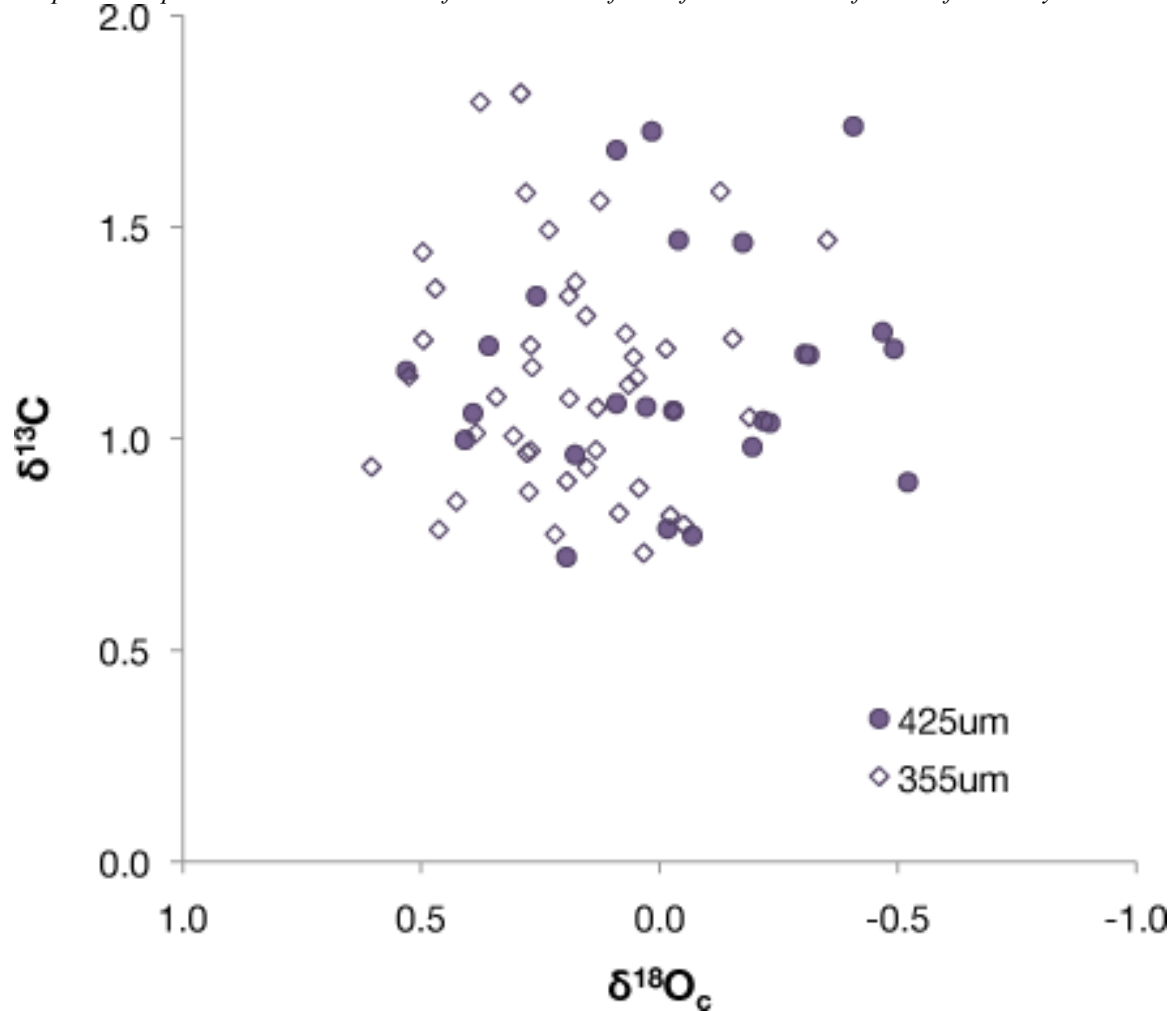


Figure 4.3. $\delta^{13}\text{C}$ - $\delta^{18}\text{O}_c$ for *N. dutertrei* for 355 μm and 425 μm size fractions. No statistically significant relationship is observed between $\delta^{13}\text{C}$ and $\delta^{18}\text{O}_c$ in *N. dutertrei* from MC38G.

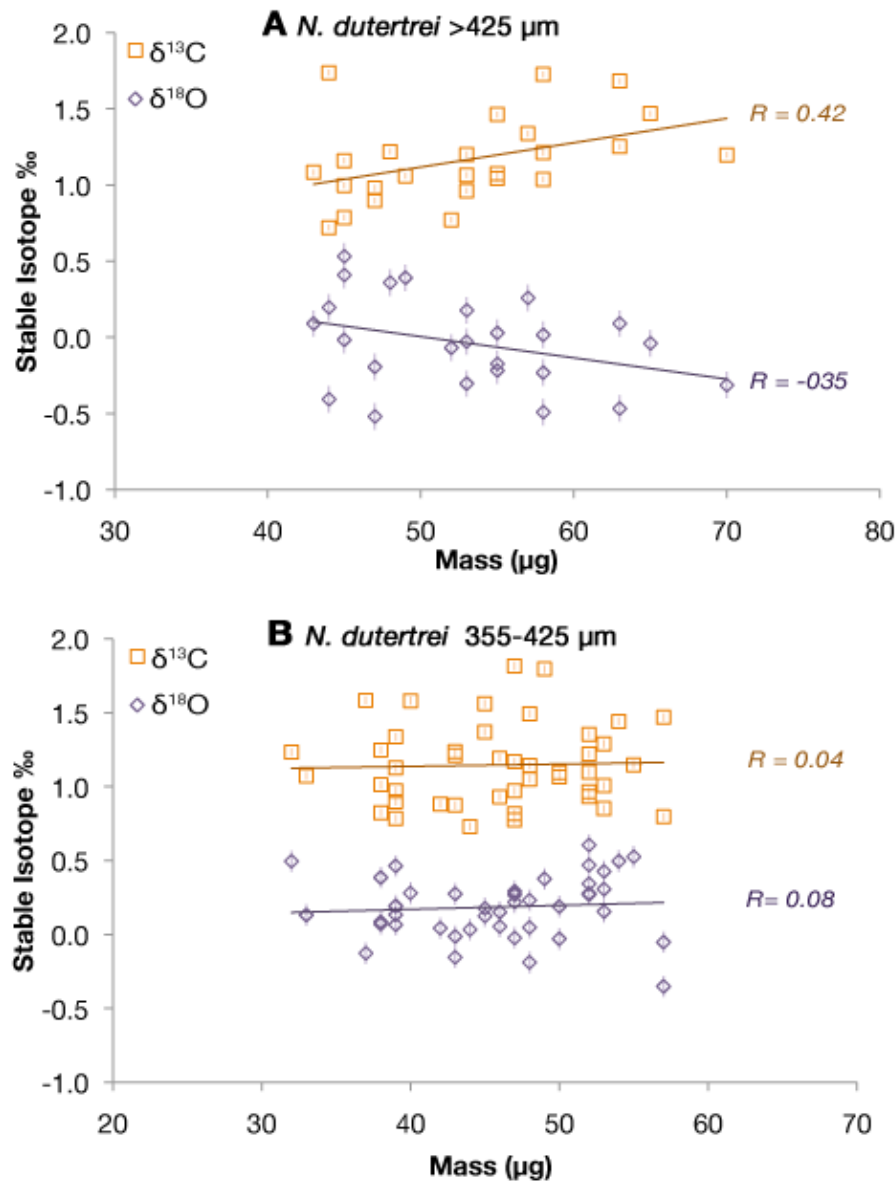


Figure 4.4. Relationship of $\delta^{13}\text{C}$ and $\delta^{18}\text{O}_\text{c}$ to mass in *N. dutertrei* of two size

fractions. (A) 425 µm *N. dutertrei* show a significant correlation between size and $\delta^{13}\text{C}$ ($p<0.05$) and are significant at $p<0.1$ for $\delta^{18}\text{O}_\text{c}$. The smaller size fraction (B) shows no size-dependency for $\delta^{13}\text{C}$ or $\delta^{18}\text{O}_\text{c}$. Horizontal bars for all data points represent the analytical error.

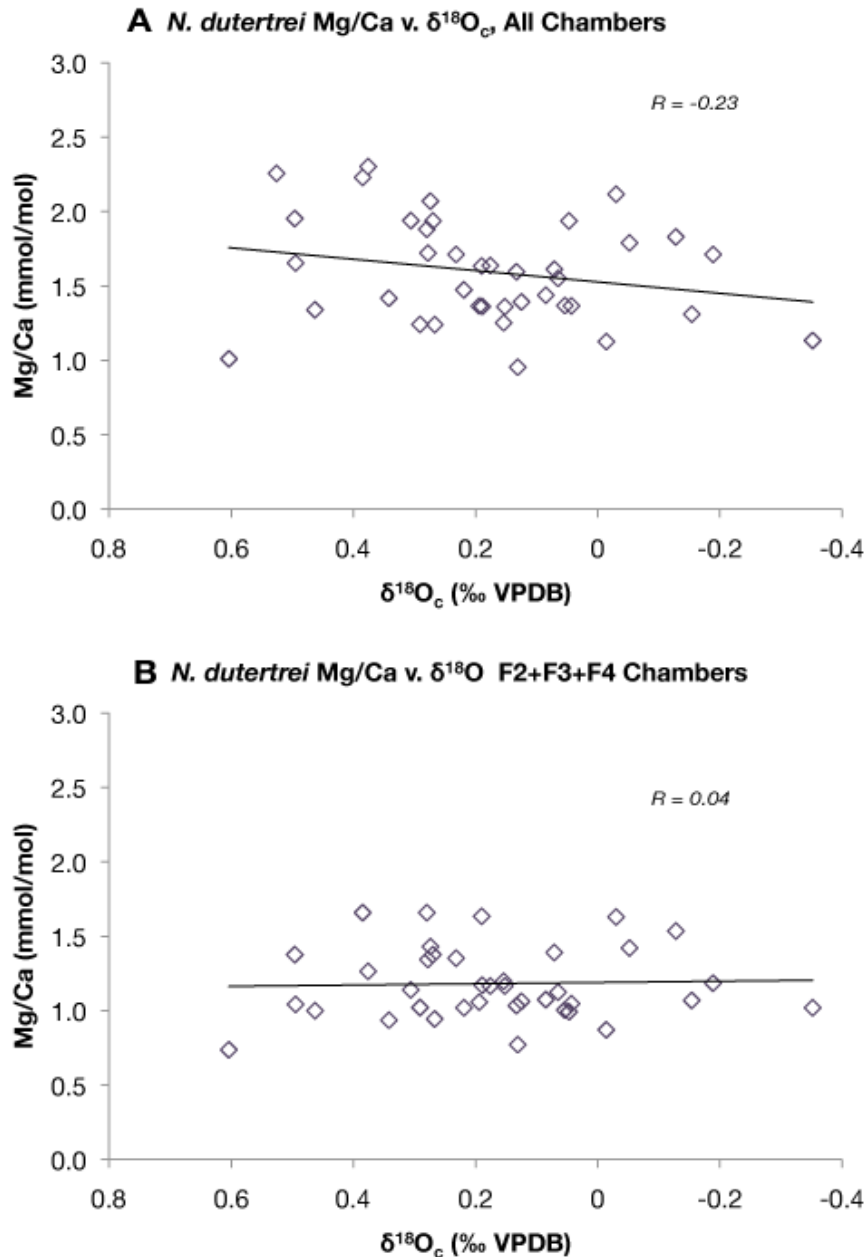


Figure 4.5. Mg/Ca and $\delta^{18}\text{O}_c$ from same-shell analysis. (A) Mg/Ca measured from all chambers ($f+f1+f2+f3+f4$) for each specimen. $\delta^{18}\text{O}_c$ values are for the entire specimen. (B) Mg/Ca values based on analysis of chambers $f2+f3+f4$. Trend lines for both are exponential (Anand et al. 2003). For (A) and (B) $p > 0.05$.

Tables

ID	Mass (μg)	$\delta^{13}\text{C}$ (‰ VPDB)	$\delta^{18}\text{O}_c$ (‰ VPDB)
<i>355-425 μm size-fraction</i>			
MC38 ND355-01	37	1.58 ±0.03	-0.13 ±0.07
MC38 ND355-02	47	1.82 ±0.03	0.29 ±0.07
MC38 ND355-03	39	0.9 ±0.03	0.19 ±0.07
MC38 ND355-05	53	1.29 ±0.03	0.15 ±0.07
MC38 ND355-06	33	1.07 ±0.03	0.13 ±0.07
MC38 ND355-07	47	0.82 ±0.03	-0.02 ±0.07
MC38 ND355-08	46	0.93 ±0.03	0.15 ±0.07
MC38 ND355-09	38	0.82 ±0.03	0.09 ±0.07
MC38 ND355-10	46	1.19 ±0.03	0.05 ±0.07
MC38 ND355-12	57	0.8 ±0.03	-0.05 ±0.07
MC38 ND355-13	38	1.25 ±0.03	0.07 ±0.07
MC38 ND355-14	47	0.77 ±0.03	0.22 ±0.07
MC38 ND355-16	52	0.97 ±0.03	0.28 ±0.07
MC38 ND355-17	53	0.85 ±0.03	0.43 ±0.07
MC38 ND355-18	55	1.15 ±0.03	0.53 ±0.07
MC38 ND355-19	52	1.22 ±0.03	0.27 ±0.07
MC38 ND355-20	44	0.73 ±0.03	0.03 ±0.07
MC38 ND355-21	48	1.14 ±0.03	0.05 ±0.07
MC38 ND355-22	52	0.93 ±0.03	0.6 ±0.07
MC38 ND355-23	47	0.97 ±0.03	0.27 ±0.07
MC38 ND355-24	57	1.47 ±0.03	-0.35 ±0.07

*Chapter 4: Depth habitat and variance of *N. dutertrei* inferred from individual foraminifera analysis*

MC38 ND355-25	47	1.17 ±0.03	0.27 ±0.07
MC38 ND355-26	52	1.1 ±0.03	0.34 ±0.07
MC38 ND355-27	49	1.8 ±0.03	0.38 ±0.07
MC38 ND355-28	48	1.05 ±0.03	-0.19 ±0.07
MC38 ND355-29	45	1.37 ±0.03	0.18 ±0.07
MC38 ND355-31	45	1.56 ±0.03	0.13 ±0.07
MC38 ND355-32	39	0.97 ±0.03	0.13 ±0.07
MC38 ND355-33	50	1.07 ±0.03	-0.03 ±0.07
MC38 ND355-34	39	1.13 ±0.03	0.07 ±0.07
MC38 ND355-35	54	1.44 ±0.03	0.5 ±0.07
MC38 ND355-36	43	1.24 ±0.03	-0.15 ±0.07
MC38 ND355-37	38	1.01 ±0.03	0.39 ±0.07
MC38 ND355-38	48	1.49 ±0.03	0.23 ±0.07
MC38 ND355-39	39	0.79 ±0.03	0.46 ±0.07
MC38 ND355-40	43	0.87 ±0.03	0.27 ±0.07
MC38 ND355-42	39	1.34 ±0.03	0.19 ±0.07
MC38 ND355-43	50	1.1 ±0.03	0.19 ±0.07
MC38 ND355-44	53	1.01 ±0.03	0.31 ±0.07
MC38 ND355-46	42	0.88 ±0.03	0.04 ±0.07
MC38 ND355-47	40	1.58 ±0.03	0.28 ±0.07
MC38 ND355-48	32	1.23 ±0.03	0.5 ±0.07
MC38 ND355-49	43	1.21 ±0.03	-0.01 ±0.07
MC38 ND355-50	52	1.36 ±0.03	0.47 ±0.07

425+ μ m size fraction

*Chapter 4: Depth habitat and variance of *N. dutertrei* inferred from individual foraminifera analysis*

MC38 ND425-01	44	1.74 ±0.02	-0.41 ±0.09
MC38 ND425-02	55	1.46 ±0.02	-0.18 ±0.09
MC38 ND425-03	58	1.73 ±0.02	0.02 ±0.09
MC38 ND425-04	63	1.25 ±0.02	-0.47 ±0.09
MC38 ND425-05	58	1.21 ±0.02	-0.49 ±0.09
MC38 ND425-06	57	1.34 ±0.02	0.26 ±0.09
MC38 ND425-08	47	0.9 ±0.02	-0.52 ±0.09
MC38 ND425-09	63	1.68 ±0.02	0.09 ±0.09
MC38 ND425-10	55	1.04 ±0.02	-0.22 ±0.09
MC38 ND425-11	58	1.04 ±0.02	-0.23 ±0.09
MC38 ND425-12	53	1.2 ±0.02	-0.31 ±0.09
MC38 ND425-13	43	1.08 ±0.02	0.09 ±0.09
MC38 ND425-14	52	0.77 ±0.02	-0.07 ±0.09
MC38 ND425-15	45	1 ±0.02	0.41 ±0.09
MC38 ND425-16	49	1.06 ±0.02	0.39 ±0.09
MC38 ND425-17	53	1.07 ±0.02	-0.03 ±0.09
MC38 ND425-18	53	0.96 ±0.02	0.18 ±0.09
MC38 ND425-19	48	1.22 ±0.02	0.36 ±0.09
MC38 ND425-20	45	1.16 ±0.02	0.53 ±0.09
MC38 ND425-21	55	1.08 ±0.02	0.03 ±0.09
MC38 ND425-22	70	1.2 ±0.02	-0.31 ±0.09
MC38 ND425-24	47	0.98 ±0.02	-0.2 ±0.09
MC38 ND425-25	65	1.47 ±0.02	-0.04 ±0.09
MC38 ND425-27	45	0.79 ±0.02	-0.02 ±0.09

Table 4.1. *N. dutertrei* data from KNR195-5 MC38G. $\delta^{18}\text{O}_c$ and $\delta^{13}\text{C}$ are reported in ‰

VPDB. Errors reported are analytical error for the stable isotope measurements based on repeated analysis of laboratory standards.

Conclusions

The eastern equatorial Pacific (EEP) is a key region for understanding tropical dynamics and modulations of ENSO that impact global climate. In this thesis I have presented new reconstructions of sea surface temperature (SST) and ENSO variability from the EEP that provide for the first time, continuous records of mean SST over the past 2700 years, and ENSO activity over the past 1000 years. These records themselves are important additions to our understanding of the tropical Pacific over the past several millennia and provide constraints on future reconstructions of past oceanic conditions and important context for future climate prediction. These records have also provided clues allowing the pressing questions regarding the role of the EEP in past climate change to be addressed.

As outlined in the Introduction of this thesis, these include questions regarding the relationship between the mean state of the tropical Pacific and ENSO variability and the nature of the connections between extra-tropical forcing and tropical climate and the possible mechanisms for communication of climate signals, and the ability to detect and attribute ENSO changes. Moreover, the results address a more fundamental question driving this research: Are ENSO modulations a product of internal variability or are they the result of external climate forcings? Following is a summary of these findings.

Is the detection and attribution of ENSO signals with single specimen analysis possible?

In Chapter 1 and Appendix A, we present evidence from single-shell $\delta^{18}\text{O}_\text{c}$ analysis of *G. ruber* foraminifera, a technique that has been used to determine ENSO variability in the

Conclusions

past (Koutavas et al. 2006, Koutavas and Joanides 2012) but is limited in its ability to distinguish seasonal from interannual effects (Ford et al. 2015). It remains difficult to attribute modulations of EEP SST variance specifically to ENSO or seasonality, but evidence supporting this technique's use as an ENSO proxy was presented. The technique captures modern variance well, and the presence and frequency of highly-probably ENSO events drives much of the variance change in the record. Given that orbital forcing over the past millennium is rather small, and thus large changes in the seasonal cycle are unlikely, this evidence supports the interpretation of this record as an ENSO proxy. Applying this technique to the past millennium, distinct modes of ENSO variability related to large-scale climate shifts were identified. Additionally, for the first time, a Mid-Millennium Shift in tropical Pacific dynamics occurring at ~1500 CE is recognized, when the tropical Pacific toggled from a low-variance “La Niña-like” mean state with a strong zonal gradient to an “El Niño-like” state with active ENSO and a weak zonal gradient. This shift appears to be coincident with a southward migration of the Intertropical Convergence Zone (ITCZ) in response to high-latitude cooling (Haug et al. 2001, Schneider et al. 2014) providing a plausible link between extra-tropical climate and tropical climate dynamics.

What is the relationship between the mean state of the tropical Pacific and ENSO variability?

The Mid-Millennial Shift identified in Chapter 1 features a reversal in the zonal temperature gradient anomaly, a key feature of the tropical Pacific Ocean and diagnostic of tropical Pacific dynamics. This zonal gradient was reconstructed by comparing the

Conclusions

SST record from the EEP with comparable western Pacific records (Oppo et al. 2009) for both the past millennium (Chapter 1) and the previous millennium (Chapter 2). Over the past millennium, an inverse correlation is observed between the mean state of the tropical Pacific and ENSO activity. The period of strong zonal gradient from ~1150-1500 CE is associated with low ENSO variance, while the weak gradient observed from ~1500-1850 CE features the most active ENSO activity.

What is the nature of the connections between extra-tropical climate and tropical Pacific dynamics, and what is the mechanism for the communication of climate signals from high latitudes to the tropics?

In Chapter 2, the ~2700-year sea surface temperature (SST) record generated from Mg/Ca ratios in *G. ruber* from the EEP provides broader context to the dynamical shifts identified in Chapter 1. This new, sub-centennially resolved EEP SST record reveals a long-term cooling trend of -0.22 °C/ky, similar to trends observed in multi-proxy Northern Hemisphere temperature reconstructions (Moberg et al. 2005, Mann et al. 2009, Ljundqvist 2010, Marcott et al. 2013), Fennoscandian tree-rings (Esper et al. 2012), Greenland ice (Alley 2000) and in SST and subsurface temperature records from the western Pacific (Oppo et al. 2009, Newton et al. 2006, 2011, Linsley et al. 2010, Rosenthal et al. 2013). This similarity suggests a common origin, and I propose that this is a tropical response to high-latitude orbital forcing. (Esper et al. 2012, Ljundqvist 2010, Marcott et al. 2013). I propose a potential mechanism for transmitting high-latitude cooling from extra-tropical latitudes in the South Pacific through intermediate via the shallow overturning circulation in the Pacific (Gu and Philander, 1997). These cooled

Conclusions

waters are entrained in the Equatorial Undercurrent (EUC) and upwelled in the EEP, cooling the surface waters, similar to the mechanism proposed for long-term cooling in the western Pacific by Rosenthal et al. (2013). This mechanism provides a path for communicating observed extra-tropical cooling signals (Shevenell et al. 2011, Pahnke et al. 2003) to the tropics.

Combined with the results from Chapter 1, I propose mechanisms linking both the dynamic and thermodynamic response of the tropical Pacific to extra-tropical forcing. The thermodynamic response of the EEP to high-latitude forcing occurs via the shallow overturning circulation via cool intermediate waters upwelling in the EEP. I also propose that southward movement of the ITCZ in response to Northern Hemisphere cooling (Schneider et al. 2014) resulted in dynamical excitation of the tropical Pacific and a more active ENSO state at the Mid-Millennium shift. These results reveal interplay of dynamical and thermodynamic effects in the EEP in response to extra-tropical climate processes.

Do the records from the EEP show signs of anthropogenic carbon entry into the ocean?

In Chapter 3, I identify a 0.3‰ decrease in the mean $\delta^{13}\text{C}$ of modern foraminifera from the EEP and propose that this decrease is the result of the $\delta^{13}\text{C}$ -Suess effect. The observed $\delta^{13}\text{C}$ signal is attenuated compared to previous studies (Beveridge and Shackleton, 1994, Al-Rousan et al. 2004, Black et al. 2011). I further propose that high pCO₂ in upwelling waters of the EEP (Feeley et al. 2006) limit the penetration of the atmospheric $\delta^{13}\text{C}$ signal in the EEP. The reduced $\delta^{13}\text{C}$ of foraminifera with warmer and

Conclusions

shallower $\delta^{18}\text{O}_c$ signatures, and the relatively small changes observed in cooler- and deeper-dwelling foraminifera suggest the $\delta^{13}\text{C}$ -Suess effect influence is greater during warmer periods when pCO_2 in the EEP is reduced, allowing for greater air-sea gas exchange with the ocean surface.

Are thermocline-dwelling *N. dutertrei* foraminifera from the EEP capable of capturing ENSO variability in thermocline temperatures?

In Chapter 4, I explored the results of $\delta^{18}\text{O}_c$ obtained from individual specimens of the thermocline dwelling foraminifer *Neogloboquadrina dutertrei*. The depth habitat inferred from single-shell analysis confirms a deep-thermocline preference (Fairbanks et al. 1982, Cléroux et al. 2013, Steinhardt et al. 2015), but the $\delta^{18}\text{O}_c$ range does not include the warmest ENSO events in the modern oceanographic record, limiting this species usefulness as an ENSO proxy. Comparison with same-shell Mg/Ca records shows no significant correlation, suggesting that each method is measuring conditions from different stages in ontogeny.

Summary

This research began with an inquiry into the nature of ENSO variability and the question of whether the modes of ENSO variability are products of internal variability, or a response to external climate processes. The ability to reconstruct both ENSO variability and mean climate has allowed us to see that changes in ENSO are related to large-scale climatic events (e.g., the MCA and LIA) and that the EEP participates in large-scale climate processes. I have provided potential mechanisms by which high-latitude climate can influence both the thermodynamic response of the EEP and EEP dynamics. The

Conclusions

relationships observed and characterized here allow me to conclude that ENSO variability is not random or chaotic. I find that ENSO activity is coupled with the state of the tropical Pacific, and this paired system appears to respond to extra-tropical climate processes. These findings are vitally important to our understanding of the climate of the recent past and can inform attempts to predict climate of the future. Having demonstrated the usefulness of the experimental approaches taken here, the findings also point to a way forward for more intensive and focused application of these methods, in order to gain climatic insights from the sedimentary record of the eastern Pacific and other ocean regions

Appendix A. Supplementary Materials for Dynamical excitation of the tropical Pacific Ocean and ENSO variability by Little Ice Age cooling

Submitted as Supplementary Materials for Chapter 1, 7/11/2015, in review

Gerald T. Rustic,^{1,2,*}, Athanasios Koutavas,^{1,2,3}, Thomas M. Marchitto,⁴, and Braddock K. Linsley³

Affiliations:

¹ Department of Engineering Science and Physics, College of Staten Island, City University of New York, Staten Island, NY, 10314, USA

² Doctoral Program in Earth and Environmental Sciences, Graduate Center of the City University of New York, New York, NY, 10016, USA

³ Lamont–Doherty Earth Observatory of Columbia University, 61 Route 9W, Palisades, NY 10964, USA

⁴ Department of Geological Sciences and Institute of Arctic and Alpine Research, University of Colorado, Boulder, CO 80309, USA.

* Corresponding author: grustic@gradcenter.cuny.edu

S1. Materials and Methods

Multi-core KNR195-5 MC42 was collected by the R/V Knorr on 4/4/2009 in the Galápagos Islands ($01^{\circ} 15.58'S$, $89^{\circ} 41.13'W$, 615m depth). Section MC42C recovered 38 cm of sediment. The sediment-water interface was observed to be intact upon recovery. MC42C was stored at the Woods Hole Oceanographic Institution core repository, where it was accessed in May 2011. The core was sectioned into 66

Appendix A: Supplementary Materials for “Dynamical Excitation of the Tropical Pacific Ocean and ENSO variability by Little Ice Age Cooling

contiguous slabs with an average thickness of ~0.58 cm. In this study we report results

from the top 14 cm of core containing ~1000 years of record. The outer rind of each slab was discarded to eliminate possible contamination along the core liner. Samples were washed in a 63- μ m sieve to remove fine sediments and the coarse fractions were oven dried at 60°C. ~60 shells of *Globigerinoides ruber* (white) were picked from the 300-355 μ m fraction for single-specimen $\delta^{18}\text{O}$ analysis, and ~100 shells from the 250-300 μm fraction for Mg/Ca analysis. *G. ruber* for individual $\delta^{18}\text{O}$ analysis were classified by morphotype as *sensu stricto* (ss) or *sensu latu* (sl) (Wang 2000). Data from both morphotypes were combined in order to maximize sample sizes.

S1.1 Age Model

The age model of MC42C is based on four ^{14}C dates on *Neogloboquadrina dutertrei* (Table S1 and Figure S1). An additional ^{14}C date, also on *N. dutertrei*, was obtained from a depth of 2.0-3.0 cm in adjacent section MC42E of the same multi-core (

Table SA.1). This sample returned a reservoir-uncorrected ^{14}C age of 200±25 years, indicating post bomb-era deposition. Combined with visual observation of an intact sediment-water interface during recovery, we set the age of the core-top (0 cm) to 2009 – the year of collection. The age model is based on linear interpolation between these five age control points in the top 15 cm of MC42C (Figure 1, Table 1). Radiocarbon dating was performed at the National Ocean Sciences Accelerator Mass Spectrometry (NOSAMS) facility at Woods Hole Oceanographic Institution. Reported radiocarbon

Appendix A: Supplementary Materials for “Dynamical Excitation of the Tropical Pacific Ocean and ENSO variability by Little Ice Age Cooling
results were calibrated using Calib 6.1 with a Delta-R of 125±66 using the marine09.14c

dataset (Stuvier and Braziunas 1993). Delta-R value was calculated as the average of published reservoir ages from locations within the Galápagos (Druffel et al. 1981, Druffel et al. 2004, Taylor et al. 1967).

Sedimentation rates average 13.0 cm/ky but range from 7.9 to 27.3 cm/ky. The greatest change is observed at ~8.5 cm depth (~1494 CE). An increase in sedimentation rate at this time coincides with the “Mid-Millennium Shift” (MMS) identified and discussed in the main text, and correlates with significant changes in our climatic proxies of mean SST (Mg/Ca) and SST variance (single shell $\delta^{18}\text{O}_{\text{cV}}$). We consider the increase in sedimentation rate to be a reflection of the MMS, and is suggestive of a shift toward greater biological productivity during the Little Ice Age.

S1.2 Mg/Ca analysis

Mg/Ca ratios were measured in *G. ruber* from the 250-300 μm size fraction. ~100 *G. ruber* specimens of equal proportions *ss* and *sl* morphotypes (Wang 2000) were selected for analysis. Samples were gently crushed to expose inner chamber walls, homogenized, and split into triplicate subsamples. They were then subjected to reductive and oxidative cleaning after removal of clay-size contaminants (Boyle and Kegwin 1985, Boyle and Rosenthal, 1996). Mg/Ca ratios were analyzed on a Thermo Finnigan Element 2 ICP-MS at INSTAAR, University of Colorado (Marchitto 2006). Long-term analytical precision,

Appendix A: Supplementary Materials for “Dynamical Excitation of the Tropical Pacific Ocean and ENSO variability by Little Ice Age Cooling

based on repeat measurements of liquid standards, is $\pm 0.5\%$, or ~ 0.015 mmol/mol for

these samples. True sample reproducibility, expressed as the average standard deviation of 25 sets of triplicate analyses, is ± 0.059 mmol/mol, or ± 0.23 °C. Mg/Ca ratios were converted to SST using the relationship

$$\text{Mg/Ca} = 0.38 \exp(0.09 * \text{SST}) \text{ (Eq. 2.) (Anand et al. 2009)}$$

The surface sample, dated ~1985-2009, gave a Mg/Ca SST of 22.99 °C, which compares well (within the calibration error of ± 1.2 °C) with modern annual mean SST of 23.44 °C for 1985-2009 (from SODA 2.1.6 reanalysis data, (Carton and Giese, 2008)).

S1.3 Single-shell $\delta^{18}\text{O}_c$ analysis

Individual *G. ruber* were picked from the 300-355 μm size-fraction, weighed, and sonicated in de-ionized water before analysis. $\delta^{18}\text{O}_c$ and $\delta^{13}\text{C}_c$ were analyzed on a Thermo Delta V with Kiel device, and a VG Isoprime both with dual inlets. The instruments were located in the same laboratory at Lamont-Doherty Earth Observatory (LDEO) and were calibrated to Vienna Pee Dee Belemnite (VPDB) with routine analysis of the NBS-19 carbonate standard. Approximately one NBS-19 standard was analyzed for every two foraminifera samples. Long-term 1-sigma analytical precision was $\pm 0.09\%$ for $\delta^{18}\text{O}_c$ and $\pm 0.05\text{‰}$ for $\delta^{13}\text{C}_c$. Full results are shown in Figure S2 and summarized in

Table SA.2.

S2. Ground-truthing of single-shell $\delta^{18}\text{O}_c$ against instrumental data

In order to validate our reconstructions of variance from single-shell $\delta^{18}\text{O}_c$ of *G. ruber* we compare our measurements from modern sediments with computed $\delta^{18}\text{O}_c$ from instrumental data for the core site. $\delta^{18}\text{O}_c$ is a linear function of growth temperature $T(\text{°C})$ and $\delta^{18}\text{O}$ of seawater ($\delta^{18}\text{O}_{\text{sw}}$), which is in turn related to salinity. We used equations from ref. 8 relating $\delta^{18}\text{O}_c$, T , and $\delta^{18}\text{O}_{\text{sw}}$ to compute the predicted value of $\delta^{18}\text{O}_c$ given instrumental values of T and salinity (used to obtain $\delta^{18}\text{O}_{\text{sw}}$). These equations (3 and 4, below) were developed from culture experiments of the symbiont-bearing foraminifera *Orbulina universa* in low-light and high-light conditions (Bemis et al. 1998) and provide an appropriate bracket for most species of symbiont-bearing foraminifera, including *G. ruber*, in the 15–30°C temperature range (Spero et al. 2003).

$$T(\text{°C}) = 16.5(\pm 0.2) - 4.80(\pm 0.16)*(\delta^{18}\text{O}_c - \delta^{18}\text{O}_{\text{sw}}) \quad [\text{low-light}] \quad (\text{Eq. 3.})$$

$$T(\text{°C}) = 14.9(\pm 0.1) - 4.80(\pm 0.08)*(\delta^{18}\text{O}_c - \delta^{18}\text{O}_{\text{sw}}) \quad [\text{high-light}] \quad (\text{Eq. 4.})$$

The high-light equation (Eq. 3) was selected here as it best represents the SST– $\delta^{18}\text{O}_c$ relationship for *G. ruber* from sediment trap data (Spero et al. 2003). $\delta^{18}\text{O}_{\text{sw}}$ and salinity (S) in the EEP are related via the following equation (Fairbanks et al. 1982):

$$\delta^{18}\text{O}_{\text{sw}} = 0.260(S) - 8.773 \quad (\text{Eq. 5.})$$

For use in equation 3, $\delta^{18}\text{O}_{\text{sw}}$ from equation 4 was adjusted from VSMOW to VPDB by applying a 0.27‰ correction (Hut 1987). Using monthly SST and salinity from the *Simple Ocean Data Assimilation* (SODA) dataset for the 0.5°x0.5° grid box containing the core site (Carton and Giese 2008), we employed equations 3 and 4 to calculate the

Appendix A: Supplementary Materials for “Dynamical Excitation of the Tropical Pacific Ocean and ENSO variability by Little Ice Age Cooling

predicted monthly $\delta^{18}\text{O}_c$ values. Predicted monthly $\delta^{18}\text{O}_c$ was computed for 1958-2008

using SODA 2.1.6. For a longer comparison we also used SODA 2.2.4 covering the period 1871-2008. Due to salinity inconsistencies in SODA 2.2.4 however, we paired SODA 2.2.4 SST (1871-2008) with SODA 2.1.6 salinity for 1958-2008, and substituted climatological salinity (from SODA 2.1.6) for the period 1871-1957 (Figure SA.2). Although lack of good salinity data for 1871-1957 introduces a somewhat larger error prior to 1958, the effect of salinity on $\delta^{18}\text{O}_c$ is much smaller than that of SST, and therefore errors due to salinity are minor. The opportunity to use this longer data product adds greater insight to our results.

Multiple $\delta^{18}\text{O}_c$ analyses of individual shells (each with a life span of a few weeks to a month) can characterize the spectrum of monthly SST. This technique has shown promise for reconstructing past ENSO (Koutavas et al. 2006, Koutavas and Joanides 2012) but has yet to be properly validated against observational datasets due to lack of modern samples. Five sediment horizons in MC42C overlapping the instrumental period of the last ~150 years provided benchmark tests of this approach.

Test 1. Mean, variance and skewness of measured versus expected $\delta^{18}\text{O}_c$ for 1958-2009.

The top two sediment slices of MC42C are nominally dated to 1985-2009 and 1951-1985. We combined single-shell *G. ruber* $\delta^{18}\text{O}_c$ analyses from these two intervals (N=96) into one distribution and compared it with the distribution of monthly $\delta^{18}\text{O}_c$ computed

Appendix A: Supplementary Materials for “Dynamical Excitation of the Tropical Pacific Ocean and ENSO variability by Little Ice Age Cooling
from SODA 2.1.6 for 1958-2008 (N=612). The comparison is shown in Figure SA.4. The

two distributions have the same means (-1.87 ‰ vs. -1.86 ‰, student's t-test p<0.05), equal variances (0.26 vs. 0.24, F-test p<0.05, Brown-Forsythe p<0.05) (Brown and Forsythe, 1974, Trujillo-Ortiz and Hernandez-Walls, 2003), equal skewness (-0.46 vs. -0.47), and similar ranges (2.69‰ vs 2.48‰). Based on this comparison we conclude that the variance of $\delta^{18}\text{O}_c$ ($\delta^{18}\text{O}_c\text{V}$) of individual *G. ruber* shells faithfully captures the variance of monthly SST of the real ocean (SSTV) by virtue of the dominant control of SST on foraminiferal $\delta^{18}\text{O}_c$ (Figure SA.2).

Test 2. Temporal shifts in variance during 1871-2008.

Can *G. ruber* $\delta^{18}\text{O}_c\text{V}$ capture changes in SSTV over time? The top five sediment intervals in MC42C resolve the period 1838-2009 with multi-decadal resolution (Table 2). We used the 1871-2008 SODA data (Figure SA.2) to calculate 20-yr and 40-yr running variance of computed $\delta^{18}\text{O}_c$ for comparison with MC42C. This comparison is shown in Figure SA.5. SODA-based running variance shows a minimum in the early 20th century followed by an increase through the 20th century and a modern plateau. Reconstructed $\delta^{18}\text{O}_c\text{V}$ from *G. ruber* captures a similar pattern with a minimum in the sample corresponding to 1887-1922, followed by increasing variance and a modern plateau. In both MC42C and SODA the magnitude of the early 20th century minimum is ~20% (0.25 to 0.20) and is partly associated with an early-to-mid 20th century lull in ENSO activity. This suggests that *G. ruber* $\delta^{18}\text{O}_c\text{V}$ is responding to multidecadal

Appendix A: Supplementary Materials for “Dynamical Excitation of the Tropical Pacific Ocean and ENSO variability by Little Ice Age Cooling

modulations of ENSO. The presence of this minimum in MC42C is also important for its implications about bioturbation. If, as we believe, this minimum is a real climatic signal, its presence implies that multi-decadal signals are not erased or seriously attenuated by bioturbation. Centennial to multi-centennial signals, which comprise the bulk of our results in this study, would be even less likely to be influenced by bioturbation.

Test 3. Extreme events.

The strongest historic El Niño events of the past 150 years occurred in 1876-77, 1982-83, and 1997-98. We find plausible evidence in our raw $\delta^{18}\text{O}_c$ data (Figure SA.3) for each of these events, in the form of strong negative outliers in the sediment horizons containing these years (with the caveat that the sediment dating has uncertainties up to ± 25 years (Table 1) and no single $\delta^{18}\text{O}_c$ value can be matched to a specific event). We consider this as compelling evidence that strong El Niño events are consistently captured by *G. ruber* and that our experimental design is able to recover these events.

Evidence for positive outliers indicative of La Niña is also present in our data. Attribution to La Niña however is somewhat more complicated, because the colder signature of positive outliers may reflect a somewhat deeper calcification temperature instead of cold SST anomalies. Many (but not all) positive outliers are recorded by *sl* specimens which have an average $\delta^{18}\text{O}$ signature 0.32‰ heavier than *ss*. This could be evidence for either a slightly colder calcification depth or a colder calcification season for *sl* compared to *ss*.

We cannot distinguish between these possibilities in our data, but based on the results of tests 1-3 reported earlier, we believe the most robust conclusions about variance changes over time are deduced by combining data from both morphotypes.

S3. *G. ruber* $\delta^{18}\text{O}_c$ V as an ENSO proxy

The capture of extreme negative and positive $\delta^{18}\text{O}_c$ values that lie beyond the seasonal range of the EEP (Figure SA.3) is a strong indication that our method has potential for reconstructing ENSO activity. We asked whether there were practical thresholds of $\delta^{18}\text{O}_c$ departure from interval means that could be confidently associated with high probability of ENSO events. To answer this question we used the Oceanic NINO Index (ONI) from NOAA Climate Prediction Center (CPC, 2015) for 1958-2008 as a guide for El Niño, La Niña, and neutral conditions, and classified the 612 monthly $\delta^{18}\text{O}_c$ values of this period accordingly (Figure SA.2 D). We then calculated the probability that $\delta^{18}\text{O}_c$ values exceeding $\pm 1.0\text{‰}$ from the period mean were associated with El Niño or La Niña events. 16 of 612 monthly $\delta^{18}\text{O}_c$ values exceeded the -1.0‰ threshold with 14 of these values occurring during El Niño events, indicating a $>87\%$ probability of El Niño. For La Niña, a corresponding $+1.0\text{‰}$ threshold was not exceeded by any of the 612 calculated $\delta^{18}\text{O}_c$ values, although two La Niña months exceeded $+0.9\text{‰}$. Using a $+0.8\text{‰}$ threshold instead, we found that 7 of 12 $\delta^{18}\text{O}_c$ values exceeding this threshold were from La Niña events (58% probability). While the $+1.0\text{‰}$ threshold is not surpassed by any of the SODA predicted $\delta^{18}\text{O}_c$ values, the foraminifera record does contain such values. It is

possible that these heavy values result from a deeper calcification temperature (especially of the *sl* morphotype) rather than La Niña conditions. However, since we have used a similar proportion of *ss* and *sl* throughout our millennial record, we do not anticipate a bias from this effect in our reconstruction. We use the $\pm 1.0 \text{ ‰}$ thresholds arbitrarily to demarcate outlier values with exceptionally high probability of El Niño and La Niña events. Strictly speaking our results are not sensitive to these $\pm 1.0 \text{ ‰}$ thresholds, because our inferences are drawn from estimations of the total $\delta^{18}\text{O}_\text{cV}$ within each sample interval, and not solely from extreme outliers. However, these $\pm 1.0 \text{ ‰}$ thresholds help illustrate that there is significant modulation in our millennial record of the frequency of “high probability ENSO outliers”.

The rationale for using the total measured $\delta^{18}\text{O}_\text{cV}$ to infer an ENSO signal is that ENSO as a phenomenon comprises not only strong but also moderate and weak events. The latter produce $\delta^{18}\text{O}_\text{c}$ values that overlap with the seasonal cycle so that they cannot be explicitly discerned as ENSO events in single-shell data, even though they are part of the measured signal. Use of the total $\delta^{18}\text{O}_\text{cV}$ signal within each interval ensures that all ENSO information contained in the data is fully accounted for, but introduces the complexity that this signal is superimposed on a strong annual cycle. Changes in $\delta^{18}\text{O}_\text{cV}$ over time then, could in principle be either due to ENSO, the annual cycle, or a combination. We acknowledge that in this sense $\delta^{18}\text{O}_\text{cV}$ is an imperfect proxy for ENSO variance but consider the annual cycle unlikely to have changed appreciably on the millennial time-scale of our record because of only small changes in orbital parameters.

Appendix A: Supplementary Materials for “Dynamical Excitation of the Tropical Pacific Ocean and ENSO variability by Little Ice Age Cooling

The presence of the ENSO signal is confirmed by the statistics of the “high-probability

ENSO outliers” (i.e. values exceeding $\pm 1.0\text{‰}$ thresholds from the mean) discussed above. But limiting our inferences to such outliers only could introduce spurious effects due to their small sample size. In our judgment then, total $\delta^{18}\text{O}_{\text{cV}}$ is the more robust way to quantify the signal of ENSO modulation. The ENSO signal is superimposed on (and diluted by) a large annual cycle, which, however, in our estimation has remained relatively invariant.

If indeed our $\delta^{18}\text{O}_{\text{cV}}$ is a proxy for ENSO variance, how does it compare with other ENSO reconstructions of the past millennium? In Figure SA.6 we compare $\delta^{18}\text{O}_{\text{cV}}$ with reconstructions from central Pacific corals (Cobb et al. 2003), and from North American tree-rings (Li et al. 2011). In both cases the comparisons show significant agreement. The coral records are discontinuous but show a trend of increasing ENSO variance through the millennium, as does our $\delta^{18}\text{O}_{\text{cV}}$. The tree-ring record is more highly resolved than the sediment record yet shows similar century-scale features as our $\delta^{18}\text{O}_{\text{cV}}$ record, including a prominent 18th century maximum. Disagreement between the two records exists only in the 11th century. Considering that the tree-ring data are capturing remote hydrologic teleconnections from the tropical Pacific to North America, some disagreement is not surprising. Yet the overall match of the tree-ring and our marine reconstruction is compelling. These comparisons further support our interpretation of *G. ruber* $\delta^{18}\text{O}_{\text{cV}}$ as a signal of ENSO activity.

S4. Effects of bioturbation

Bioturbation is the disturbance and mixing of the sediment by biological activity such as infaunal burrowing. This mixes older with younger sediments, and can obscure or confound results. Our climate reconstructions were obtained from a 14 cm thick section of sediment, and therefore we need to be mindful of the potential effects of bioturbation. The fact that our measured proxies (Mg/Ca and $\delta^{18}\text{O}_{\text{cV}}$) recovered significant and systematic changes over the millennium, is by itself evidence that bioturbation has not homogenized the climatic signals. It is possible however that these signals may have been attenuated somewhat by mixing. This would imply that actual climate changes were larger than reconstructed. In this sense, our interpretations of climatic signals may be conservative.

Additional evidence against significant bioturbation comes from *G. ruber* $\delta^{13}\text{C}_{\text{c}}$. A 0.3‰ depletion is evident in the top 6 cm of MC42C, which we attribute to a Suess effect (Figure SA.7) (Keeling 1979). The appearance of this signal begins at ~1600 CE and continues forward to the present. This timing is somewhat earlier than expected, and this may indeed suggest some downward mixing by bioturbation. Clearly however sediments deposited prior to ~1600 CE show no evidence of this effect, and therefore at a minimum we can conclude that late-millennium (~1600-2009 CE) and early-millennium (1000-1600 CE) sediments as a whole have not been mixed. On finer scales, the detection of the early 20th century minimum in $\delta^{18}\text{O}_{\text{cV}}$, as predicted by SODA reanalysis data discussed

Appendix A: Supplementary Materials for “Dynamical Excitation of the Tropical Pacific Ocean and ENSO variability by Little Ice Age Cooling

earlier (Figure SA.5), implies that multi-decadal signals are also recoverable from the

sediments. The same can be said for the negative $\delta^{18}\text{O}_c$ outliers plausibly associated with the historic El Niños of 1876-77, 1982-83, and 1997-98 (Figure SA.3). Overall, the coherency of the modern sediment record with the instrumental data, the presence of a robust Suess effect, and the recovery of systematic climate signals from the analyzed core section, collectively attest to the integrity of the record and to minimal influence of bioturbation.

As a final consistency check we compared our *G. ruber* mean $\delta^{18}\text{O}_c$ values with annual $\delta^{18}\text{O}$ values of coral from Urvina Bay in Isabela Island, Galápagos (Dunbar et al. 1994) (Figure SA.8). Although the two records differ in resolution, we find substantial coherency between them and no evidence of divergence in their signals. Both show multidecadal fluctuations in $\delta^{18}\text{O}$ of $\pm 0.1 \text{ ‰}$, and both show positive $\delta^{18}\text{O}$ excursions in the early 20th century, which are coeval within the dating error of MC42C ($\pm 20 \text{ y}$).

Tables

NOSAMS Accession ID	Core Depth	Radiocarbon Age (y)	Calibrated Date	1-sigma range	2-sigma range
-	0 cm	—	2009 CE	-	-
OS-86755	2-3 cm (MC42E)	200 ± 25	>1950 CE	N/A	N/A
OS-93340	5.0-5.5 cm	805 ±25	1611 CE	1539 - 1682 CE	1479 - 1774 CE
OS-113967	8.1-8.7 cm	950 ±20	1494 CE	1433 - 1555 CE	1401 - 1651 CE
OS-113968	11.8-12.3 cm	1390 ±15	1137 CE	1065 - 1209 CE	1018 - 1278 CE
OS-93341	14.8-15.5 cm	1770 ±25	745 CE	674 - 816 CE	616 - 908 CE

Table SA.1. ^{14}C analyses and age control points for KNR195-5 MC42C. ^{14}C age at 2-3 cm depth is from section MC42E. Depths are corrected for small variations in slab thickness during sampling. The age of the core-top was assigned to the year of collection (2009). All ^{14}C ages were on *N. dutertrei*.

Appendix A: Supplementary Materials for “Dynamical Excitation of the Tropical Pacific Ocean and ENSO variability by Little Ice Age Cooling

Depth (cm)	Age (CE)	N	$\delta^{18}\text{Oc}$ mean	$\delta^{18}\text{Oc}$ variance ($\delta^{18}\text{OcV}$)	$\delta^{18}\text{Oc}$ skew	Mg/Ca SST
<i>Modern</i>						
0-0.3	**1985-2009 ±2	39	-1.78 ±0.08	0.24 ±0.06	-0.92	22.99 ±0.13
0.3-0.8	1951-1985 ±7	57	-1.92 ±0.07	0.27 ±0.05	-0.24	22.58 ±0.16
0.8-1.1	1922-1951 ±13	58	-1.97 ±0.06	0.24 ±0.05	0.72	22.54 ±0.18
1.1-1.6	1887-1922 ±19	59	-1.69 ±0.06	0.19 ±0.04	0.26	21.77 ±0.38
1.6-2.2	1838-1887 ±26	55	-1.85 ±0.07	0.25 ±0.05	-0.12	22.24 ±0.15
<i>LIA</i>						
2.2-2.7	1800-1838 ±34	54	-1.81 ±0.06	0.22 ±0.04	-0.28	22.42 ±0.22
2.7-3.3	1756-1800 ±41	60	-1.91 ±0.07	0.32 ±0.06	0.17	22.53 ±0.40
3.3-3.8	1717-1756 ±49	50	-1.85 ±0.08	0.32 ±0.06	0.21	21.83 ±0.16
3.8-4.4	1672-1717 ±56	55	-1.88 ±0.05	0.16 ±0.03	0.15	22.23 ±0.21
4.4-4.9	1632-1672 ±64	55	-1.76 ±0.07	0.27 ±0.05	-0.08	22.70 ±0.73
4.9-5.5	*1590-1632 ±72	51	-1.8 ±0.07	0.22 ±0.04	0	22.43 ±0.08
5.5-6.3	1572-1590 ±69	52	-1.8 ±0.07	0.27 ±0.05	0.36	21.90 ±0.15
6.3-6.7	1555-1572 ±67	57	-1.79 ±0.07	0.26 ±0.05	-0.29	22.21 ±0.07
6.7-7.4	1532-1555 ±65	60	-1.83 ±0.05	0.15 ±0.03	-0.01	21.79 ±0.31
7.4-8.1	1503-1532 ±63	58	-1.88 ±0.06	0.18 ±0.03	-0.39	21.94 ±0.25
<i>Late MCA / Early LIA</i>						
8.1-8.7	*1469-1503 ±61	57	-1.74 ±0.06	0.22 ±0.04	0.55	21.70 ±0.41
8.7-9.2	1413-1469 ±63	56	-1.78 ±0.06	0.19 ±0.04	0.4	21.73 ±0.15
9.2-10	1340-1413 ±65	54	-1.74 ±0.06	0.17 ±0.03	0.26	21.86 ±0.36
10-10.6	1280-1340 ±67	56	-1.76 ±0.06	0.17 ±0.03	-0.32	22.04 ±0.15
10.6-11.1	1231-1280 ±68	60	-1.81 ±0.06	0.19 ±0.03	-0.03	22.02 ±0.16
11.1-11.8	1163-1231 ±70	57	-1.77 ±0.06	0.19 ±0.04	-0.26	22.27 ±0.20

Peak MCA							
11.8-12.3	*1103-1163 ±72	56	-1.74 ±0.07	0.25 ±0.05	0.3	22.80 ±0.15	
12.3-13	1022-1103 ±72	50	-1.86 ±0.07	0.22 ±0.04	0.25	22.72 ±0.11	
13-13.5	958-1022 ±72	59	-1.68 ±0.07	0.26 ±0.05	0.39	22.63 ±0.26	
13.5-14.2	864-958 ±71	++	++	++	++	22.4 ±0.25	

Table SA.2. List of analyzed MC42C sample intervals and their climate data. Age ranges show years CE (Common Era) with 1-sigma age uncertainty. Stars (*) indicate ^{14}C dated intervals. Double-star (**) indicates core top sample dated to the year of collection (2009). Samples were assigned to four age groups (Modern, LIA, Late MCA, Peak MCA) based on their midpoint ages. N is the number of *G. ruber* shells analyzed individually, and $\delta^{18}\text{O}_\text{c}$ mean is the average of individual analyses shown with the standard error of the mean. Variance is computed as the squared standard deviation of the individual $\delta^{18}\text{O}_\text{c}$ analyses, shown with the standard error of the variance. Errors on Mg/Ca SST indicate the standard deviation of triplicate Mg/Ca analyses. Individual *G. ruber* were not analyzed in the 13.5-14.2 cm interval (indicated by ++).

Figures

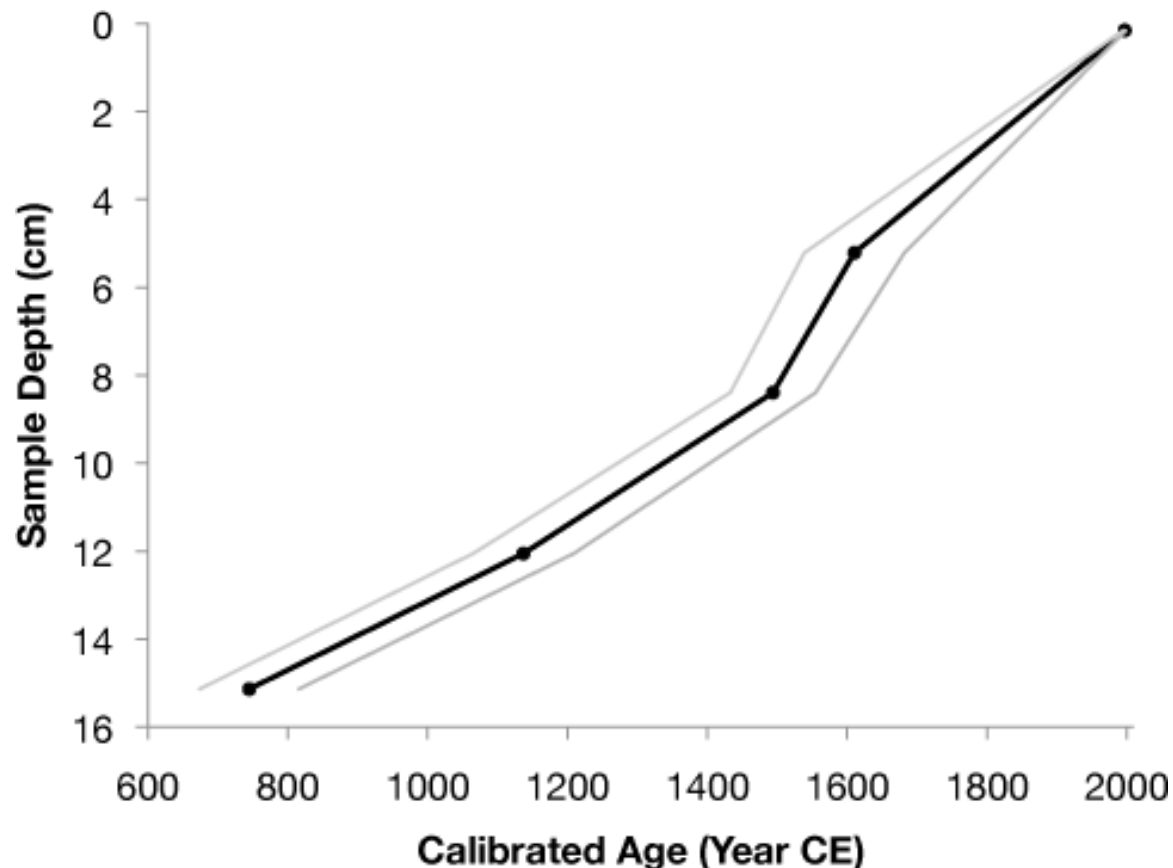


Figure SA.1. MC42C age model with 1-sigma age uncertainty. Age control points are ^{14}C ages (Table S1), except the multicore-top which is assigned the year of collection (2009) with zero uncertainty.

Appendix A: Supplementary Materials for “Dynamical Excitation of the Tropical Pacific Ocean and ENSO variability by Little Ice Age Cooling

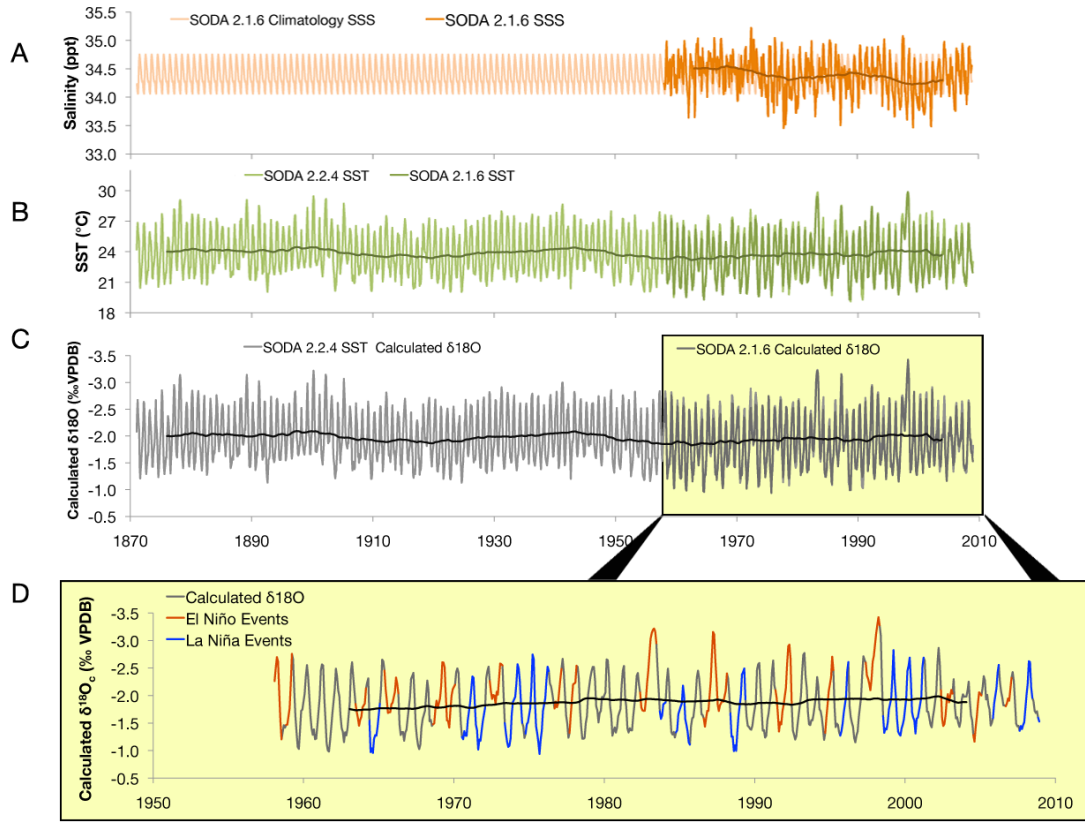
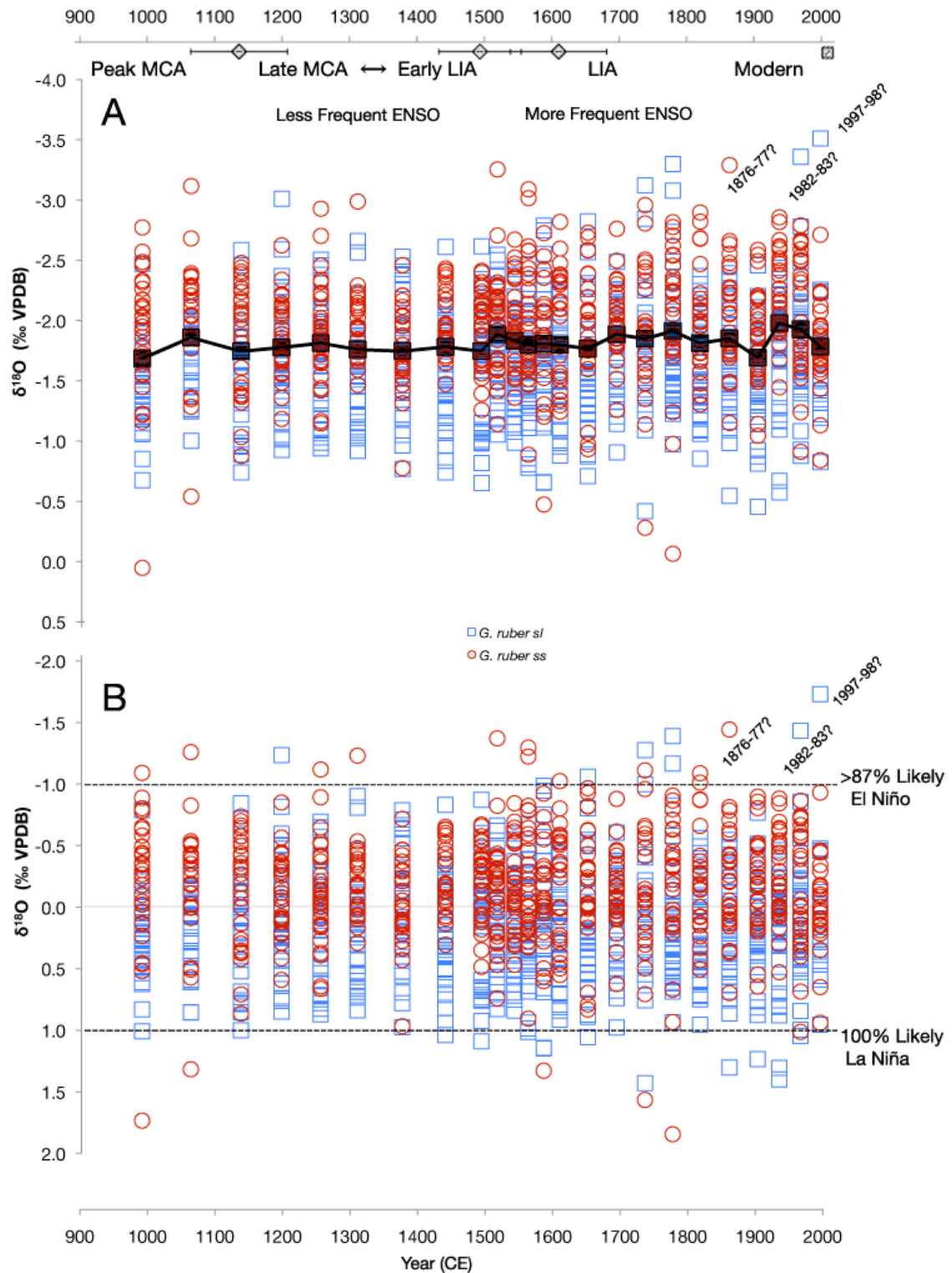


Figure SA.2. Time series of monthly sea surface temperature (SST), salinity (SSS), and computed $\delta^{18}\text{O}_c$ from SODA reanalysis data, for the $0.5^\circ \times 0.5^\circ$ grid box surrounding the study site (Carton and Giese 2008). 10-year centered moving averages are shown as dark lines in each panel. (A) Monthly SSS from SODA 2.1.6 (1958-2008). Average SSS climatology is substituted for 1871-1957, needed to compute $\delta^{18}\text{O}_c$. (B) Monthly SST from SODA 2.2.4 (1871-2008) (light green) and SODA 2.1.6 (1958-2008, darker green). (C) Computed monthly $\delta^{18}\text{O}_c$ from SSS and SST using equations (4) and (5) as explained in the text. Note that the $\delta^{18}\text{O}_c$ signal is driven almost entirely by SST (86% of the monthly variance of $\delta^{18}\text{O}_c$ is due to SST) with SSS having a minor role. (D) Expanded $\delta^{18}\text{O}_c$ for 1958-2009 from (C) indicating El Niño (red), La Niña (blue) and ENSO-neutral

Appendix A: Supplementary Materials for “Dynamical Excitation of the Tropical Pacific Ocean and ENSO variability by Little Ice Age Cooling

conditions (gray) as defined by the Ocean NINO Index (CPC, 2015). Although ENSO conditions are not always associated with extreme values, all extreme values (negative and positive) are associated with ENSO conditions.

Appendix A: Supplementary Materials for “Dynamical Excitation of the Tropical Pacific Ocean and ENSO variability by Little Ice Age Cooling”



Appendix A: Supplementary Materials for “Dynamical Excitation of the Tropical Pacific Ocean and ENSO variability by Little Ice Age Cooling

Figure SA.3. $\delta^{18}\text{O}_c$ data of individual *G. ruber* from KNR195-5 MC42C. (A) Raw $\delta^{18}\text{O}_c$

data from MC42C. The black line shows the mean $\delta^{18}\text{O}_c$ value for each interval. (B)

$\delta^{18}\text{O}_c$ data with interval means removed. For both, red circles denote *G. ruber ss*, and

blue squares *G. ruber sl* morphotypes. On average *ss* is 0.32‰ lighter than *sl*, but

extreme values can be recorded by either morphotype. We combined data from both to

obtain the most robust estimates of sample variance in accordance with the tests

described in section 2. The percentage of *ss* to *sl* has been maintained approximately

constant throughout the record ($46\% \pm 5\%$ *ss*) with the exception of the uppermost

interval (65% *ss*, due to small sample size and few *sl* present).

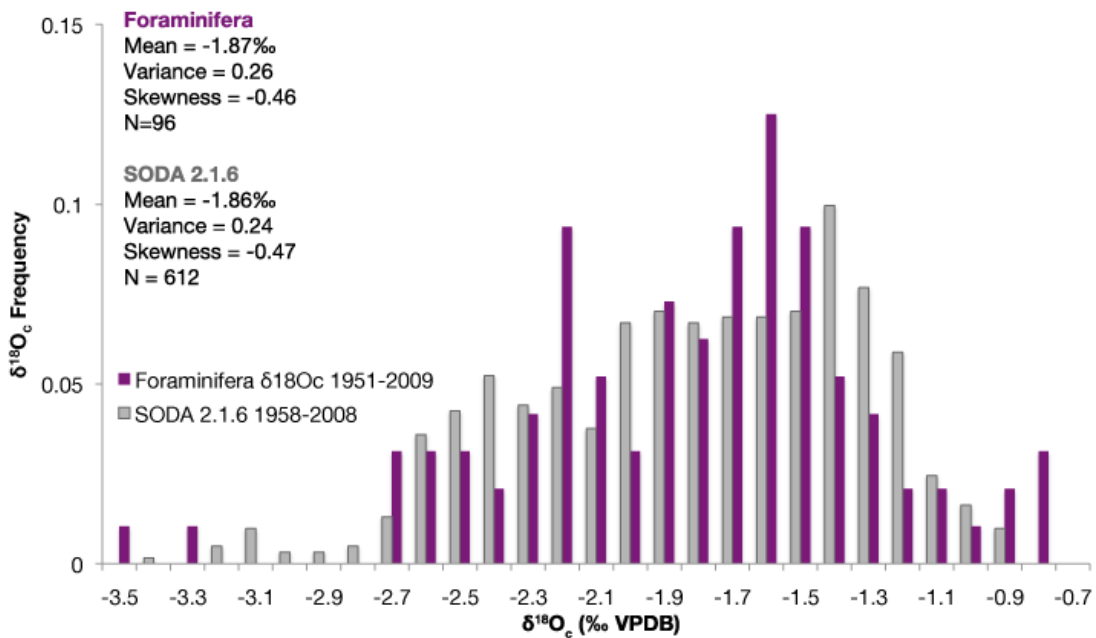


Figure SA.4. Comparison of $\delta^{18}\text{O}_c$ values measured on *G. ruber* single shells from surface sediments (1951-2009, purple), and computed from SODA 2.1.6 reanalysis data (1958-2009, gray). The mean, variance and skewness of each distribution are given.

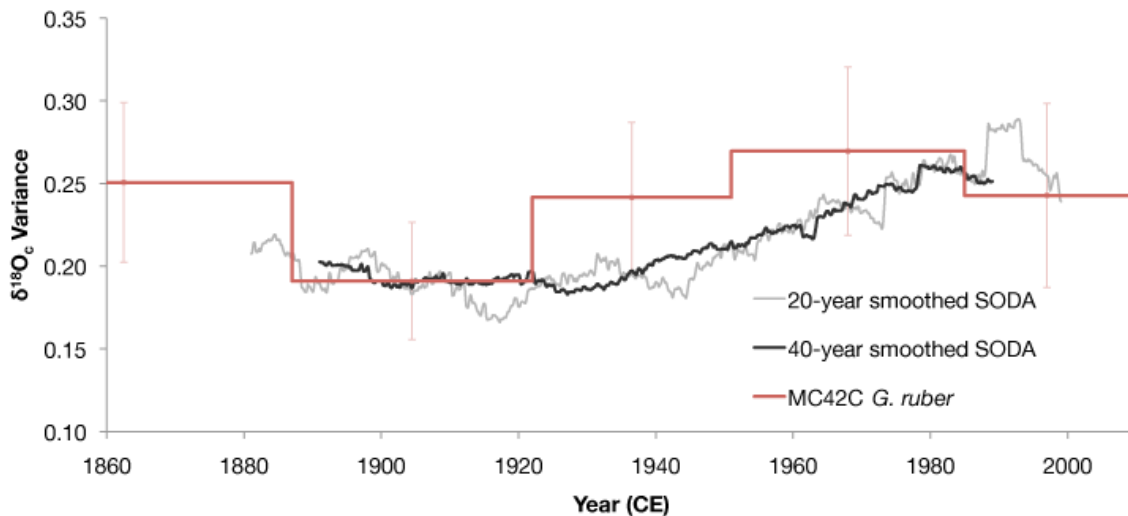


Figure SA.5. Reconstructed versus instrumental $\delta^{18}\text{O}_c$ variance for 1860-2009. Single-shell *G. ruber* $\delta^{18}\text{O}_c$ variance measured on MC42C is shown in red. Gray and black lines are the 20-year and 40-year centered variance of the computed $\delta^{18}\text{O}_c$ from SODA 2.2.4 monthly SST/salinity data as described in the text. The reconstructed *G. ruber* variance captures the early 20th century minimum evident in the SODA reanalysis, and the subsequent increase in variance. Moreover both approaches give similar values for the variance, and capture similar amplitudes of change.

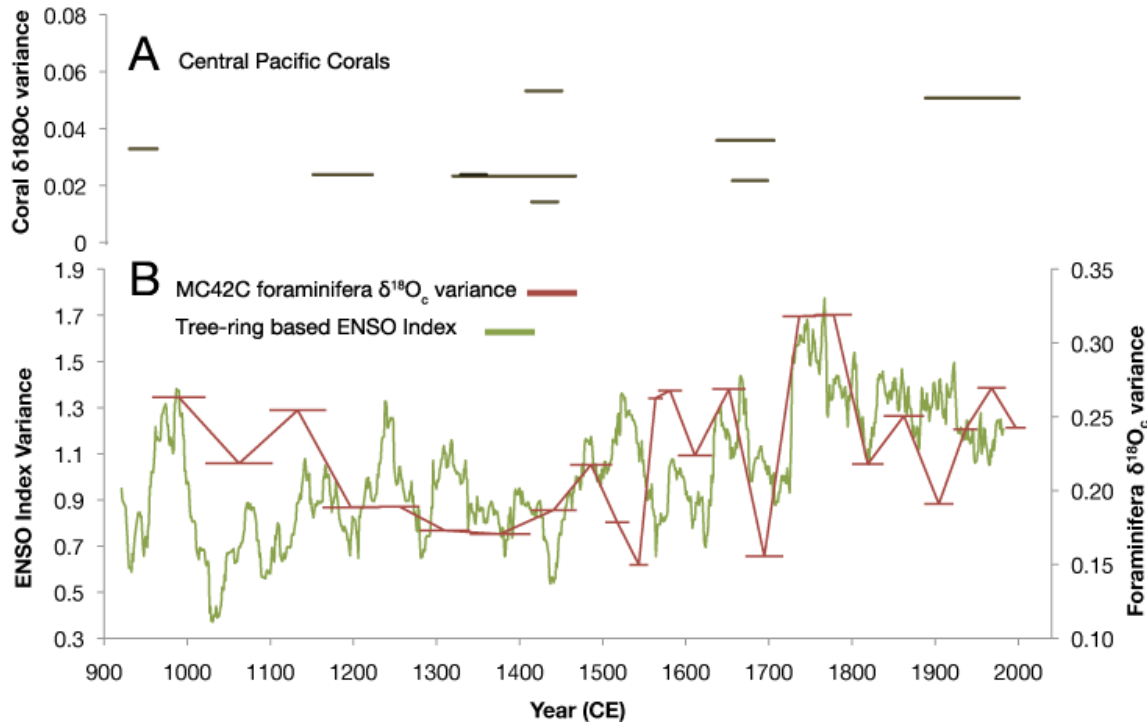


Figure SA.6. Records of ENSO variance during the past millennium. (A) $\delta^{18}\text{O}_c$ variance from central Pacific corals (Cobb et al. 2003, Cobb et al. 2013). Each horizontal line indicates the total variance within the interval captured by a single coral. (B) *G. ruber* $\delta^{18}\text{O}_c$ V from MC42C, Galápagos (red), and 40-year centered ENSO variance from North American tree rings (green) (Li et al. 2011).

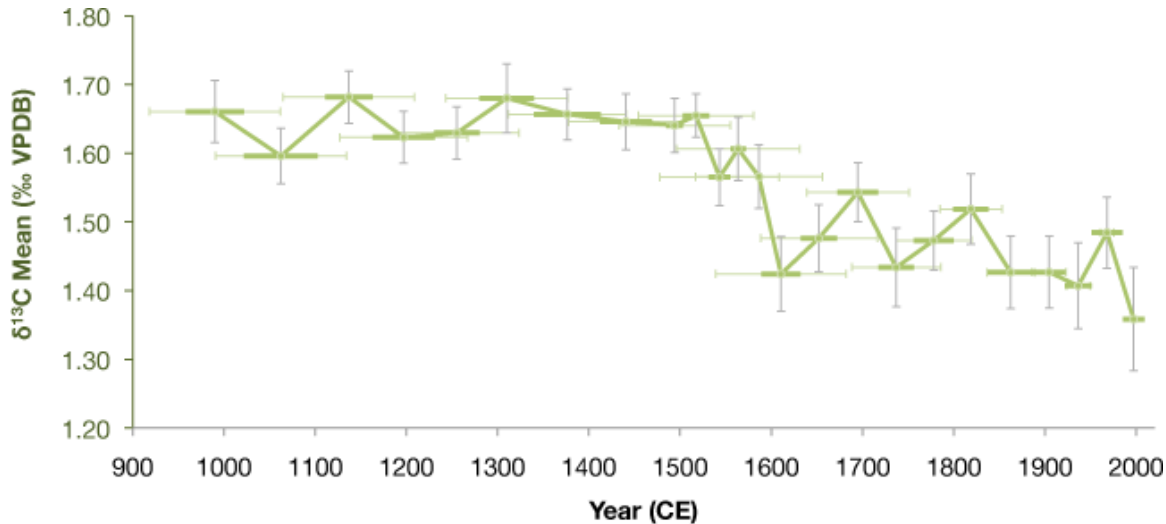


Figure SA.7. *G. ruber* mean $\delta^{13}\text{C}_c$ from MC42C. A decrease in $\delta^{13}\text{C}_c$ beginning ~ 1600 CE and intensifying through the present indicates a Suess effect. Width of the bar represents the length of the interval. Horizontal whiskers show the 1-sigma age error. Vertical whiskers represent the standard error of the mean. The sharp onset of a 0.3 ‰ Suess effect ~ 1600 CE implies that pre- and post-1600 CE sediments have not been mixed by bioturbation.

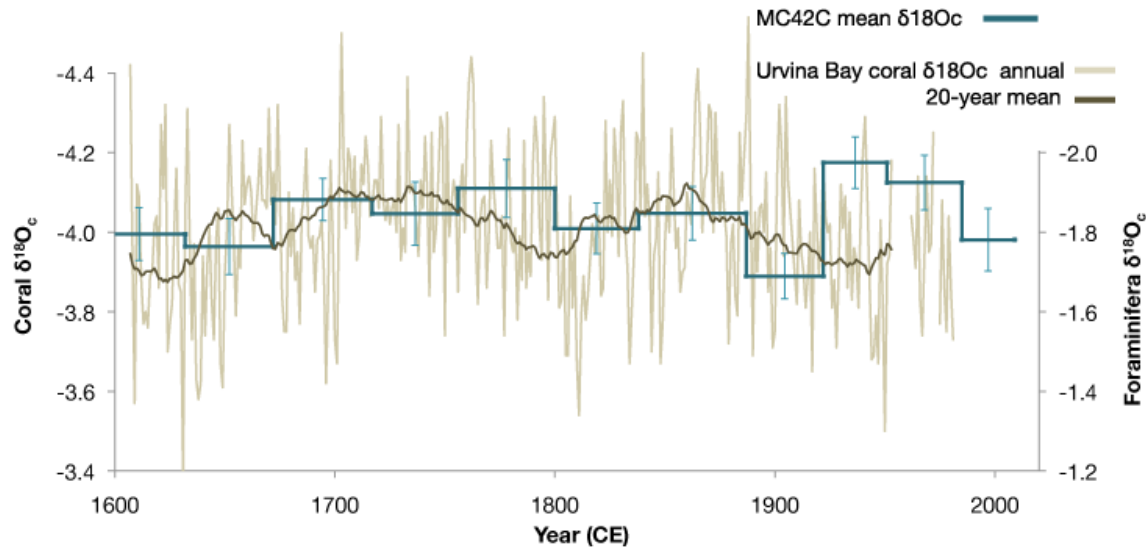


Figure SA.8. Comparison of mean $\delta^{18}\text{O}_c$ from MC42C and an Urvina Bay coral (Dunbar et al. 1994). Both records are from the Galápagos region. The dark brown line through the coral data is a 20-year centered moving average. Both records show evidence of a $\delta^{18}\text{O}$ maximum in the beginning of the 20th century. Coral data are from *Pavona clavus* (1607-1953), and from *Pavona gigantea* (1962-1981), the latter adjusted by +0.4 ‰ (Dunbar et al. 1994).

Bibliography and References

- Al-Rousan, S., Pätzold, J., Al-Moghrabi, S. & Wefer, G. Invasion of anthropogenic CO₂ recorded in planktonic foraminifera from the northern Gulf of Aqaba. *International Journal of Earth Sciences* **93**, 1066–1076 (2004).
- Alley, R. B. The Younger Dryas cold interval as viewed from central Greenland. *Quaternary Science Reviews* **19**, 213–226 (2000).
- Anand, P., Elderfield, H. & Conte, M. H. Calibration of Mg/Ca thermometry in planktonic foraminifera from a sediment trap time series. *Paleoceanography* **18**, 28–31 (2003).
- Anderson, E. C. & Hayes, F. N. Recent advances in low level counting techniques. *Annual review of nuclear science* **6**, 303–316 (1956).
- Andres, R.J., Boden, T.A., Bréon, F.-M., Ciais, P., Davis, S., Erickson, D., Gregg, J.S., Jacobson, A., Marland, G., Miller, J., Oda, T., Oliver, J. G. J., Raupach, M. R., Rayner, P., Treanton, K. A synthesis of carbon dioxide emissions from fossil-fuel combustion. *Biogeosciences* **9**, 1845–1871 (2012).
- Andres, R.J. T.A. Boden, and G. Marland, Annual Fossil-Fuel CO₂ Emissions: Global Stable Carbon Isotopic Signature. Carbon Dioxide Information Analysis Center, Oak Ridge National Laboratory, U.S. Department of Energy, Oak Ridge, Tenn., U.S.A. (2013)
- Ashok, K., Behera, S. K., Rao, S. A., Weng, H., & Yamagata, T. El Niño Modoki and its possible teleconnection. *Journal of Geophysical Research: Oceans (1978–2012)*, **112(C11)** (2007).
- Barnston, A. G., Tippett, M. K., van den Dool, H. M. & Unger, D. A. Toward an Improved Multimodel ENSO Prediction. *J. Appl. Meteor. Climatol.* **54**, 1579–1595 (2015).

Bibliography and References

- Bauch, D., Carstens, J., Wefer, G. & Thiede, J. The imprint of anthropogenic CO₂ in the Arctic Ocean: Evidence from planktic δ¹³C data from watercolumn and sediment surfaces. *Deep Sea Research Part II: Topical Studies in Oceanography* **47**, 1791–1808 (2000).
- Bé, A. W. H. & Lott, L. Shell Growth and Structure of Planktonic Foraminifera. *Science* **145**, 823–824 (1964).
- Bemis, B. E., Spero, H. J., Bijma, J. & Lea, D. W. Reevaluation of the oxygen isotopic composition of planktonic foraminifera: Experimental results and revised paleotemperature equations. *Paleoceanography* **13**, 150–160 (1998).
- Bemis, B. E., Spero, H. J., Lea, D. W. & Bijma, J. Temperature influence on the carbon isotopic composition of *Globigerina bulloides* and *Orbulina universa* (planktonic foraminifera). *Marine Micropaleontology* **38**, 213–228 (2000).
- Berger, W. H., Killingley, J. S. & Vincent, E. Stable isotopes in deep-sea carbonates-box core ERDC-92, west equatorial Pacific. *Oceanologica Acta* **1**, 203–216 (1978).
- Beveridge, N. A. S. & Shackleton, N. J. Carbon isotopes in recent planktonic foraminifera: A record of anthropogenic CO₂ invasion of the surface ocean. *Earth and Planetary Science Letters* **126**, 259–273 (1994).
- Bijma, J., Spero, H. J. & Lea, D. W. in *Use of proxies in paleoceanography* 489–512 (Springer, 1999).
- Black, D., Thunell, R., Wejnert, K. & Astor, Y. Carbon isotope composition of Caribbean Sea surface waters: Response to the uptake of anthropogenic CO₂. *Geophysical Research Letters* **38**, (2011).
- Bjerknes, J. Atmospheric Teleconnections from the Equatorial Pacific 1. *Monthly Weather Review* **97**, 163–172 (1969).
- Black, D., Thunell, R., Wejnert, K. & Astor, Y. Carbon isotope composition of Caribbean Sea surface waters: Response to the uptake of anthropogenic CO₂. *Geophysical Research Letters* **38**, (2011).

Bibliography and References

- Böhm, F., Joachimski, M. M., Lehnert, H., Morgenroth, G., Kretschmer, W., Vacelet, J., & Dullo, W. C. Carbon isotope records from extant Caribbean and South Pacific sponges: Evolution of $\delta^{13}\text{C}$ in surface water DIC. *Earth and Planetary Science Letters* **139**, 291–303 (1996).
- Böhm, F., Haase-Schramm, A., Eisenhauer, A., Dullo, W. C., Joachimski, M. M., Lehnert, H., & Reitner, J. Evidence for preindustrial variations in the marine surface water carbonate system from coralline sponges. *Geochem.-Geophys.-Geosyst.* **3**, 1–13 (2002).
- Bolin, B. & Eriksson, E. Changes in the carbon dioxide content of the atmosphere and sea due to fossil fuel combustion. *The atmosphere and the sea in motion* **1**, 30–142 (1959).
- Boyle, E. A. & Keigwin, L. D. Comparison of Atlantic and Pacific paleochemical records for the last 215,000 years: changes in deep ocean circulation and chemical inventories. *Earth and Planetary Science Letters* **76**, 135–150 (1985).
- Boyle, E. A. & Rosenthal, Y. *The South Atlantic: Present and Past Circulation*. (Springer-Verlag, 1996).
- Broecker, W. S. & Maier-Reimer, E. The influence of air and sea exchange on the carbon isotope distribution in the sea. *Global Biogeochemical Cycles* **6**, 315–320 (1992).
- Brown, M. B. & Forsythe, A. B. Robust Tests for the Equality of Variances. *Journal of the American Statistical Association* **69**, 364–367 (1974).
- Cai, W., Borlace, S., Lengaigne, M., Van Renssch, P., Collins, M., Vecchi, G., Timmermann, A., Santoso, A., McPhaden, M. J., Wu, L., England, M. H., Wang, G., Guilyardi, E. & Jin, F. F. Increasing frequency of extreme El Niño events due to greenhouse warming. *Nature Climate Change* **4**, 111–116 (2014).
- Cai, W., Wang, G., Santoso, A., McPhaden, M. J., Wu, L., Jin, F. F., Timmermann, A., Collings, M., Vecchi, G., Lengaigne, M., England, M., Dommegård, D.,

Bibliography and References

- Takahashi, K. & Guilyardi, E. Increased frequency of extreme La Niña events under greenhouse warming. *Nature Climate Change* **5**, 132–137 (2015).
- Cane, M. A. A role for the tropical Pacific? *Science* **282**, 59–61 (1998)
- Cane, M. A. Oceanographic events during El Niño. *Science* **222**, 1189–1195 (1983).
- Carton, J. A. & Giese, B. S. A reanalysis of ocean climate using Simple Ocean Data Assimilation (SODA). *Monthly Weather Review* **136**, 2999–3017 (2008).
- Carton, J.A. & Giese, B.S. *CARTON-GIESE SODA SODA 2.2.4, 1871-2008 Assimilation Run: Oceanic and air-sea interface data from the UMD Simple Ocean Data Assimilation Reanalysis.* (2010).
- Chiang, J. C. H. The tropics in paleoclimate. *Annual Review of Earth and Planetary Sciences* **37**, 263–297 (2009).
- Chiang, J. C. & Bitz, C. M. Influence of high latitude ice cover on the marine Intertropical Convergence Zone. *Climate Dynamics* **25**, 477–496 (2005).
- Clark, S. *Thermocline structure and El Niño-Southern Oscillation variability in the eastern equatorial Pacific under Last Glacial Maximum climate*, Master's thesis, Program in Environmental Science, College of Staten Island. (2014).
- Clement, A. C., Seager, R., Cane, M. A. & Zebiak, S. E. An ocean dynamical thermostat. *Journal of Climate* **9**, 2190–2196 (1996).
- Clement, A. C., Seager, R. & Cane, M. A. Suppression of El Niño during the mid-Holocene by changes in the Earth's orbit. *Paleoceanography* **15**, 731–737 (2000).
- Cléroux, C., deMenocal, P., Arbuszewski, J. & Linsley, B. Reconstructing the upper water column thermal structure in the Atlantic Ocean. *Paleoceanography* **28**, 503–516 (2013).
- Climate Prediction Center - Monitoring & Data: ENSO Impacts on the U.S. - Previous Events. at

Bibliography and References

http://www.cpc.ncep.noaa.gov/products/analysis_monitoring/ensostuff/ensoyears_ERSSSTv3b.shtml

- Cobb, K. M., Westphal, N., Sayani, H. R., Watson, J. T., Di Lorenzo, E., Cheng, H., Edwards, R. L. & Charles, C. D. Highly Variable El Niño–Southern Oscillation Throughout the Holocene. *Science* **339**, 67–70 (2013).
- Cobb, K. M., Charles, C. D., Cheng, H., & Edwards, R. L. El Niño/Southern Oscillation and tropical Pacific climate during the last millennium. *Nature* **424**, 271–276 (2003).
- Collins, M., An, S. I., Cai, W., Ganachaud, A., Guilyardi, E., Jin, F. F., Jochum, M., Lengaigne, M., Power, S., Timmermann, A., Vecchi, G., & Wittenberg, A. The impact of global warming on the tropical Pacific Ocean and El Niño. *Nature Geoscience* **3**, 391–397 (2010).
- Conroy, J. L., Overpeck, J. T., Cole, J. E., Shanahan, T. M. & Steinitz-Kannan, M. Holocene changes in eastern tropical Pacific climate inferred from a Galápagos lake sediment record. *Quaternary Science Reviews* **27**, 1166–1180 (2008).
- Conroy, J. L., Restrepo, A., Overpeck, J. T., Steinitz-Kannan, M., Cole, J. E., Bush, M. B., & Colinvaux, P. A. Unprecedented recent warming of surface temperatures in the eastern tropical Pacific Ocean. *Nature Geoscience* **2**, 46–50 (2009).
- Cook, E. R., Woodhouse, C. A., Eakin, C. M., Meko, D. M. & Stahle, D. W. Long-term aridity changes in the western United States. *Science* **306**, 1015–1018 (2004).
- Craig, H. The natural distribution of radiocarbon and the exchange time of carbon dioxide between atmosphere and sea. *Tellus A* **9**, (1957).
- Crowley, T. J. & Unterman, M. B. Technical details concerning development of a 1200 yr proxy index for global volcanism. *Earth System Science Data* **5**, 187–197 (2013).

Bibliography and References

- D'Arrigo, R., Cook, E.R., Wilson, R. J, Allan, R, Mann, M.E., On the variability of ENSO over the past six centuries, *Geophysical Research Letters*, **32**, L03711 (2005)
- Dassié, E. P., Lemley, G. M. & Linsley, B. K. The Suess effect in Fiji coral $\delta^{13}\text{C}$ and its potential as a tracer of anthropogenic CO₂ uptake. *Palaeogeography, Palaeoclimatology, Palaeoecology* **370**, 30–40 (2013).
- Dekens, P. S., Lea, D. W., Pak, D. K. & Spero, H. J. Core top calibration of Mg/Ca in tropical foraminifera: Refining paleotemperature estimation. *Geochem. Geophys. Geosyst* **3**, 1022 (2002).
- Deser, C. & Wallace, J. M. Large-scale atmospheric circulation features of warm and cold episodes in the tropical Pacific. *Journal of Climate* **3**, 1254–1281 (1990).
- Deser, C., Phillips, A. S. & Alexander, M. A. Twentieth century tropical sea surface temperature trends revisited. *Geophys. Res. Lett.* **37**, L10701 (2010).
- Druffel, E. M. Radiocarbon in annual coral rings from the eastern tropical Pacific Ocean. *Geophysical Research Letters* **8**, 59–62 (1981).
- Druffel, E. R. & Benavides, L. M. Input of excess CO₂ to the surface ocean based on $^{13}\text{C}/^{12}\text{C}$ ratios in a banded Jamaican sclerosponge. *Nature* **321**, 58–61 (1986).
- Druffel, E. R., Griffin, S., Hwang, J., Komada, T., Beaupre, S. R., Druffel-Rodriguez, K. C., Santos, G. & Southon, J. R. Variability of monthly radiocarbon during the 1760s in corals from the Galapagos Islands. *Radiocarbon* **46**, 627–631 (2004).
- Dunbar, R. B., Wellington, G. M., Colgan, M. W. & Glynn, P. W. Eastern Pacific sea surface temperature since 1600 AD: The $\delta^{18}\text{O}$ record of climate variability in Galápagos corals. *Paleoceanography* **9**, 291–315 (1994).
- Boyle, E.A. & Rosenthal, Y. in The South Atlantic: Present and Past Circulation, G. Wefer, e. al., Eds. (Springer-Verlag, Berlin, 1996), pp. 423-443.

Bibliography and References

- Eggins, S., De Deckker, P. & Marshall, J. Mg/Ca variation in planktonic foraminifera tests: implications for reconstructing palaeo-seawater temperature and habitat migration. *Earth and Planetary Science Letters* **212**, 291–306 (2003).
- Elderfield, H., Vautravers, M. & Cooper, M. The relationship between shell size and Mg/Ca, Sr/Ca, $\delta^{18}\text{O}$, and $\delta^{13}\text{C}$ of species of planktonic foraminifera. *Geochemistry, Geophysics, Geosystems* **3**, 1–13 (2002).
- Emile-Geay, J., Cobb, K. M., Mann, M. E. & Wittenberg, A. T. Estimating central equatorial Pacific SST variability over the past millennium. Part II: Reconstructions and implications. *Journal of Climate* **26**, 2329–2352 (2013).
- Emiliani, C. Pleistocene Temperatures. *The Journal of Geology* **63**, 538–578 (1955).
- England, M. H., McGregor, S., Spence, P., Meehl, G. A., Timmermann, A., Cai, W., Gupta, A. S., McPhaden, M. J., Purich, A., & Santoso, A. Recent intensification of wind-driven circulation in the Pacific and the ongoing warming hiatus. *Nature Climate Change* **4**, 222–227 (2014).
- Epstein, S., Buchsbaum, R., Lowenstam, H. A. & Urey, H. C. Revised carbonate-water isotopic temperature scale. *Geological Society of America Bulletin* **64**, 1315–1326 (1953).
- Esper, J., Büntgen, U., Timonen, M. & Frank, D. C. Variability and extremes of northern Scandinavian summer temperatures over the past two millennia. *Global and Planetary Change* **88–89**, 1–9 (2012).
- Fairbanks, R. G., Wiebe, P. H. & Bé, A. W. Vertical distribution and isotopic composition of living planktonic foraminifera in the western North Atlantic. *Science* **207**, 61–63 (1980).
- Fairbanks, R. G., Sverdlove, M., Free, R., Wiebe, P. H. & Bé, A. W. H. Vertical distribution and isotopic fractionation of living planktonic foraminifera from the Panama Basin. *Nature* **298**, 841–844 (1982).

Bibliography and References

- Fedorov, A. V., Hu, S., Lengaigne, M., & Guilyardi, E. The impact of westerly wind bursts and ocean initial state on the development, and diversity of El Niño events. *Climate Dynamics*, 44(5-6), 1381-1401 (2014)
- Feely, R. A., Takahashi, T., Wanninkhof, R., McPhaden, M. J., Cosca, C. E., Sutherland, S. C., & Carr, M. E. Decadal variability of the air-sea CO₂ fluxes in the equatorial Pacific Ocean. *Journal of Geophysical Research: Oceans (1978–2012)* **111**, (2006).
- Fiedler, P. C. & Talley, L. D. Hydrography of the eastern tropical Pacific: A review. *Progress in Oceanography* **69**, 143–180 (2006).
- Ford, H. L., Ravelo, A. C. & Polissar, P. J. Reduced El Niño–Southern Oscillation during the Last Glacial Maximum. *Science* **347**, 255–258 (2015).
- Fowler, A. M. ENSO history recorded in Agathis australis (kauri) tree rings. Part B: 423 years of ENSO robustness. *International Journal of Climatology* **28**, 21–35 (2008).
- Francey, R. J., Allison, C. E., Etheridge, D. M., Trudinger, C. M., Enting, I. G., Leuenberger, M., Langenfels, R. L., Michel, E. & Steele, L. P.. A 1000-year high precision record of δ13C in atmospheric CO₂. *Tellus B* **51**, 170–193 (1999).
- Garcia, H. E., R. A. Locarnini, T. P. Boyer, J. I. Antonov, O. K. Baranova, M. M. Zweng, and D. R. Johnson. World Ocean Atlas 2009, Volume 3: Dissolved Oxygen, Apparent Oxygen Utilization, and Oxygen Saturation. S. Levitus, Ed. NOAA Atlas NESDIS 70, U.S. Government Printing Office, Washington, D.C., (2010).
- Garcia, H. E., R. A. Locarnini, T. P. Boyer, and J. I. Antonov. World Ocean Atlas 2009, Volume 4: Nutrients (phosphate, nitrate, silicate). S. Levitus, Ed. NOAA Atlas NESDIS 71, U.S. Government Printing Office, Washington, D.C., 398 pp. (2010)
- Gruber, N., Keeling, C. D., Bacastow, R. B., Guenther, P. R., Lueker, T. J., Wahlen, M., Meijer, H. A. J., Mook, W.G. & Stocker, T. F. Spatiotemporal patterns of carbon-

Bibliography and References

- 13 in the global surface oceans and the oceanic Suess effect. *Global Biogeochemical Cycles* **13**, 307–335 (1999).
- Hathorne, E. C., Alard, O., James, R. H. & Rogers, N. W. Determination of intratest variability of trace elements in foraminifera by laser ablation inductively coupled plasma-mass spectrometry. *Geochemistry, Geophysics, Geosystems* **4**, (2003).
- Haug, G. H., Hughen, K. A., Sigman, D. M., Peterson, L. C. & Röhl, U. Southward migration of the Intertropical Convergence Zone through the Holocene. *Science* **293**, 1304–1308 (2001).
- Hönisch, B., Allen, K. A., Lea, D. W., Spero, H. J., Eggins, S. M., Arbuszewski, J., Rosenthal, Y., Russell, A. D. & Elderfield, H. The influence of salinity on Mg/Ca in planktic foraminifers—Evidence from cultures, core-top sediments and complementary $\delta^{18}\text{O}$. *Geochimica et Cosmochimica Acta* **121**, 196–213 (2013).
- Hut, G. Stable isotope reference samples for geochemical and hydrological investigations. Consultant Group Meeting IAEA, Vienna, 16–18 September 1985, Report to the Director General. in 42 (International Atomic Energy Agency, 1987).
- Indermühle, A., Stocker, T. F., Joos, F., Fischer, H., Smith, H. J., Wahlen, M., Deck, B., Mastroianni, D., Tschumi, J., Blunier, T., Meyer, R., & Stauffer, B. Holocene carbon-cycle dynamics based on CO₂ trapped in ice at Taylor Dome, Antarctica. *Nature* **398**, 121–126 (1999).
- Kalnay, E., Kanamitsu, M., Kistler, R., Collins, W., Deaven, D., Gandin, L., Iredell, M., Saha, S., White, G., Woollen, J., Zhu, Y., Leetmaa, A., Reynolds, R., Chelliah, M., Ebisuzaki, W., Higgins, W., Janowiak, J., Mo, K.C., Ropelewski, C., Wang, J., Jenne, R., Joseph, D. The NCEP/NCAR 40-year reanalysis project. *Bulletin of the American meteorological Society* **77**, 437–471 (1996).

Bibliography and References

- Karnauskas, K. B., Smerdon, J. E., Seager, R. & González-Rouco, J. F. A Pacific Centennial Oscillation Predicted by Coupled GCMs*. *Journal of Climate* **25**, 5943–5961 (2012).
- Keeling, C. D. The Suess effect: 13Carbon-14Carbon interrelations. *Environment International* **2**, 229–300 (1979).
- Keeling, C.D., Piper, S. C., Bacastow, R. B., Wahlen, M., Whorf, T. P., Heimann, M. and Meijer, H. A., Exchanges of atmospheric CO₂ and 13CO₂ with the terrestrial biosphere and oceans from 1978 to 2000. I. Global aspects, SIO Reference Series, No. 01-06, Scripps Institution of Oceanography, San Diego (2001).
- Khider, D., Stott, L., Thunell, R. & Hammond, D. Assessing El Niño Southern Oscillation variability during the past millennium. *Paleoceanography* **26**, 3222 (2011).
- Kim, S.-T. & O’Neil, J. R. Equilibrium and nonequilibrium oxygen isotope effects in synthetic carbonates. *Geochimica et Cosmochimica Acta* **61**, 3461–3475 (1997).
- King, A. L. & Howard, W. R. Planktonic foraminiferal δ¹³C records from Southern Ocean sediment traps: New estimates of the oceanic Suess effect. *Global biogeochemical cycles* **18**, (2004).
- Kosaka, Y. & Xie, S.-P. Recent global-warming hiatus tied to equatorial Pacific surface cooling. *Nature* **501**, 403–407 (2013).
- Koutavas, A., Lynch-Stieglitz, J., Marchitto, T. M. & Sachs, J. P. El Niño-Like Pattern in Ice Age Tropical Pacific Sea Surface Temperature. *Science* **297**, 226 –230 (2002).
- Koutavas, A. & Lynch-Stieglitz, J. Glacial-interglacial dynamics of the eastern equatorial Pacific cold tongue-Intertropical Convergence Zone system reconstructed from oxygen isotope records. *Paleoceanography* **18**, (2003).
- Koutavas, A., deMenocal, P. B., Olive, G. C. & Lynch-Stieglitz, J. Mid-Holocene El Niño–Southern Oscillation (ENSO) attenuation revealed by individual foraminifera in eastern tropical Pacific sediments. *Geology* **34**, 993–996 (2006).

Bibliography and References

- Koutavas, A. & Joanides, S. El Niño–Southern Oscillation extrema in the Holocene and Last Glacial Maximum. *Paleoceanography* **27**, (2012).
- Kroopnick, P. M. The distribution of ^{13}C of ΣCO_2 in the world oceans. *Deep Sea Research Part A. Oceanographic Research Papers* **32**, 57–84 (1985).
- Lamb, H. H. *Climate, History and the Modern World*. Psychology Press (1995).
- Laskar, J., Robutel, P., Joutel, F., Gastineau, M., Correia, A.C.M., Levrard, B A long-term numerical solution for the insolation quantities of the earth. *Astronomy & Astrophysics* **428**, 261–285 (2004).
- Laubelenfant, E. & Pierre, C. Variability of delta-c-13 of sigma-co2 in ocean waters of the equatorial pacific. *Oceanologica acta* **17**, 633–641 (1994).
- Lea, D.W., Pak, D.K., Belanger, C.L., Spero, H.J., Hall, M.A., Shackleton, N.J. Paleoclimate history of Galápagos surface waters over the last 135,000 yr. *Quaternary Science Reviews* **25**, 1152–1167 (2006).
- Leduc, G., Vidal, L., Cartapanis, O. & Bard, E. Modes of eastern equatorial Pacific thermocline variability: Implications for ENSO dynamics over the last glacial period. *Paleoceanography* **24**, PA3202 (2009).
- Levin, L. A. Oxygen minimum zone benthos: adaptation and community response to hypoxia. In Gibson, R. N., & Atkinson, R. J. A., eds. *Oceanography and Marine Biology: An Annual Review*, 41, 1-45. Taylor & Francis (2003)
- Li, J., Xie, S.P., Cook, E.R., Huang, G., Arrigo, R. D', Liu, F., Ma, J., Zheng, X.T. Interdecadal modulation of El Niño amplitude during the past millennium. *Nature Climate Change* **1**, 114–118 (2011).
- Linsley, B. K., Rosenthal, Y. & Oppo, D. W. Holocene evolution of the Indonesian throughflow and the western Pacific warm pool. *Nature Geoscience* **3**, 578–583 (2010).

Bibliography and References

- Linsley, B. K., Dunbar, R. B., Wellington, G. M. & Mucciarone, D. A. A coral-based reconstruction of Intertropical Convergence Zone variability over Central America since 1707. *J. Geophys. Res.* **99**, 9977–9994 (1994).
- Ljungqvist, F. C. A new reconstruction of temperature variability in the extra-tropical northern hemisphere during the last two millennia. *Geografiska Annaler: Series A, Physical Geography* **92**, 339–351 (2010).
- Loubere, P. Nutrient and oceanographic changes in the eastern equatorial Pacific from the last full glacial to the present. *Global and Planetary Change* **29**, 77–98 (2001).
- Löwemark, L., Hong, W.-L., Yui, T.-F. & Hung, G.-W. A test of different factors influencing the isotopic signal of planktonic foraminifera in surface sediments from the northern South China Sea. *Marine Micropaleontology* **55**, 49–62 (2005).
- Lynch-Stieglitz, J., Stocker, T. F., Broecker, W. S. & Fairbanks, R. G. The influence of air-sea exchange on the isotopic composition of oceanic carbon: Observations and modeling. *Global Biogeochemical Cycles* **9**, 653–665 (1995).
- Mann, M.E., Zhang, Z., Rutherford, S., Bradley, R.S., Hughes, M.K., Shindell, D., Ammann, C., Faluvegi, G., Ni, F. Global signatures and dynamical origins of the Little Ice Age and Medieval Climate Anomaly. *Science* **326**, 1256–1260 (2009).
- Mann, M. E., Cane, M. A., Zebiak, S. E. & Clement, A. Volcanic and solar forcing of the tropical Pacific over the past 1000 years. *Journal of Climate* **18**, 447–456 (2005).
- Mantua, N. J. & Hare, S. R. The Pacific Decadal Oscillation. *Journal of Oceanography* **58**, 35–44 (2002).
- Marchitto, T. M., Muscheler, R., Ortiz, J. D., Carriquiry, J. D. & Van Geen, A. Dynamical response of the tropical Pacific Ocean to solar forcing during the early Holocene. *Science* **330**, 1378 (2010).
- Marchitto, T. M. Precise multielemental ratios in small foraminiferal samples determined by sector field ICP-MS. *Geochemistry, Geophysics, Geosystems* **7**, (2006).

Bibliography and References

- Marcott, S. A., Shakun, J. D., Clark, P. U. & Mix, A. C. A reconstruction of regional and global temperature for the past 11,300 years. *Science* **339**, 1198–1201 (2013).
- McGregor, H.V., Evans, M.N., Goosse, H., Leduc, G., Martrat, B., Addison, J.A., Mortyn, P.G., Oppo, D.W., Seidenkrantz, M.-S., Sicre, M.-A., Phipps, S.J., Selvaraj, K., Thirumalai, K., Filipsson, H.L., Ersek, V. Robust global ocean cooling trend for the pre-industrial Common Era. *Nature Geoscience* advance online publication, (2015).
- McPhaden, M. J., Zebiak, S. E. & Glantz, M. H. ENSO as an Integrating Concept in Earth Science. *Science* **314**, 1740–1745 (2006).
- Mitchell, T. P. & Wallace, J. M. The annual cycle in equatorial convection and sea surface temperature. *Journal of Climate* **5**, 1140–1156 (1992).
- Moberg, A., Sonechkin, D. M., Holmgren, K., Datsenko, N. M. & Karlén, W. Highly variable Northern Hemisphere temperatures reconstructed from low-and high-resolution proxy data. *Nature* **433**, 613–617 (2005).
- Moy, C. M., Seltzer, G. O., Rodbell, D. T., Anderson, D. M. & others. Variability of El Niño/Southern Oscillation activity at millennial timescales during the Holocene epoch. *Nature* **420**, 162–165 (2002).
- Newton, A., Thunell, R. & Stott, L. Changes in the Indonesian Throughflow during the past 2000 yr. *Geology* **39**, 63–66 (2011).
- Newton, A., Thunell, R. & Stott, L. Climate and hydrographic variability in the Indo-Pacific Warm Pool during the last millennium. *Geophysical Research Letters* **33**, (2006).
- Nürnberg, D., Bijma, J. & Hemleben, C. Assessing the reliability of magnesium in foraminiferal calcite as a proxy for water mass temperatures. *Geochimica et Cosmochimica Acta* **60**, 803–814 (1996).
- Oeschger, H., Siegenthaler, U., Schotterer, U. & Gugelmann, A. A box diffusion model to study the carbon dioxide exchange in nature. *Tellus* **27**, 168–192 (1975).

Bibliography and References

- Olsson, R. K. What Is a Kummerform Planktonic Foraminifer? *Journal of Paleontology* **47**, 327–329 (1973).
- Oppo, D. W. & Fairbanks, R. G. Carbon isotope composition of tropical surface water during the past 22,000 years. *Paleoceanography* **4**, 333–351 (1989).
- Oppo, D. W., Rosenthal, Y. & Linsley, B. K. 2,000-year-long temperature and hydrology reconstructions from the Indo-Pacific warm pool. *Nature* **460**, 1113–1116 (2009).
- Ortiz, J. D., Mix, A. C., Wheeler, P. A. & Key, R. M. Anthropogenic CO₂ invasion into the northeast Pacific based on concurrent δ¹³CDIC and nutrient profiles from the California Current. *Global Biogeochem. Cycles* **14**, 917–929 (2000).
- PAGES 2K Consortium, Ahmed, M., Anchukaitis, K., Buckley, B.M., Braida, M., Borgaonkar, H.P., Asrat, A., Cook, E.R., Büntgen, U., Chase, B.M., Christie, D.A., others., Continental-Scale Temperature Variability during the Past Two Millennia: Supplementary Information. *Nature Geoscience* **6**, (2013).
- Pena, L. D., Cacho, I., Ferretti, P. & Hall, M. A. El Niño–Southern Oscillation-like variability during glacial terminations and interlatitudinal teleconnections. *Paleoceanography* **23**, (2008).
- Pennington, J. T., Mahoney, K. L., Kuwahara, V. S., Kolber, D. D., Calienes, R., & Chavez, F. P. Primary production in the eastern tropical Pacific: a review. *Progress in Oceanography* **69**, 285–317 (2006).
- Quay, P. D., Tilbrook, B. & Wong, C. S. Oceanic uptake of fossil fuel CO₂: Carbon-13 evidence. *Science* **256**, 74–79 (1992).
- Rasmusson, E. M. & Carpenter, T. H. Variations in tropical sea surface temperature and surface wind fields associated with the Southern Oscillation/El Niño. *Monthly Weather Review* **110**, 354–384 (1982).
- Ravelo, A. C. & Hillaire-Marcel, C. Chapter Eighteen The Use of Oxygen and Carbon Isotopes of Foraminifera in Paleoceanography. *Developments in Marine Geology* **1**, 735–764 (2007).

Bibliography and References

- Rodbell, D. T., Seltzer, G. O., Anderson, D. M., Abbott, M. B., Enfield, D. B., & Newman, J. H. An ~15,000-year record of El Niño-driven alluviation in southwestern Ecuador. *Science* **283**, 516–520 (1999).
- Rodgers, K.B., Blanke, B., Madec, G., Aumont, O., Caias, P., Dutay, J.-C. Extratropical sources of equatorial Pacific upwelling in an OGCM. *Geophysical research letters* **30**, (2003).
- Romanek, C. S., Grossman, E. L. & Morse, J. W. Carbon isotopic fractionation in synthetic aragonite and calcite: effects of temperature and precipitation rate. *Geochimica et Cosmochimica Acta* **56**, 419–430 (1992).
- Rosenthal, Y., Boyle, E. A. & Slowey, N. Temperature control on the incorporation of magnesium, strontium, fluorine, and cadmium into benthic foraminiferal shells from Little Bahama Bank: Prospects for thermocline paleoceanography. *Geochimica et Cosmochimica Acta* **61**, 3633–3643 (1997).
- Rosenthal, Y., Linsley, B. K. & Oppo, D. W. Pacific ocean heat content during the past 10,000 years. *Science* **342**, 617–621 (2013).
- Sachs, J. P., Sachse, D., Smittenberg, R. H., Zhang, Z., Battisti, D. S., & Golubic, S. Southward movement of the Pacific intertropical convergence zone AD 1400–1850. *Nature Geoscience* **2**, 519–525 (2009).
- Sadekov, A. Y., Eggins, S. M. & De Deckker, P. Characterization of Mg/Ca distributions in planktonic foraminifera species by electron microprobe mapping. *Geochemistry, Geophysics, Geosystems* **6**, (2005).
- Sadekov, A. Y. *et al.* Palaeoclimate reconstructions reveal a strong link between El Niño-Southern Oscillation and Tropical Pacific mean state. *Nature communications* **4**, (2013).
- Schneider, T., Bischoff, T. & Haug, G. H. Migrations and dynamics of the intertropical convergence zone. *Nature* **513**, 45–53 (2014).

Bibliography and References

- Shevenell, A. E., Ingalls, A. E., Domack, E. W. & Kelly, C. Holocene Southern Ocean surface temperature variability west of the Antarctic Peninsula. *Nature* **470**, 250–254 (2011).
- Slocum, G. Has the amount of carbon dioxide in the atmosphere changed significantly since the beginning of the twentieth century. *Monthly Weather Review* **83**, 225–231 (1955).
- Spero, H. J. & Williams, D. F. Extracting environmental information from planktonic foraminiferal $\delta^{13}\text{C}$ data. *Nature* **335**, 717–719 (1988).
- Spero, H. J. & Williams, D. F. Opening the carbon isotope ‘vital effect’ black box 1. Seasonal temperatures in the euphotic zone. *Paleoceanography* **4**, 593–601 (1989).
- Spero, H. J. Life history and stable isotope geochemistry of planktonic foraminifera. *Paleontological Society Papers* **7–36** (1998).
- Spero, H. J., Bijma, J., Lea, D. W. & Bemis, B. E. Effect of seawater carbonate concentration on foraminiferal carbon and oxygen isotopes. *Nature* **390**, 497–500 (1997).
- Spero, H. J., Lerche, I. & Williams, D. F. Opening the carbon isotope‘ vital effect’ black box, 2, Quantitative model for interpreting foraminiferal carbon isotope data. *Paleoceanography* **6**, 639–655 (1991).
- Spero, H. J., Mielke, K. M., Kalve, E. M., Lea, D. W. & Pak, D. K. Multispecies approach to reconstructing eastern equatorial Pacific thermocline hydrography during the past 360 kyr. *Paleoceanography* **18**, 1022 (2003).
- Steinhardt, J., Cléroux, C., de Nooijer, L. J., Brummer, G. J., Zahn, R., Ganssen, G., & Reichart, G. J. Reconciling single-chamber Mg/Ca with whole-shell $\delta^{18}\text{O}$ in surface to deep-dwelling planktonic foraminifera from the Mozambique Channel. *Biogeosciences* **12**, 2411–2429 (2015).

Bibliography and References

- Steinhilber, F., Beer, J. & Fröhlich, C. Total solar irradiance during the Holocene. *Geophysical Research Letters* **36**, L19704 (2009).
- Stevenson, S., Fox-Kemper, B., Jochum, M., Neale, R., Deser, C., Meehl, G. Will There Be a Significant Change to El Niño in the Twenty-First Century? *Journal of Climate* **25**, 2129–2145 (2011).
- Stott, L., Cannariato, K., Thunell, R., Haug, G.H., Koutavas, A., Lund, S. Decline of surface temperature and salinity in the western tropical Pacific Ocean in the Holocene epoch. *Nature* **431**, 56–59 (2004).
- Stuiver, M. & Braziunas, T. F. Modeling Atmospheric ^{14}C Influences and ^{14}C Ages of Marine Samples to 10 000 BC. *Radiocarbon* **35**, 137–189 (1993).
- Suess, H. E. Radiocarbon Concentration in Modern Wood. *Science* **122**, 415–417 (1955).
- Swart, P.K., Greer, L., Rosenheim, B.E., Moses, C.S., Waite, A.J., Winter, A., Dodge, R.E., Helmle, K. The ^{13}C Suess effect in scleractinian corals mirror changes in the anthropogenic CO_2 inventory of the surface oceans. *Geophysical Research Letters* **37**, (2010).
- Takahashi, T., Sutherland, S.C., Wanninkhof, R., Sweeney, C., Feely, R.A., Chipman, D.W., Hales, B., Friederich, G., Chavez, F., Sabine, C., Watson, A., Bakker, D.C.E., Schuster, U., Metzl, N., Yoshikawa-Inoue, H., Ishii, M., Midorikawa, T., Nojiri, Y., Körtzinger, A., Steinhoff, T., Hoppema, M., Olafsson, J., Arnarson, T.S., Tilbrook, B., Johannessen, T., Olsen, A., Bellerby, R., Wong, C.S., Delille, B., Bates, N.R., de Baar, H.J.W. Climatological mean and decadal change in surface ocean pCO_2 , and net sea–air CO_2 flux over the global oceans. *Deep Sea Research Part II: Topical Studies in Oceanography* **56**, 554–577 (2009).
- Taylor, R. E. & Berger, R. Radiocarbon content of marine shells from the Pacific coasts of Central and South America. *Science* **158**, 1180–1182 (1967).

Bibliography and References

- Thirumalai, K., Partin, J. W., Jackson, C. S. & Quinn, T. M. Statistical constraints on El Niño Southern Oscillation reconstructions using individual foraminifera: A sensitivity analysis. *Paleoceanography* **28**, 401–412 (2013).
- Thompson, L. G., Mosley-Thompson, E., Davis, M. E., Zagorodnov, V. S., Howat, I. M., Mikhalenko, V. N., & Lin, P. N. Annually resolved ice core records of tropical climate variability over the past ~1800 years. *Science* **340**, 945–950 (2013).
- Tierney, J. E., Oppo, D. W., Rosenthal, Y., Russell, J. M. & Linsley, B. K. Coordinated hydrological regimes in the Indo-Pacific region during the past two millennia. *Paleoceanography* **25**, PA1102 (2010).
- Tourre, Y. M. & White, W. B. ENSO signals in global upper-ocean temperature. *Journal of Physical Oceanography* **25**, 1317–1332 (1995).
- Trujillo-Ortiz, A. and R. Hernandez-Walls. BFtest: Brown-Forsythe's test for homogeneity of variances. A MATLAB file. [WWW document]. URL <http://www.mathworks.com/matlabcentral/fileexchange/loadFile.do?objectId=3412&objectType=FILE> (2003)
- Tudhope, A.W., Chilcott, C.P., McCulloch, M.T., Cook, E.R., Chappell, J., Ellam, R.M., Lea, D.W., Lough, J.M., Shimmield, G.B. Variability in the El Niño-Southern Oscillation through a glacial-interglacial cycle. *Science* **291**, 1511–1517 (2001).
- Urey, H. C. Oxygen isotopes in nature and in the laboratory. *Science* **108**, 489–496 (1948).
- Vecchi, G. A., Clement, A. & Soden, B. J. Examining the tropical Pacific's response to global warming. *Eos, Transactions American Geophysical Union* **89**, 81 (2008).
- Vecchi, G. A., Soden, B. J., Wittenberg, A. T., Held, I. M., Leetmaa, A., & Harrison, M. J. Weakening of tropical Pacific atmospheric circulation due to anthropogenic forcing. *Nature* **441**, 73–76 (2006).

Bibliography and References

- Wang, C., Deser, C., Yu, J.-Y., DiNezio, P., Clement, A. *El Niño and Southern Oscillation (ENSO): a review*. In Glynn, P., Manzello, D., Enochs, I. (eds.), *Coral Reefs of the Eastern Pacific*. Springer (2012).
- Wang, C. & Fiedler, P. C. ENSO variability and the eastern tropical Pacific: A review. *Progress in Oceanography* **69**, 239–266 (2006).
- Wang, C., and Picaut, J., *Understanding ENSO physics – a review*. In Wang, C., Xie, S. P., and Carton, J. A. (eds.), *Earth's Climate: The Ocean-Atmosphere Interaction*. Washington, DC: AGU, pp. 21–48 (2004).
- Wang, L. Isotopic signals in two morphotypes of *Globigerinoides ruber* (white) from the South China Sea: implications for monsoon climate change during the last glacial cycle. *Palaeogeography, Palaeoclimatology, Palaeoecology* **161**, 381–394 (2000).
- Yan, H., Wei, W., Soon, W., An, Z., Zhou, W., Liu, Z., Wang, Y., Carter, R.M. Dynamics of the intertropical convergence zone over the western Pacific during the Little Ice Age. *Nature Geoscience* **8**, 315–320 (2015).
- Zhang, P.Z., Cheng, H., Edwards, R.L., Chen, F.H., Wang, Y.J., Yang, X.L., Liu, J., Tan, M., Wang, X.F., Liu, J.H., An, C.L., Dai, Z.B., Zhou, J., Zhang, D.Z., Jia, J.H., Jin, L.Y., Johnson, K.R. A test of climate, sun, and culture relationships from an 1810-year Chinese cave record. *Science* **322**, 940–942 (2008).